

Cyclostrophic wind in the mesosphere of Venus from Venus Express observations

Von der Fakultät für Elektrotechnik, Informationstechnik, Physik
der Technischen Universität Carolo-Wilhelmina
zu Braunschweig
zur Erlangung des Grades eines
Doktors der Naturwissenschaften
(Dr.rer.nat.)
genehmigte
Dissertation

von Arianna Piccialli
aus Napoli/Italy

Bibliografische Information der Deutschen Nationalbibliothek

Die Deutsche Nationalbibliothek verzeichnet diese Publikation in der Deutschen Nationalbibliografie; detaillierte bibliografische Daten sind im Internet über <http://dnb.d-nb.de> abrufbar.

1. Referentin oder Referent: Prof. Dr. Andreas Hördt

2. Referentin oder Referent: Prof. Fred W. Taylor

eingereicht am: 29. März 2010

mündliche Prüfung (Disputation) am: 16. Juni 2010

ISBN 978-3-942171-36-6

uni-edition GmbH 2010

<http://www.uni-edition.de>

© Arianna Piccialli



This work is distributed under a
Creative Commons Attribution 3.0 License

Printed in Germany

Contents

Summary	5
1 Properties and dynamics of Venus atmosphere	7
1.1 Venus in human history	7
1.2 Venus atmosphere	8
1.3 Venus mesospheric circulation and dynamics	13
1.4 Goals and structure of the thesis	16
2 Venus Express meteorology observations	19
2.1 Venus Express mission and payload	19
2.2 Sounding of the atmospheric temperature structure	22
2.2.1 VIRTIS (Visible and Infrared Thermal Imaging Spectrometer) . .	23
2.2.2 VeRa (Radio Science Experiment)	27
2.3 Wind velocity measurements	33
2.3.1 VIRTIS (Visible and Infrared Thermal Imaging Spectrometer) . .	33
2.3.2 VMC (Venus Monitoring Camera)	34
3 Methods of wind determination	39
3.1 Wind determinations	39
3.1.1 Direct measurements	39
3.1.1.1 Cloud-tracking winds	39
3.1.1.2 Doppler shifts measurements	41
3.1.1.3 Doppler tracking of balloons and descent probes	41
3.1.2 Thermal winds	42
3.1.2.1 Thermal wind equation and cyclostrophic balance	43
4 Thermal zonal wind retrieval	49
4.1 Wind retrievals from VIRTIS temperature soundings	49
4.1.1 Retrieval method	49
4.1.2 Thermal winds	50
4.2 Wind retrievals from VeRa radio occultation data	54
4.2.1 Retrieval method	54
4.2.2 Thermal winds	54
4.2.3 Alternative retrieval method	56
4.3 Sensitivity to the lower boundary condition	57
4.4 Uncertainties in wind speeds	59

5	Discussion	65
5.1	Zonal thermal winds from Venus Express observations	65
5.2	Comparison with cloud-tracked winds	68
5.2.1	Cloud top morphology	71
5.3	Comparison with ground-based observations	73
5.4	Dynamical properties	74
5.4.1	Stability studies	75
5.4.2	Angular momentum	79
5.4.3	Ertel potential vorticity	80
5.4.4	Barotropic instability	83
5.5	Other cyclostrophic systems	84
5.5.1	Super-rotation on Titan	85
5.5.2	Dust devils on Earth and Mars	87
5.5.3	Tornadoes and hurricanes on Earth	90
6	Conclusions and outlook	93
6.1	Conclusions	93
6.2	Future work and outlook	95
A	The adiabatic lapse rate in Venus atmosphere	97
	Bibliography	99
	Publications	111
	Acknowledgements	117
	Curriculum Vitae	119

Summary

Venus mesosphere (60–100 km altitude) is a transition region characterised by a complex dynamic: strong retrograde zonal winds dominate in the lower mesosphere while a solar-antisolar circulation is observed in the upper mesosphere. The super-rotation extends from the surface up to the cloud top (~ 70 km altitude) with wind speeds of only few meters per second near the surface and reaching a maximum value of ~ 100 m s⁻¹ at the cloud top, corresponding to a rotation period of 4 Earth days (~ 60 times faster than Venus itself). The solar-antisolar circulation driven by the day-night contrast in solar heating, occurs above 110 km of altitude with speeds of 120 m s⁻¹. The processes responsible for maintaining the zonal super-rotation in the lower atmosphere and its transition to the solar-antisolar circulation in the upper atmosphere are still unknown. Venus Express, the first ESA mission to Venus, provided a wealth of data about Venus meteorology. The aim of this thesis is to study the dynamics of Venus mesosphere from the Venus Express observations with emphasis on thermal wind retrievals from temperature soundings.

Different techniques have been used to obtain direct observations of wind at various altitudes: tracking of clouds features in ultraviolet (UV) and near infrared (NIR) images give information on wind speed at the cloud top (~ 70 km altitude) and within the clouds (~ 61 km, ~ 66 km) while groundbased measurements of Doppler shift in CO₂ band at 10 μ m and in several CO millimetre lines sound winds at ~ 110 km of altitude. In the mesosphere where direct observations of wind are not possible, the only way to characterise the circulation is to derive zonal wind field from the vertical temperature structure using a special approximation of the thermal wind equation: the cyclostrophic balance. Previous studies showed that on a slowly rotating planet, like Venus, strong zonal winds at the cloud top can be described by the cyclostrophic balance in which equatorward component of centrifugal force is balanced by meridional pressure gradient. This equation gives a possibility to reconstruct zonal wind if the temperature field is known.

Two experiments on board the European Venus Express (VEx) orbiter are sounding temperature structure of the Venus mesosphere: Visible and Infrared Thermal Imaging Spectrometer (VIRTIS) sounds the Venus Southern hemisphere in the altitude range 65 – 90 km with a very good spatial and temporal coverage. The radio science experiment (VeRa) observes both north and south hemispheres between 40 – 90 km of altitude with a vertical resolution of ~ 500 m. In addition, Venus Monitoring Camera (VMC) acquires UV images used for direct measurements of wind speed by cloud-tracking. VEx gives for the first time the opportunity to verify the cyclostrophic hypothesis by comparing cloud-tracked and thermal winds.

In this thesis I derived zonal cyclostrophic winds from VIRTIS and VeRa temperature soundings. The main features of the retrieved winds are: (1) the midlatitude jet with a maximum speed up to 140 ± 15 m s⁻¹ which occurs around 50°S latitude at 70 km alti-

tude; (2) the fast decrease of the wind speed from 60°S toward the pole; (3) the decrease of the wind speed with increasing height above the jet. The influence of the temperature retrievals uncertainties and of the lower boundary condition on the thermal wind field was analysed. An approximate uncertainty of $\pm 15 \text{ m s}^{-1}$ on zonal wind was found. Zonal thermal winds were shown to be only slightly dependent on the choice of lower boundary condition. VIRTIS temperature field shows radiative cooling by $\sim 15 \text{ K}$ during the night at cloud top which affects also the thermal wind field. The midlatitude jet speed appears to increase during the night by $\sim 10 - 20 \text{ m s}^{-1}$. However, any conclusion must be taken cautiously, since the magnitude of speed change with local time is within the uncertainty on the wind itself. Thermal winds were compared to the cloud-tracked winds from imaging observations that allowed to validate the cyclostrophic assumption. Cyclostrophic wind shows satisfactory agreement with the cloud-tracked winds derived from the Venus Monitoring Camera (VMC/VEx) UV images. A disagreement is observed at the equator and near the pole due to the breakdown of the cyclostrophic approximation.

From the temperature and thermal wind fields we calculated the Richardson number, the parameter characterising the stability of the atmosphere. We have found that the atmosphere is dominated by convection from $\sim 45 \text{ km}$ altitude up to the cloud top. High value of Richardson number in the region of midlatitude jet indicates highly stable atmosphere. Verification of the necessary condition for barotropic instability implies that it can occur on the poleward side of the midlatitude jet where planetary waves are expected to play an important role in the maintenance of the circulation.

Venus plays a unique role in the solar system as a natural laboratory to investigate the circulation on a slowly rotating planet. Comparative studies between atmospheres dynamics of other planets can improve our understanding of the current conditions and evolution of their climate. Titan super-rotation, dust devils on Earth and Mars, terrestrial tornadoes and hurricanes are only an example of other cyclostrophic systems whose investigation can help to understand the complex Venesian climate.

1 Properties and dynamics of Venus atmosphere

"To the great Queen of Heaven, Inanna, I want to address my greeting. To her who fills the sky with her pure blaze, to the luminous one, to Inanna, as bright as the sun"

(a Sumerian hymn, Cochrane, 2002).

1.1 Venus in human history

As one of the brightest objects in the sky, Venus has been known since prehistoric times and has always played an important role in human culture. The planet is named after Venus, the Roman goddess of love. First records of the planet can be found in Babylonian cuneiform texts dating to 1600 BC. Babylonians named the planet after the goddess of love and war, Ishtar, also related to the Sumerian Inanna. The planet was believed to be two separate bodies by ancient Egyptians and Greeks who distinguished between the morning star (Phosphoros) and the evening star (Hesperos). It is attributed to Pythagoras the discovery that the morning and evening stars are a single object. First scientific studies of Venus were realised by Galileo Galilei who was the first to observe the phases of Venus in December 1610; his observations contributed to support Copernicus heliocentric theory, in fact, Venus phases could not be explained by the Ptolemaic geocentric model. On June 5, 1761 during a transit of Venus across the Sun which was observed by 176 scientists from 117 stations all over the world, the Russian astronomer Mikhail V. Lomonosov provided the first evidence that Venus had an atmosphere. The presence of an atmosphere complicated the efforts to determine the rotation period of the planet: two astronomer, Giovanni Domenico Cassini in the XVII century and Johann Hieronymus Schröter in XVIII independently obtained as rotation period of the planet the incorrect value of ~ 24 hours. The Italian astronomer Giovanni Schiaparelli in 1890 was the first to speculate that the rotation period of Venus was much lower. Few more information about the planet were obtained until the 20th century when the planet was photographed with an ultraviolet (UV) filter by Wright (1927) and Ross (1928). UV images revealed the presence of cloud features (UV markings); by following the evolution of the markings became possible to investigate in more detail the composition, circulation and dynamics of Venus atmosphere. A new era in the studies of Venus began only with space exploration which started in 1962 with the Mariner 2 probe. Since then many missions have continued investigating the planet: a set of orbiters, descent probes, and balloons delivered to Venus by the Soviet Union in the framework of Venera and VEGA program, the US Mariner 2 and 10 flyby spacecraft, the orbiter and multiprobe Pioneer Venus missions, the dedi-

	Venus	Earth
Mass	4.87×10^{24} kg	5.98×10^{24} kg
Radius	6052 km	6378 km
Density	5250 kg/m ³	5520 kg/m ³
Av. distance from Sun	108 million km	150 million km
Rotation period (day)	243 Earth days (retrograde)	23 hours 56 minutes
Orbit period (year)	224.7 Earth days	365.2 days
Surface temp. (mean)	465°C	15°C
Surface pressure	90 bar	1 bar (sea level)
Albedo	0.76	0.37
Highest point on surface	Maxwell Montes (8 km)	Mount Everest (8.8 km)
Orbit inclination	3.4°	0° by definition
Obliquity of axis	178°	23.5°
Moons	None	1 (The Moon)

Table 1.1: Basic atmospheric parameters for Venus and Earth (Copyright ESA).

cated radar orbiter Magellan. More recently, the Galileo and Cassini spacecrafts observed Venus during encounters made *en route* to their ultimate targets in the outer Solar System. Many ground-based observations have also contributed to detailed studies of the planet. Yet, the "morning star" still has many mysteries which need to be unveiled (Cruikshank, 1983).

1.2 Venus atmosphere

Venus is the second-closest planet to the Sun, orbiting it every 224.7 Earth days and slowly rotating in a retrograde direction¹ with a period of 243 days. First ground-based observations of Venus lead to the conclusion that our nearest planetary neighbour was in many respects the twin of the Earth. Indeed, the two planets are similar in size, gravity and bulk composition as can be observed in table 1.1. Nevertheless, further investigations by spacecrafts revealed that the two planets present very different atmospheric conditions: Venus is characterised by an extremely hot and dry surface with a temperature of ~ 735 K, and a high surface pressure of 92 bars resulting from a strong greenhouse effect and it is shrouded by a cloud layer about 22 km thick located between 48 km and 70 km of altitude, with additional hazes up to 90 km, and down to 30 km (Fig. 1.1). As a consequence of the ubiquitous clouds which scatter back the incoming solar radiation, the bond albedo of Venus is about 2.5 times that of Earth (Table 1.1), thus that Venus absorbs less radiative energy than Earth, despite being closer to the Sun. In figure 1.2 is shown the comparison between the vertical temperature profiles of Venus and Earth. In the range where they overlap in pressure they show a similar trend. The main difference occurs around 1 mbar which corresponds to the Earth's stratosphere; in this region is observed an increase of temperature with altitude due to the presence of Earth's ozone layer which has no equivalent on Venus.

Composition and clouds: the Venusian atmosphere consists mainly of CO₂ (96.5%) and N₂ (3.5%) (Table 1.2). Sulphur bearing gases, carbon and chlorine compounds, and

¹Most planets rotate counter-clockwise, Venus and Uranus rotate clockwise in "retrograde" direction.

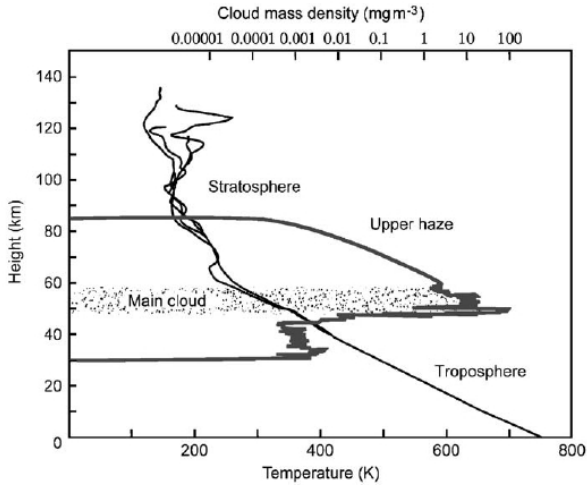


Figure 1.1: Temperature (black curves) and cloud density (grey curve) profiles of Venus atmosphere based on measurements from several different instruments on the Pioneer Venus orbiter and entry probes (Taylor, 2006b).

Species	Venus	Earth
Carbon dioxide	0.96	380 ppm
Nitrogen	0.035	0.770
Sulfur dioxide	150 ppm	0.2 ppb
Argon	70 ppm	9340 ppm
Carbon monoxide	30 ppm	0.1 ppm
Water vapor	20 ppm	~ .01
Helium	12 ppm	5 ppm
Neon	7 ppm	18 ppm
Atomic oxygen	trace	trace
Hydroxyl	trace	trace
Atomic hydrogen	trace	trace

Table 1.2: Composition of the atmospheres of Venus and Earth as fractional abundances except where otherwise is stated (Taylor and Grinspoon, 2009).

water vapour are also present in the atmosphere in amounts from few to few hundred parts per million (ppm) (Esposito et al., 1997). Minor constituents exhibit strong temporal and spatial variability, this indicates their involvement in numerous chemical cycles and dynamical processes.

The clouds which completely veil the planet are almost featureless in visible light but in the near-ultraviolet (UV) spectral range display prominent markings, with an overall

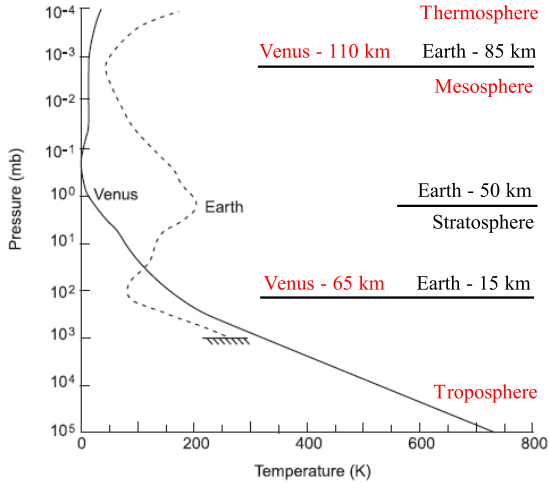
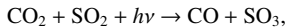


Figure 1.2: Comparison between Earth (dashed line) and Venus (solid line) vertical temperature profiles (Taylor and Grinspoon, 2009). Regions of the atmosphere are also shown. The vertical scale is pressure in millibars (1000 mbar equals the mean surface pressure on Earth).

V-shaped morphology (Fig. 1.3, *left*). Although the precise composition of UV absorbers in the cloud layers has yet to be identified, spectroscopic observations have shown that the dark markings in the ultraviolet spectral range are produced in part by sulfur dioxide (SO_2). Within the main cloud deck, particles of different sizes have been found at different altitudes. The particles have a size that ranges from $1 \mu\text{m}$ to more than $30 \mu\text{m}$ and show a trimodal size distribution. The smallest particles, 'mode 1', have an unknown composition and form an aerosol haze extending throughout the cloud layer. Ground-based polarimetric and spectroscopic observations showed that the upper clouds consist of intermediate size or 'mode 2' droplets made of 75% H_2SO_4 and 25% H_2O . Sulfuric acid drops are formed through photochemical reaction between H_2O and SO_2 at the cloud tops via the reactions:



Both components seem to originate from volcanic degassing. Most of the cloud mass is in the big 'mode 3' particles; these can be either originated from an aggregate of sulphuric acid drops of mode 2 or another mode with a different, unknown, composition. Pioneer Venus Large Probe data indirectly suggested solid, probably non-spherical, particles which would exclude H_2O , H_2SO_4 or HCl . At visible, UV and most infrared wavelengths,

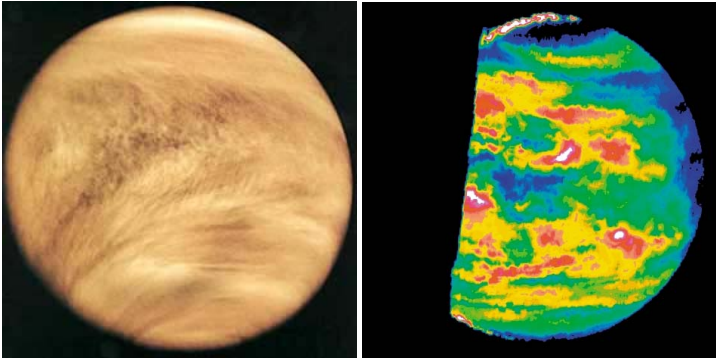


Figure 1.3: *Left*: ultraviolet image of Venus clouds as seen by the Pioneer Venus Orbiter (Copyright NASA). *Right*: NIMS/Galileo image of Venus night side at $2.3 \mu\text{m}$ (Carlson et al., 1991). False colors indicate variations of brightness due to spatial inhomogeneity in cloud opacity.

Venus clouds are so thick ($\tau \gg 1$) that the planet's surface is completely hidden. However, through several near-infrared spectral "windows", the hot surface and lower atmosphere of Venus can be observed from space. Figure 1.3 (*right*) shows an image of Venus clouds taken with the Near-Infrared Mapping Spectrometer (NIMS) on Galileo spacecraft at a wavelength of $2.3 \mu\text{m}$, where the lower level clouds are probed ($\sim 50 \text{ km}$ altitude). The night side near-IR observations revealed significant spatial variations of the cloud structure that, together with observed strong variations of minor species concentrations in and around the cloud level, indicate an high meteorological activity at cloud level.

Thermal structure: Venus atmosphere can be divided in three distinct regions: troposphere ($0 - 65 \text{ km}$), mesosphere ($65 - 110 \text{ km}$) and thermosphere ($> 110 \text{ km}$). First observations of the troposphere or lower atmosphere were limited to in situ measurements acquired by 16 descent probes, mostly in equatorial latitudes (Seiff et al., 1985). The descent probes showed that the temperature structure below 30 km of altitude is characterised by a lapse rate of $8 - 9 \text{ K/km}$, high surface temperature of $\sim 735 \text{ K}$, and a high surface pressure of 92 bars. The discovery of the near infrared spectral "windows" (Allen and Crawford, 1984), through which thermal radiation leaks to space from the lower atmosphere, allowed to study the composition and thermal structure of the atmosphere below the clouds on the nightside of the planet. The temperature structure of the middle atmosphere was observed remotely by the Venera and Pioneer Venus orbiters (Taylor et al., 1980; Zasova et al., 1999), it shows a significant latitudinal variability probably driven by the dynamics. Figure 1.4 shows an example of Venusian mesospheric temperature field; some important features of Venus mesosphere can be observed: above $\sim 70 \text{ km}$ of altitude temperatures increase from equator to pole, this is known as the "warm polar mesosphere". This trend is the opposite of expectations from radiative-convective equilibrium since solar heating is higher at equator as compared to poles. This indicates a

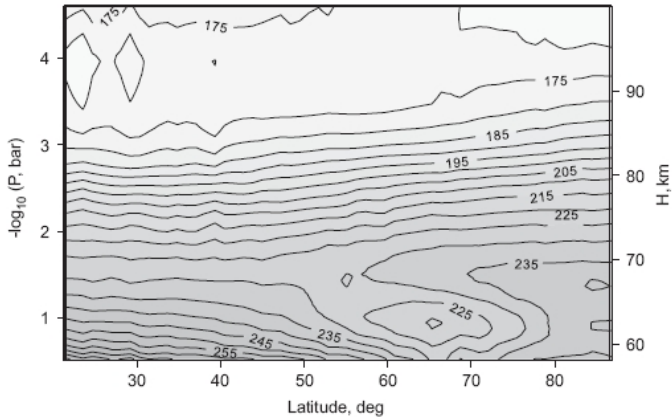


Figure 1.4: Global averaged temperature field derived from the Venera 15 IR spectrometry data (Zasova et al., 2007).

significant role of atmospheric dynamics in the poleward branch of the Hadley cell which redistribute the excess of solar heating at the equator. However, the physical mechanisms responsible for this behaviour remain still poorly understood, partly because the early observations were limited in latitude and local time coverage. At cloud top (~ 65 km of altitude) temperature decreases about 25 K from equator to $\sim 65^\circ$ latitude; this feature is called the "cold collar". Venus thermosphere was investigated by Pioneer Venus remote observations of UV airglow and in situ measurements of neutral densities (Keating et al., 1985; Fox and Bougher, 1991). These observations show that the thermosphere of Venus is cooler than the Earth's (Fig. 1.2), despite Venus' proximity to the Sun, because of the greater abundance of carbon dioxide, which is very efficient at radiating heat to space. Above 140 km of altitude temperature has an approximately constant value of 300 K. A sharp collapse of temperature is observed across the terminator to the night side where the temperature reaches a maximum value of 100 K; this region, known as "cryosphere", has no counterpart anywhere else in the Solar System.

Greenhouse effect: the high abundance of CO_2 provides the largest contribution to the greenhouse effect on Venus. Other greenhouse gases are H_2O , SO_2 and sulphuric acid clouds. Although less than 10% of the incident solar radiation penetrates through the atmosphere and heats the surface, the presence of these species in the atmosphere prevents thermal radiation from escaping to space. This results in a difference of ~ 450 K between the surface temperature and that of the cloud tops, whose observed temperature is ~ 240 K. Venus is not the only planet where a greenhouse effect is present: it is acting also on Mars and Earth. On Mars its efficiency is low (~ 7 K) due to the very thin atmosphere. On Earth the greenhouse effect heats the surface by about 35 K, which is of crucial importance for the presence of life on our planet.

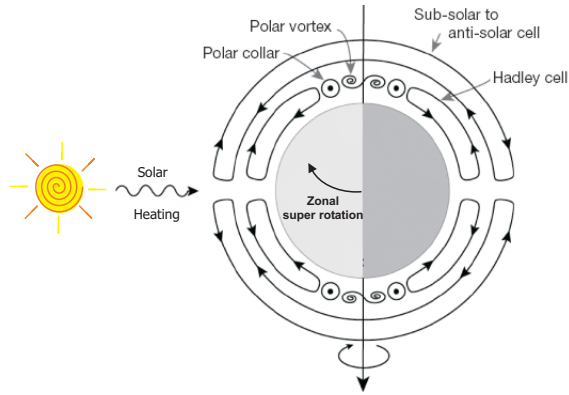


Figure 1.5: Schematic view of main features of Venus circulation (Taylor and Grinspoon, 2009).

1.3 Venus mesospheric circulation and dynamics

Venus' mesosphere (60 – 100 km altitude) is a transition region characterised by an extremely complex dynamic: strong retrograde zonal winds dominate in the troposphere and lower mesosphere while a solar-antisolar circulation can be observed in the upper mesosphere (Fig. 1.5). Tracking of the UV markings, descent probes, and Vega balloon trajectories (Rossow et al., 1980; Counselman et al., 1980; Kerzhanovich and Limaye, 1985) all showed that the super-rotation extends from the surface up to the cloud top with wind speeds of only few meter per second near the surface and reaching a maximum value of $\sim 100 \text{ m s}^{-1}$ at cloud top, corresponding to a rotation period of 4 Earth days (~ 60 times faster than Venus itself). The solar-antisolar circulation is driven by the day-night contrast in solar heating, it occurs above 110 km of altitude with speeds of 120 m s^{-1} (Bougher et al., 1997; Lellouch et al., 1997). The processes responsible for maintaining the zonal super-rotation in the lower atmosphere and its transition to the solar-antisolar circulation in the upper atmosphere are still unknown (Schubert, 1983; Gierasch et al., 1997; Schubert et al., 2007). In particular, what is most puzzling is how the atmosphere is accelerated to such high speeds on a slowly-rotating planet. Earlier studies (Baker and Leovy, 1987; Newman and Leovy, 1992) suggest that the super-rotation is maintained by the transport of retrograde zonal momentum upward through thermal tides at the equator and then poleward by a meridional cell. Nevertheless, all attempts to model the zonal super-rotation have had only a partial success so far, indicating that the basic mechanisms of this phenomenon are still unclear. Figure 1.6(a) compares zonal wind profiles acquired by the entry probes of the Veneras and Pioneer Venus. Wind profiles exhibit alternating layers of high and low shear; below 10 km altitude velocities are no larger than few meter per second. Between about 10 km and the cloud tops (~ 60 km altitude) the circulation is dominated by a retrograde zonal motion and the zonal wind speeds increase monotonically with altitude from near zero to $\sim 100 \text{ m s}^{-1}$. The differences in Venera and Pioneer

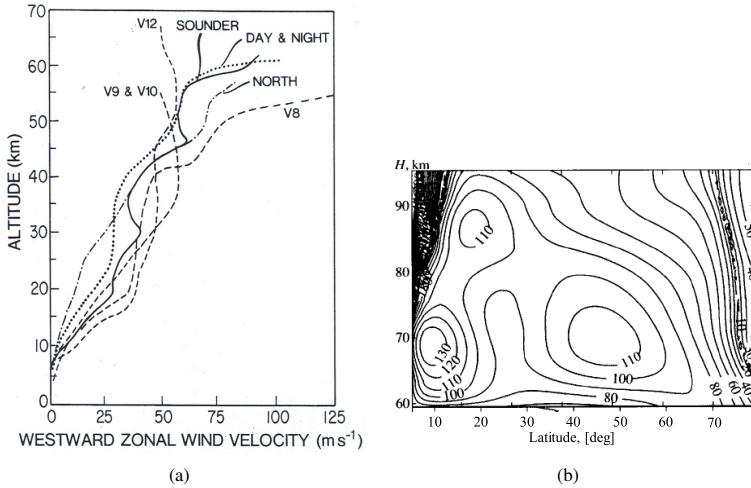


Figure 1.6: (a) A comparison of zonal wind velocity profiles from Pioneer Venus and Venera probes (Schubert et al., 1980); (b) the globally averaged field of the cyclostrophic wind (Zasova et al., 2000).

Venus zonal wind velocity profiles (Fig. 1.6(a)) may reflect variations in the wind field over long periods of time.

Atmospheric dynamics at the cloud tops: the cloud top winds have been particularly well studied by the tracking of cloud-like features in ultraviolet images from the Mariner 10 flyby (Limaye and Suomi, 1981), the Pioneer Venus orbiter (Rossow et al., 1980) and Galileo flyby (Crisp et al., 1991; Peralta et al., 2007). The latitudinal zonal wind profiles observed by cloud-tracking methods have regularly shown the presence of a strong jet with speed of $\sim 120 \text{ m s}^{-1}$ in the latitude range $40 - 60^\circ$. These observations are in agreement with the assumption of cyclostrophic balance in Venus' atmosphere. Leovy (1973) was the first to notice that on slowly rotating planet, like Venus, strong zonal winds at cloud top can be described by cyclostrophic balance in which equatorward component of centrifugal force is balanced by meridional pressure gradient. The cyclostrophic approximation gives a possibility to reconstruct zonal wind if the temperature field is known. The mesospheric temperature field retrieved from the Pioneer Venus (Taylor et al., 1983), Venera-15 (Zasova et al., 2007) and Galileo (Roos-Serote et al., 1995) radiance measurements has been used to derive the cyclostrophic wind (Newman et al., 1984; Roos-Serote et al., 1995; Zasova et al., 2007). Figure 1.6(b) shows Venera-15 retrieved cyclostrophic wind: the wind exhibits a strong midlatitude jet with a maximum speed of 110 m s^{-1} ; it is also clearly observed that the wind field declines with altitude above the jet. Although the cyclostrophic balance seems to clearly describe the observed state of Venus super-rotation showing that winds are tightly coupled to temperature field, it does not explain

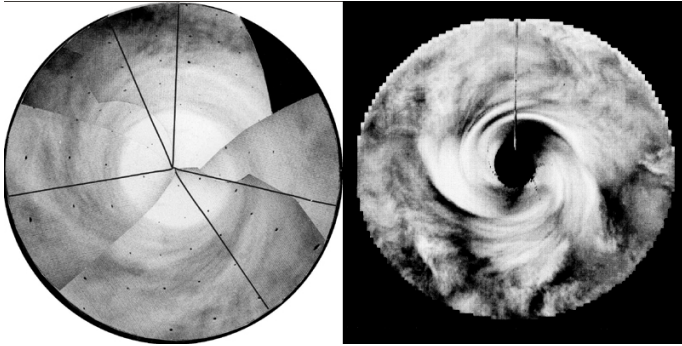


Figure 1.7: Mariner 10 (left) and Pioneer Venus (right) views of Venus south polar vortex (Copyright ESA).

neither what originally brought the atmosphere to this state, nor which mechanisms maintain the vertical wind shear.

Meridional circulation: in addition to the zonal super-rotation, a thermally directed meridional (Hadley) cell flowing from the equator to pole with meridional velocities of less than 10 m s^{-1} has been observed at the cloud top (Fig. 1.5). The meridional circulation is expected to be efficient on Venus in transporting warm air polewards and cooler air equatorwards (Limaye, 1985), it consists of one cell in each hemisphere and it is not limited to the near-equatorial regions like on the relatively-rapidly rotating Earth, where it breaks up in more cells due to the Coriolis force. The vertical extent of the meridional circulation as well as whether it is one large Hadley cell extending from the surface to the cloud level, or a stack of such cells is still unclear. Cloud-tracking observations (Limaye, 2007; Peralta et al., 2007) indicate that the Hadley cell does not extend exactly to the poles but starts to descend at a latitude of about 65° . This is the same latitude where the cold collar has been observed. As mentioned before, the circumpolar collar is a belt of cold air that surrounds the pole; the temperature inside the collar is about 30° colder than the outside region at the same altitude. The resulting pressure differences generated by this feature would tend to dissipate it rapidly, this indicates that it must be continually forced by some unknown mechanism.

Polar Vortex: the combination of the zonal super-rotation and of the meridional flow gives rise at each pole to giant vortices recycling the air downwards rotating with a period of 2.8 (Earth) days (Fig. 1.7). Observations of the North polar vortex acquired by Pioneer Venus showed that the vortex often exhibits a dipole-like shape. More recent results (Taylor and Grinspoon, 2009), however, have shown that the nature of the vortex is much more complex: it assumes often more complicated shapes, as well as monopoles and tripoles. Limaye (2007) first noted similarities between Venus polar vortex and a tropical cyclone on Earth, yet a complete description of the vortex dynamics is still missing and attempts to model the structure and dynamics of the vortex were unsuccessful. Figure 1.8 shows the

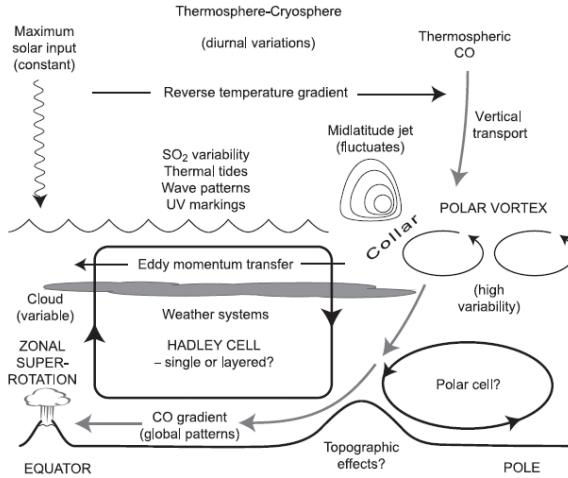


Figure 1.8: Main features which characterise the general circulation on Venus. Question marks indicate some of the questions which still need to be answered (Taylor and Grinspoon, 2009).

main features that characterise Venus circulation and dynamics; the unresolved problems which still need an answer are also shown, this can be synthesised as:

- Which are the processes responsible for maintaining the zonal super-rotation?
- How deep is the Hadley cell and how is it structured?
- How do the polar vortices couple the two main components of the global circulation and why do they have such a complex shape and behaviour?
- How do the midlatitudes jet behaves over time?

1.4 Goals and structure of the thesis

After a pause of more than a decade, Venus atmosphere is being explored again: the first European mission to the planet Venus, Venus Express (VEx), is acquiring new data since 2006. Main objective of the mission is to carry out a remote and in-situ investigation of the atmosphere, plasma environment and surface properties from orbit. Venus Express payload is especially very well suited for atmospheric studies with a special regard to atmospheric dynamics and circulation: atmospheric dynamics is investigated by observing clouds at different levels and by deriving thermal winds from thermal profiles. The Venus Monitoring Camera (VMC) and the Visible and Infrared Thermal Imaging Spectrometer (VIRTIS) on board Venus Express are deriving latitude profile of zonal wind by observing

clouds at several altitudes. Two experiments onboard Venus Express are sounding temperature structure of the Venus mesosphere: VIRTIS sounds the Venus Southern hemisphere in the altitude range 65 – 90 km with a very good spatial and temporal coverage; the Venus Radio Science Experiment (VeRa) observes both north and south hemispheres between 40 – 90 km of altitude with a vertical resolution of ~ 500 m.

The aim of this thesis is to study the dynamics of the Venus mesosphere from the Venus Express observations. Zonal thermal winds have been derived from VIRTIS and VeRa temperature sounding applying an approximation of the thermal wind equation: the cyclostrophic balance. The objectives which have been pursued within the frame of this work are:

- Derivation of the mesospheric thermal wind field in the cyclostrophic approximation from the results of VIRTIS and VeRa temperature soundings;
- Study of the influence of the temperature retrievals uncertainties on the thermal wind field;
- Variability of the mesospheric thermal wind field with latitude, altitude and local solar time;
- Comparison of the wind fields derived from the temperature measurements with the wind speeds from cloud tracking and with results from earlier missions to validate the cyclostrophic hypothesis.

This thesis is organised as follows:

- This chapter gives a brief description of the planet Venus. Special emphasis is given to Venus atmosphere, the dynamics and circulation which characterise the mesosphere.
- Chapter 2 describes the Venus Express spacecraft and its payload. VIRTIS, VeRa and VMC experiments are illustrated in more detail. The scientific objectives of these experiments are explained with special regard to their meteorology studies.
- Chapter 3 illustrates different methods of wind determinations and explains in detail the cyclostrophic approximation.
- Chapter 4 describes the method of thermal wind calculations and its uncertainties, and presents the main results of the thesis.
- Chapter 5 discusses the results of the thesis.

2 Venus Express meteorology observations

2.1 Venus Express mission and payload

Venus Express (VEx) is the first European mission to the planet Venus. The mission aims at a global and long term survey of the atmosphere, the plasma environment and the surface of Venus. The spacecraft is based on the Mars Express design with small modifications needed to accommodate to the conditions at Venus (Svedhem et al., 2007). The Venus Express payload consists of seven experiments. The experiments can be divided in three categories: spectrometers and spectral imagers for remote sensing, plasma and magnetic field instruments for in situ measurements, and the ultrastable oscillator used for radio science. The VEx payload suited very well for meteorology studies. Within the frame of this work temperature profiles retrieved from the Visible and Infrared Thermal Imaging Spectrometer (VIRTIS) and the Venus Radio Science Experiment (VeRa) on board Venus Express have been used to derive thermal winds. Results have then been compared to cloud-tracking winds observed by the Venus Monitoring Camera (VMC) and VIRTIS at different altitude levels. A description of the seven instruments on board Venus Express is given with special emphasis on VeRa, VIRTIS and VMC (Fig. 2.1):

- **VeRa:** The Venus Express Radio Science Experiment performs radio-occultation sounding of the atmosphere: it makes use of radio signals at wavelengths of 3.6 and 13 cm ("X"- and "S"-band, respectively) to probe neutral atmosphere, ionosphere, surface properties and gravity anomalies. In addition, an ultra-stable oscillator (USO) provides a high quality onboard reference frequency source to the spacecraft transponder (Häusler et al., 2006). Radio sounding of the neutral atmosphere provides vertical profiles of density, temperature and pressure in the altitude range 40 – 90 km with a very good latitude coverage. The Venusian ionosphere is probed from ~ 80 km altitude up to the ionopause (< 600 km) to derive the vertical profiles of electron density, to study the interaction between the solar wind and Venus ionopause and to determine the exact altitude of the ionopause. The VeRa surface studies includes bi-static radar sounding and the investigation of the gravity field. The radio measurements also contribute to studies of solar corona structures and solar wind turbulence. VeRa observes near the pericentre; the spacecraft, in order to operate, requires specific geometry which can often preclude the rest of the payload to operate.

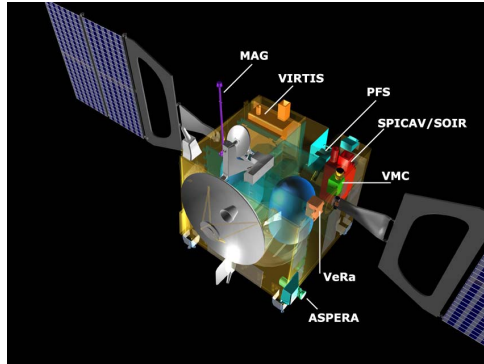


Figure 2.1: Locations of the scientific instruments on the Venus Express spacecraft (Copyright ESA).

- VIRTIS:** The Visible and Infrared Thermal Imaging Spectrometer (VIRTIS) is one of the key experiments on board of Venus Express (Fig. 2.2). It consists of two channels. VIRTIS-M is an imaging spectrometer with moderate spectral resolution ($R \sim 200$) and high spatial resolution (0.25 mrad) operating in the spectral ranges $0.25 - 1 \mu\text{m}$ and $1 - 5 \mu\text{m}$. VIRTIS-H is a high resolution spectrometer ($R \sim 1200$) operating in the spectral range $1.84 - 4.99 \mu\text{m}$ (Drossart et al., 2007). The instantaneous field of view (IFOV) of VIRTIS-M is 0.25×64 mrad, corresponding to about one-third of the diameter of Venus at apocentre. Therefore, VIRTIS requires a 3×3 mosaicing procedure at apocentre to obtain a global observation of the whole planet. At the pericentre, where the spacecraft is only about 350 km above the clouds, imaging with VIRTIS is problematic, thus, observations consist of separate spots scattered along the orbit which give a statistical coverage of the Northern hemisphere. VIRTIS experiment has a broad range of scientific objectives which cover the study of the lower atmosphere composition, the sounding of the mesosphere vertical temperature structure and the investigation of the atmospheric dynamics. VIRTIS measures the wind speeds by tracking the clouds in the UV (~ 70 km, dayside) and IR (~ 50 km, nightside). In addition, it maps the Venus surface in the $1 \mu\text{m}$ "window" on the night side.
- VMC:** Venus Monitoring Camera (VMC) is a CCD-based camera specifically designed to take images of Venus in four narrow band filters in UV (365 nm), visible (513 nm), and near-IR (965 and 1000 nm) range (Markiewicz et al., 2007). Venus Express orbit allows VMC to capture images of Venus with a spatial scale which ranges from a global view of the planet with a resolution of ~ 50 km to close-ups with few hundred meters resolution. High resolution images taken at the pericentre are used to study small-scale dynamical phenomena at the cloud top. Off-pericentre observations provide full disc images for both day and night side of Venus and permit to investigate global atmospheric circulation. The UV channel is centered at the spectral signature of the unknown UV absorber. This filter is used to investigate

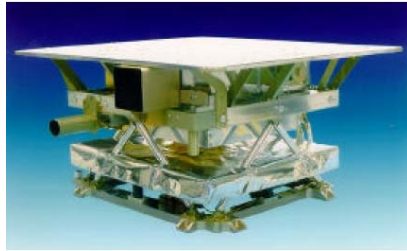


Figure 2.2: Photography of VIRTIS instrument.

the dynamics of Venus atmosphere by tracking motions of cloud features. Maps of the airglow originating at ~ 100 km are obtained from visible images taken on the night side. The near-IR channel centered on the $0.94 \mu\text{m}$ H_2O band sounds the water vapour abundance and distribution at the cloud tops on the day side and in the lower 20 km at night. Night side observations taken in the $1 \mu\text{m}$ transparency "window" provide a thermal mapping of the Venus surface. Structure of the upper clouds and mesospheric hazes are studied in limb geometry.

- **ASPERA:** Analyser of Space Plasma and Energetic Atoms (Barabash et al., 2007).
- **MAG:** Venus Express Magnetometer (Zhang et al., 2006).
- **PFS:** Planetary Fourier Spectrometer (Formisano et al., 2006).
- **SPICAV/SOIR:** Ultraviolet and Infrared Atmospheric Spectrometer (Bertaux et al., 2007).

Venus Express was launched on 9 November 2005 and on 11 April 2006 was inserted in an elliptical polar orbit around Venus, with a pericentre height of ~ 250 km, apocentre distance of $\sim 66,000$ km and an orbital period of 24 hours. Venus Express orbit provides a complete latitude and local solar time coverage and optimises the science return of each instrument on board. The selected orbit is ideal to investigate the dynamics of the atmosphere: it permits to combine global studies of large scale phenomena at the apocentre with detailed studies at high-resolution at the pericentre. The Venus Express orbit can be divided in three parts (Fig. 2.3): pericentre observations (23 – 2 h orbital time), telecommunications (2 – 12 h, descending branch of the orbit), and the apocentre and off-pericenter observations (12 – 23 h, ascending branch). Venus Express modes of observation differ for their science goals, geometry of observations and experiments involved. These can be subdivided in nadir observations, limb observations, and radio occultations. Goals of nadir observations are to obtain high resolution spectroscopic and imaging observations of the North hemisphere, plasma and magnetic field observations in the vicinity of the planet, global view of the Southern hemisphere with particular attention to the investigation of the composition and dynamics of the atmosphere. Limb observations are dedicated to study the vertical structure of the atmosphere. The radio occultation observations study the surface properties and sound the neutral atmosphere

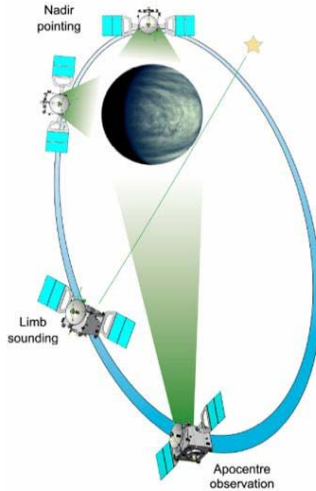


Figure 2.3: Venus Express orbit (Titov et al., 2009).

and ionosphere (Titov et al., 2009).

One of the main mission goals of Venus Express is to study atmospheric dynamics: the quasi-polar orbit provides a complete latitudinal coverage and gives the best compromise for allowing both high-resolution observations near pericenter and global observations during the apoapse part of the orbit. Some of the open problems in Venus atmospheric dynamics can be addressed by detailed observations of winds at various altitudes. Venus Express can quantify the velocities by tracking the motions of the cloud features in the VIRTIS and VMC images corresponding to the altitudes of ~ 50 km, 61 km and 70 km. These observations have been complemented by the thermal wind field retrievals from the temperature sounding by VeRa and VIRTIS. Comparison of simultaneous direct and indirect observations of winds allows to verify the hypothesis of cyclostrophic balance in the Venus atmosphere.

2.2 Sounding of the atmospheric temperature structure

Venus Express exploits two techniques to sound the atmospheric structure of Venus: (1) it sounds the temperature of the middle atmosphere (60 – 100 km) on the night side using spectroscopic observations of the $4.3 \mu\text{m}$ CO_2 bands, with a very good spatial and temporal coverage and a vertical resolution of ~ 3 km (Drossart et al., 2007); and (2) it sounds the temperature in the altitude range 40 – 90 km by radio occultation, providing vertical resolution of a few hundred meters both for the day and night side of the planet (Häusler et al., 2006; Pätzold et al., 2007).

2.2.1 VIRTIS (Visible and Infrared Thermal Imaging Spectrometer)

The spectral distribution of the radiance leaving the top of the atmosphere contains information about the vertical distribution of temperature and the gaseous constituent concentrations in the mesosphere above the clouds. Since atmospheric opacity varies with wavelength and the depth from which emergent radiation is emitted varies with opacity, different depths in the atmosphere are sounded by measurements at different wavelengths (Andrews et al., 1987). Radiation emitted from gases whose distribution is known, such as carbon dioxide, which is nearly uniformly mixed, contains information about temperature only. In order to use an absorption band for temperature sounding some conditions must be satisfied (Houghton et al., 1984):

- The emitting gas should be well mixed in the atmosphere, with known abundance, so that the emitted radiation can be considered a function of the temperature distribution only. This is the case for carbon dioxide (CO₂) and for molecular oxygen (O₂) up to ~ 100 km altitude. Absorption bands due to carbon dioxide occur near wavelengths of 15 μm and 4.3 μm .
- The absorption bands involved should not be overlapped by bands of other atmospheric constituents. This is substantially the case for the bands mentioned above.
- Local thermodynamic equilibrium (LTE) should apply. This requires that the population of the upper state belonging to the absorption band in question should be determined by the Boltzmann factor at the local kinetic temperature. This generally occurs when the probability of excitation by collision is considerably larger than the probability of losing excitation by radiation processes.

Grassi et al. (2008) retrieved vertical profiles of air temperature at 67 pressure levels in the Venusian mesosphere from VIRTIS-M spectra acquired in the region of 4.3 μm CO₂ band. [The following derivations are an excerpt from Grassi et al. (2008)] Once calibrated, the radiation field measured by VIRTIS in orbit around Venus is described by the radiative transfer equation (Hanel et al., 2003):

$$\begin{aligned}
 I_v(\tau_v, \text{total}, \mu, \phi) = & \\
 \text{A. } & \frac{1}{\mu} \int_0^{\tau_v, \text{total}} [1 - \omega_{0,v}(\tau_v = \tau'_v)] e^{-(\tau_v, \text{total} - \tau'_v)/\mu} B_v[T(\tau_v = \tau'_v)] d\tau'_v + \\
 \text{B. } & \frac{1}{4\pi\mu} \int_0^{\tau_v, \text{total}} \int_0^{2\pi} \int_{-1}^1 e^{-(\tau_v, \text{total} - \tau'_v)/\mu} \tilde{p}_v(\tau_v = \tau'_v, \mu, \phi, \mu', \phi') I_v(\tau_v = \tau'_v, \mu', \phi') d\mu' d\phi' d\tau'_v + \\
 \text{C. } & \frac{F_{v,0}}{4\pi} \int_0^{\tau_v, \text{total}} \tilde{p}_v(\tau_v = \tau'_v, \mu, \phi, \mu_0, \phi_0) e^{-(\tau_v, \text{total} - \tau'_v)/\mu} e^{-(\tau_v, \text{total} - \tau'_v)/\mu_0} d\tau'_v + \\
 \text{D. } & \frac{1}{4\pi\mu} \int_0^{\tau_v, \text{total}} \int_0^{2\pi} \int_{-1}^1 e^{-(\tau_v, \text{total} - \tau'_v)/\mu} S_v(\tau_v = \tau'_v, \mu, \phi, \mu', \phi') d\mu' d\phi' d\tau'_v
 \end{aligned} \tag{2.1}$$

Where τ_v is the optical depth, μ is the cosine of the zenith angle θ , ϕ is the azimuthal angle, $\omega_{0,v}$ is the albedo for single scattering, B_v is the Planck function, \tilde{p}_v is the aerosol phase function and $F_{v,0}$ is the solar flux density. The various term of equation (2.1) represent: (A) radiation thermally emitted from the surface and the atmosphere; (B) multiple

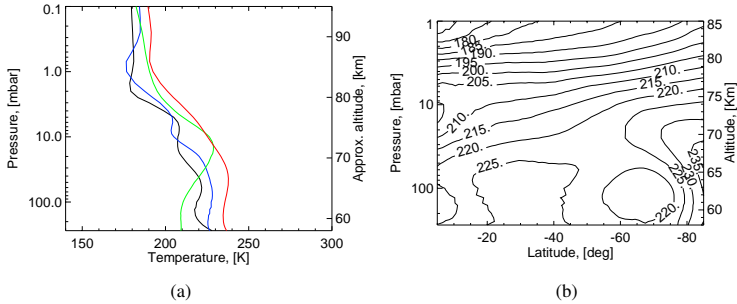


Figure 2.4: (a) VIRTIS vertical temperature profiles at four different latitudes. Colors correspond to the latitudes: (black) 10° ; (blue) 35° ; (green) 65° ; (red) 85° . (b) Contours of temperature field; contour interval is 5 K. For both figures data refer to VIRTIS-M orbit VI0072.

scattering phenomena; (C) reflection of solar radiation; and (D) other non thermal emissions such as radiation due to non-LTE (local thermodynamic equilibrium) phenomena. Term (B) makes equation (2.1) an integral equation. The analytical determination of the expected radiation field is not usually possible, even when a complete knowledge of the vertical distributions of aerosols and gases, air temperature and optical properties of suspended materials are available; therefore the radiation field must be calculated numerically. The inversion of equation (2.1) is thus considered an "ill-posed" problem, often without a mathematically unique solution (Rodgers, 1976).

The VIRTIS temperature sounding covers altitude range from 85 to 65 km (1 – 100 mbar). The overall error in retrieved temperature is $\lesssim 5$ K in the range 100 – 0.1 mbar. The main sources of errors and systematic uncertainties in the temperature retrievals are instrumental noise in the spectral ranges sounding high altitudes and uncertainties in the aerosols densities within the cloud deck (70 – 60 km) (Grassi et al., 2008). The VIRTIS observations analysed in this thesis cover the night side in the Southern hemisphere. The measurements on the day side have non-negligible solar component (Eq. 2.1, term C) and were excluded from our study. VIRTIS-M has acquired about 1120 cubes suitable for temperature retrieval and about 410 out of them have already been processed ($\sim 37\%$ of total). Temperature profiles used for this thesis were selected in order to have a very good latitude coverage (at least 50° wide latitude range) of the Southern hemisphere. Temperature retrieved from 66 orbits were analysed; they cover all latitudes of the Southern hemisphere in the local time range 18 – 06 h. Figures 2.4(a, b) show an example of several typical temperature profiles at different locations and the latitude-altitude temperature field retrieved from the VIRTIS-M observations in orbit 72. Figure 2.5 shows the corresponding latitude dependence of temperature at constant pressure levels. At the cloud top (~ 65 km) an inversion in the vertical temperature profiles is clearly visible between $\sim 45 - 75^\circ$ latitude. Above ~ 70 km altitude an increasing of temperature towards the pole can be observed. Both these features were observed by previous missions (Pioneer

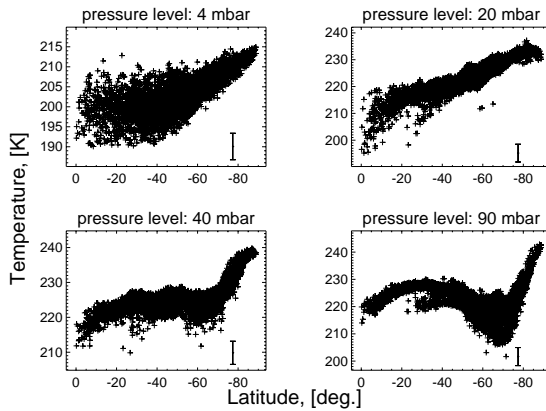


Figure 2.5: Plots of temperature at different pressure levels. Error bar shows random error of air temperature retrieval. Data refer to the VIRTIS-M orbit VI0072.

Venus and Venera-15) and are known as "cold collar" and "warm polar mesosphere" respectively (Taylor et al., 1983; Zasova et al., 2007). The VIRTIS observations in orbit 72 completely covered the night side of the Southern hemisphere, that allowed us to estimate the dependence of temperature field on local time. Figure 2.6 shows latitude profiles of temperatures at selected pressure levels for 2-h local time bins. They suggest that the atmosphere at the cloud top (~ 90 mbar) cools down by about 15 K during the night. Local time-latitude temperature maps at two different pressure levels (35 and 90 mbar) are shown in figures 2.7(a), 2.7(b). At cloud top (90 mbar, ~ 65 km) temperature tends to decrease from dusk to dawn and the cold collar appears particularly pronounced on the dawn side. At higher altitudes (35 mbar, ~ 70 km) temperature slightly increases towards the pole; the atmosphere appears warmer before midnight. Evolution of temperature fields with local time is shown in figure 2.8 where temperatures derived from VIRTIS orbit 72 have been divided in 3-h local time bins. Temperature in the region of the cold collar reaches a maximum value of ~ 225 K just before midnight and then tends to decrease towards the dawn where a minimum value of ~ 215 K occurs.

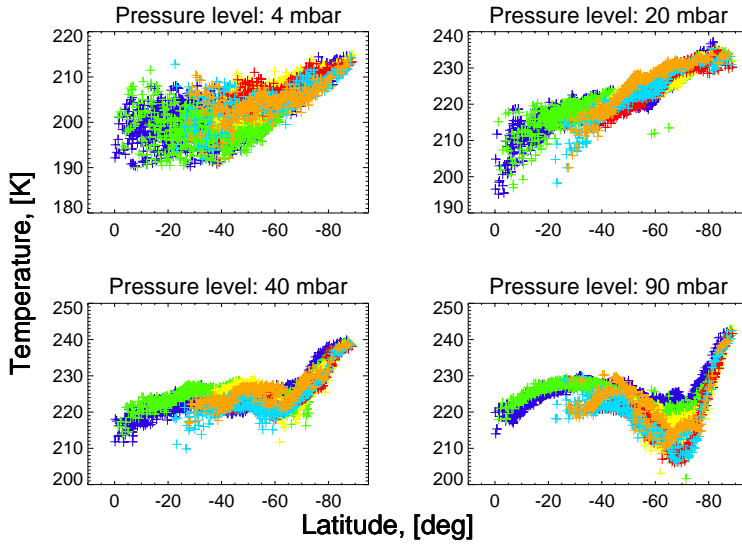


Figure 2.6: Plots of latitude dependence of temperatures at selected pressure levels; different colors correspond to different local time: (blue) 18 – 20 LT; (green) 20 – 22 LT; (yellow) 22 – 24 LT; (red) 00 – 02 LT; (light blue) 02 – 04 LT; and (orange) 04 – 06 LT. Data refers to VIRTIS-M orbit VI0072.

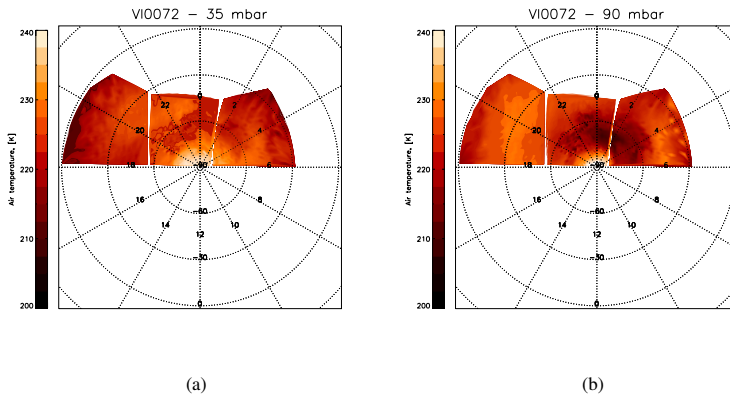


Figure 2.7: Latitude-local time air temperature maps (a) 35 and (b) 90 mbar levels (~ 65 and 70 km). Data refers to VIRTIS-M orbit VI0072. The air temperature (K) is the colour code as shown.

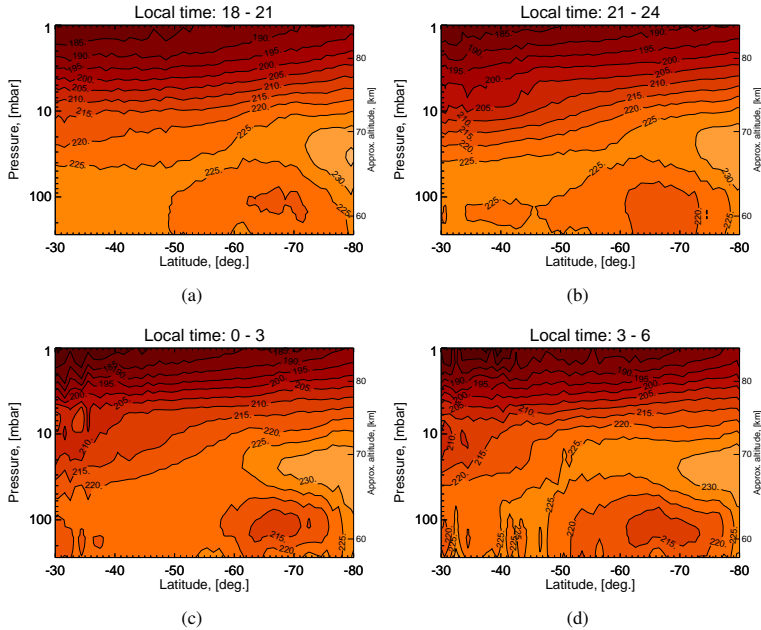


Figure 2.8: Latitude-height cross sections of temperature (K); data refers to five VIRTIS-M orbits acquired between June and July 2006. Data have been divided in four local time bins: (a) 18 – 21 LT; (b) 21 – 24 LT; (c) 00 – 03 LT; and (d) 03 – 06 LT. Contour interval is 5 K.

2.2.2 VeRa (Radio Science Experiment)

The Venus Express Radio Science Experiment VeRa uses one-way radio carrier signals at two coherent frequencies (X-band at 8.4 GHz and S-Band at 2.3 GHz) for the radio sounding of the ionosphere and the neutral atmosphere of the planet ((Häusler et al., 2006) for details). An Ultrastable Oscillator (USO) provides an onboard reference source with a relative frequency stability of $\sim 10^{-13}$. The measurements are performed during so-called "Earth occultation" constellations. As seen from the Earth, the spacecraft disappears behind the planetary disk and emerges on the opposite limb of the planet. The radio signals have to propagate through the ionosphere and the neutral atmosphere of the planet during the entry ("ingress") and the exit ("egress") phases of the occultation event. The propagation path of the radio link is bended in response to the local gradient of the refractive index while the radio link slices through the altitude regions of the planetary ionosphere and atmosphere. This causes a corresponding frequency shift of the radio carrier signal on ground. Figure 2.9 shows VeRa geometry of observation. The data presented herein were recorded at the ground station in the Closed Loop receiver technique with a sample

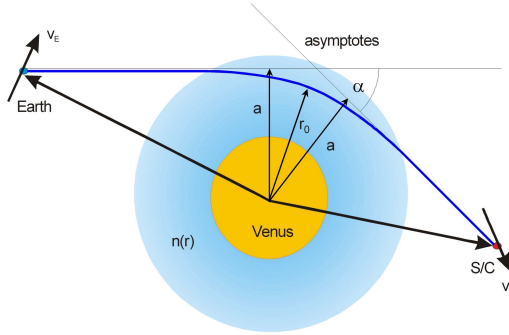


Figure 2.9: VeRa geometry of observation. The angle of deflection α is related to the impact parameter a and the index of refraction $n(r)$ through the Abel transform. The signal penetrates in the atmosphere until it reaches a minimum radius r_0 (Häusler et al., 2006).

rate of 1 sample/s. The standard retrieval method for radio occultations is based on geometrical optics assuming spherical symmetry. The resulting profiles of the bending angle and the ray periaopsis is used to retrieve refractivity profiles $\mu(h)$ as a function of altitude h via an inverse Abel transform (Fjeldbo et al., 1971). In the ionosphere, the electron density is directly proportional to the refractivity profile and the transmitted frequency. VeRa investigations of the ionospheric vertical structure can be found in Pätzold et al. (2007), Pätzold et al. (2008). Below an altitude of approx. 100 km the planetary neutral atmosphere dominates the effect on the radio signal. The neutral number density profile $n(h)$ is directly proportional to the refractivity

$$\mu(h) = C_1 \cdot n(h) \cdot k \quad (2.2)$$

where k is the Boltzmann constant and C_1 is a constant factor depending on the atmospheric composition of the atmosphere (for details see Tellmann et al., 2009). Temperature profiles $T(h)$ are derived assuming hydrostatic equilibrium from Eshleman (1973); Jenkins et al. (1994); Ahmad and Tyler (1997)

$$T(h) = \frac{\mu_{up}}{\mu(h)} \cdot T_{up} + \frac{\bar{m}}{k \cdot n(h)} \int_h^{h_{up}} n(h') \cdot g(h') dh' \quad (2.3)$$

where the mean molecular mass of the atmosphere is given by \bar{m} , $g(h)$ represents the altitude dependent acceleration of gravity (Lipa and Tyler, 1979). The integration constant T_{up} for the temperature at the upper end at 100 km of the sensible atmosphere has to be estimated. Usually, the values $T_{up} = 170$ K, 200 K and 230 K are chosen. Typically, the influence of the selected boundary value is negligible below an altitude of approx. 90 km (Tellmann et al., 2009). The pressure profile is derived from the temperature and the neutral number density by using the ideal gas law. The VeRa profiles are covering the altitude range between approx. 90 and 40 km with an high vertical resolution of only a

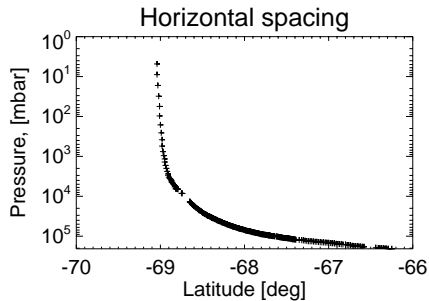


Figure 2.10: Altitude-latitude coverage of a single VeRa temperature profile. Data refers to VeRa orbit 257 egress.

	VIRTIS	VeRa
Vertical resolution	~ 3 km	~ 500 m
Altitude range	65 – 85 km	40 – 90 km
Uncertainties	< 5 K	0.1 – 1 K
Latitudinal coverage	continuous coverage of Southern hem.	good coverage of Southern hem. partial coverage of Northern hem.
Local time coverage	full coverage of nightside	partial coverage of night and dayside
Sensitivity to clouds	Yes	No

Table 2.1: Main properties of temperature retrievals for VIRTIS and VeRa.

few hundred metres. The uncertainties in the retrieved profiles are decreasing with decreasing altitude and are in the order of a fraction of a Kelvin in the temperature profile at the lowest detectable levels (~ 40 km). More than 280 profiles of the ionosphere and the neutral atmosphere could be retrieved during the nominal and first extended mission of Venus Express. First results can be found in Pätzold et al. (2007); Pätzold et al. (2008) and Tellmann et al. (2009). The highly elliptical polar orbit of Venus Express allows to cover almost all latitudes and local times. Measurements in the Northern hemisphere are mainly constrained to high latitudes while the Southern hemisphere is observed with good latitudinal and longitudinal coverage during each occultation season (Häusler et al., 2006; Tellmann et al., 2009). Orbits do not have a common pressure grid, therefore, temperatures were interpolated to a standard pressure grid chosen to retain as much detail of the original data set as possible. As can be discerned from figure 2.10, each vertical temperature profile is spread over more latitudes; the latitude interval can reach a maximum of 8° . Generally, the latitudinal coverage of each vertical temperature profile is retained, however, in order to plot contours of temperature field a nominal location for temperature profiles is taken at the pressure level of 1 bar. Table 2.1 compares the characteristics of VIRTIS and VeRa temperature soundings. For this thesis 116 temperature profiles have been used, they were acquired between December 2006 and January 2009. Figure 2.11 shows the latitude - local time distribution of the observations; data have a very good coverage of the Southern hemisphere, observations in the north hemisphere are

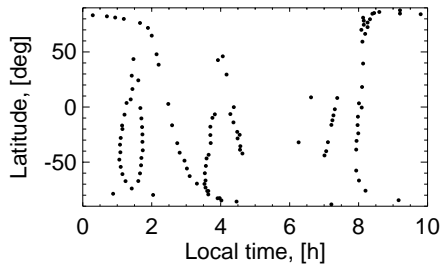


Figure 2.11: VeRa latitude - local time coverage. Data were acquired between December 2006 and January 2009.

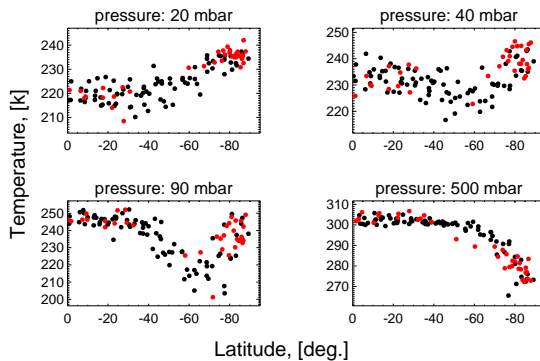


Figure 2.12: Latitude temperature profiles at different pressure levels. Comparison between Northern (red) and Southern (black) hemisphere is shown. Data refers to 116 VeRa profiles acquired between December 2006 and January 2009.

confined to latitudes near the pole. Different local times are covered ranging from late night to early morning. Comparison between observations in the Northern and Southern hemisphere is shown in figure 2.12. In black are represented Southern temperature profiles which have a very good latitudinal coverage. Measurements in the Northern hemisphere (red dots) are especially constrained to the pole. The comparison shows that observations taken in the two hemispheres are very similar. Therefore, hereinafter hemispheric symmetry will be assumed. Venus Express orbital configuration allowed to cover each latitude range at different local times. VeRa temperature profiles were divided in two different groups depending on their local time. Measurements with a local time in the

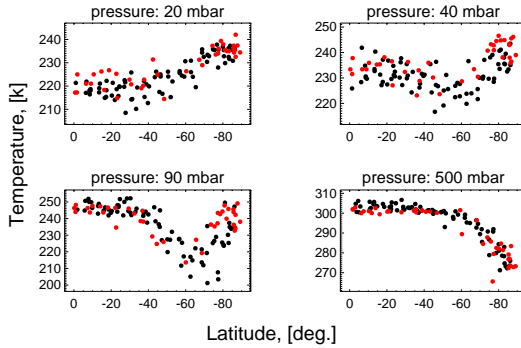


Figure 2.13: Comparison between night (black) and day (red) latitude temperature profiles at different pressure levels.

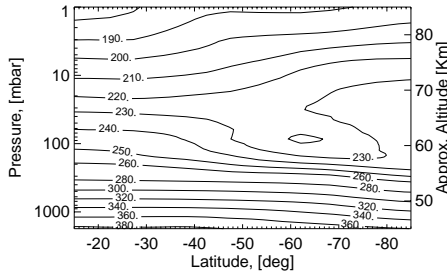


Figure 2.14: Latitude-altitude cross section of VeRa temperature [K] acquired between December 2006 and January 2009. Hemisphere symmetry has been assumed. Contour interval is 10 K.

range [0, 6] were selected as "night" temperatures, while observations covering the local time range [6, 10] were considered "day" temperatures. Figure 2.13 shows the comparison between nightside (black) and dayside (red) observations: it is not possible to discern a trend due to local time. Figures 2.14 and 2.15 show VeRa temperature field and latitude temperature profiles at different pressure levels. Data from Northern and Southern hemispheres and for all local times have been considered. Observations are in a very good agreement with previous radio occultation measurements (Newman et al., 1984). The "cold collar" region can be clearly observed in the latitude range 50 – 75° at the cloud top with a minimum temperature of about 220 K. The warming of the mesosphere towards the pole can be seen above ~ 70 km altitude.

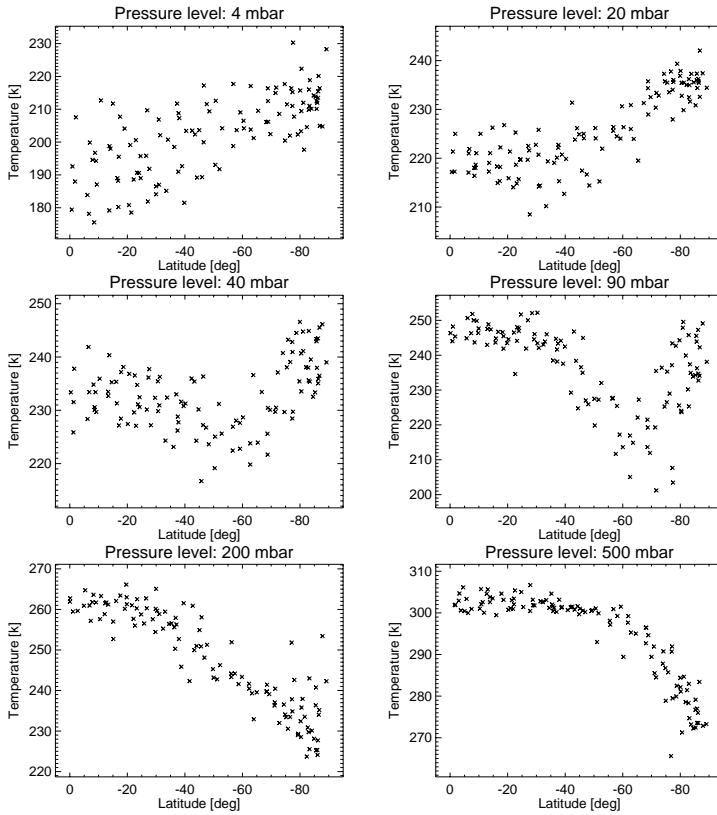


Figure 2.15: Plots of temperature at different pressure levels. Data refers to 116 VeRa profiles acquired between December 2006 and January 2009. Hemisphere symmetry has been assumed.

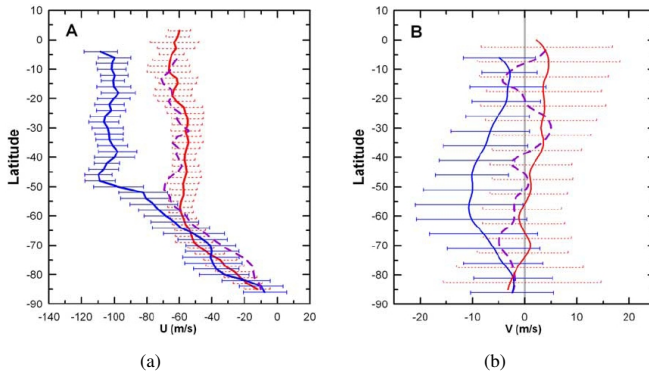


Figure 2.16: Averaged wind profiles derived from VIRTIS images at cloud level. Data refers to VIRTIS orbits acquired between April 2006 - July 2007. Wind was measured using cloud tracers at three different wavelengths: ultraviolet (blue curve, 380 nm; upper cloud, altitude ~ 66 km; day time), near-infrared (violet curve, 980 nm; upper cloud, altitude ~ 61 km; day time), and infrared (red curve, $1.74 \mu\text{m}$; lower cloud, altitude ~ 47 km; night time). Figure (a) corresponds to the latitudinal zonal wind speed profile; figure (b) refers to meridional wind velocity (Sánchez-Lavega et al., 2008).

2.3 Wind velocity measurements

Spectro-imaging instruments onboard Venus Express provide observations of the atmospheric motions at altitudes from the cloud base (~ 50 km) up to the cloud tops (~ 70 km). The wind speeds are derived at ~ 70 km of altitude by tracking the UV markings in IRC images and within the clouds (~ 48 km; ~ 61 km; and ~ 66 km) by observing near-IR cloud features on the night side in VIRTIS images (Moissl et al., 2009; Sánchez-Lavega et al., 2008).

2.3.1 VIRTIS (Visible and Infrared Thermal Imaging Spectrometer)

For the first time it has been possible to derive winds from images acquired by the same instrument at three different wavelengths in order to sound the cloud layers at three different altitude ranges (Sánchez-Lavega et al., 2008). Images in the ultraviolet at the wavelength of 380 nm were used to sound wind speed at the cloud top, in the altitude range of 62 – 70 km. In the near infrared at 980 nm winds can be inferred within the cloud layer in the altitude range of 58 – 64 km. Night side images of Venus at the wavelength of $1.74 \mu\text{m}$ observe within a nominally altitude range of ~ 44 – 48 km. It must be emphasised, however, that there is an uncertainty in the altitude of the cloud features observed at each wavelength due to a lack of knowledge of the cloud vertical structure variability. Figures 2.16(a,b) show the averaged wind speed profile as a function of latitude. Data refers to VIRTIS images acquired between April 2006 and June 2007 and have a very good cover-

	Pericenter	Off-pericenter	Apocenter
Distance	250 – 10, 000 km	10, 000 – 50, 000 km	50, 000 – 66, 000 km
Total field of view	70 – 3000 km	3000 – 14, 000 km	14, 000 – 20, 000 km
Spatial resolution	0.2 – 7 km	7 – 35 km	35 – 48 km

Table 2.2: VMC observations types.

age of the Southern hemisphere. Average zonal wind velocity profiles are shown in figure 2.16(a), they present the same general behaviour at all altitudes. At the cloud top (~ 66 km altitude) zonal wind is constant from the equator to $\sim 50^\circ$ latitude with a speed of $\sim 102 \pm 10$ m s^{-1} ; a strong decrease of wind to zero towards the pole is then observed. Within the clouds, at ~ 61 km and ~ 47 km altitude, the wind velocity is respectively $\sim 62 \pm 10$ m s^{-1} and $\sim 60 \pm 10$ m s^{-1} between the equator and $\sim 55^\circ$ latitude and then decreases to zero velocity at the pole. From the measured wind velocities vertical wind shear has been calculated as: $\partial\langle u \rangle / \partial z$. In the latitude range $0^\circ - 55^\circ S$ vertical wind shear is 8 ± 2 m s^{-1} per km between 61 – 66 km altitude and < 1 m s^{-1} per km in the altitude range $\sim 47 - 61$ km. At sub-polar latitudes the vertical wind shear is weaker, ~ 2 m s^{-1} per km. Comparison with previous measurements obtained by entry probes and Vega balloons are in very good agreement (Schubert, 1983). The meridional component of the velocity is shown in figure 2.16(b) for the three altitudes. At ~ 66 km of altitude it reaches a maximum value of 10 m s^{-1} at $\sim 55^\circ$ latitude. At 61 and 47 km it remains below 5 m s^{-1} . The measurement error is ± 9 m s^{-1} , therefore any conclusion on meridional wind should be taken carefully. VIRTIS data cover the local time range 7 – 17 h, the dependence of wind on local time was analysed and a thermal solar tide was found in the latitude range $50 - 75^\circ S$ which results in increase of the zonal wind speed of 2.5 ± 0.5 m s^{-1} hr^{-1} from the morning (9 h local time) to the afternoon (15 h). A more detailed description of winds tracking clouds in VIRTIS images can be found in Sánchez-Lavega et al. (2008).

2.3.2 VMC (Venus Monitoring Camera)

Moissl et al. (2009) used VMC UV images taken in 365 nm filter to track the UV cloud markings on the dayside to determine the winds at the cloud tops (~ 70 km). The observed dark markings in the ultraviolet (UV) spectral range are caused by inhomogeneous distribution of the yet unknown absorbers. The UV patterns in the clouds are seen where optical depth in the UV approaches unity, this correspond to an altitude of 65 – 70 km (pressure level 40 – 50 mbar) (Esposito et al., 1983). VMC provided the possibility to investigate the global dynamics with a high resolution in space and time; both hemispheres of the planet were covered. Images used for the cloud tracking were acquired when the spacecraft was at a distance of 60, 000 – 26, 000 from the planet. This configuration corresponds to the apocentric and ascending branch of the spacecraft orbit; coverage of the planet in this configuration ranges from about $10^\circ N$ to $80^\circ S$ in latitude and 8 – 16 h local time. VMC spatial resolution depends on the distance of the spacecraft from the planet: around apocenter the resolution ranges between 35 – 48 km per pixel, while at pericenter the resolution can reach a value of 0.2 – 7 km (Table 2.2). Apocentric images provide a view of Venus from beneath the south pole and are used to study near-polar global dynamics. In the ascending branch VMC observes middle and low latitudes in the nadir geometry; ascending branch images are mainly used to track winds from medium and

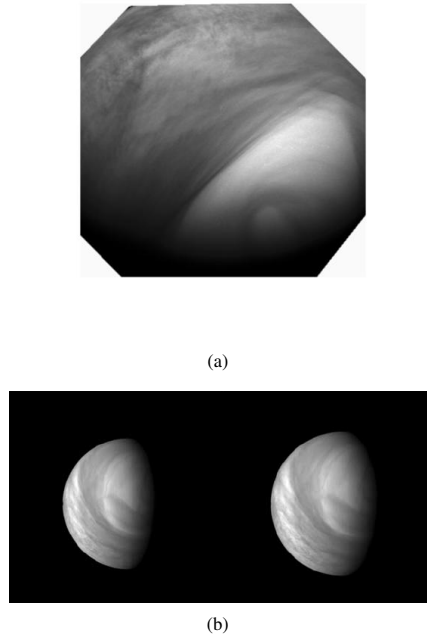


Figure 2.17: Examples of VMC UV images used for cloud tracking.

small-scale features. At distances closer than 10,000 km the rapid motion of the spacecraft does not permit to acquire images suitable to track cloud markings, however, the high spatial resolution allows to study the fine structure of dynamics features.

Figure 2.17 shows example of VMC UV images used to track clouds. Different methods have been used to track cloud features, these can be divided in digital (automatic) and visual (manual) tracking. Figure 2.18 shows average zonal wind profiles obtained from different tracking methods. Wind speeds obtained with different methods show a good agreement at low-mid latitudes, however, a bigger difference is observed at high latitudes. Main reason of this disagreement is more due to difficulties in finding adequate features for tracking at high latitudes than to differences in the tracking methods. A zonal wind speed of $85 - 90 \text{ m s}^{-1}$ almost constant with latitude is observed at low latitudes. The latitude zonal wind profile shows a gradually increase reaching 100 m s^{-1} at $\sim 45^\circ\text{S}$, indicating the presence of a weak midlatitude jet. South of this latitude the wind speed decreases to zero toward the pole. Error bars represented in figure 2.18 are the standard deviation of the zonal wind speed in each latitude bin. The deviation increases toward

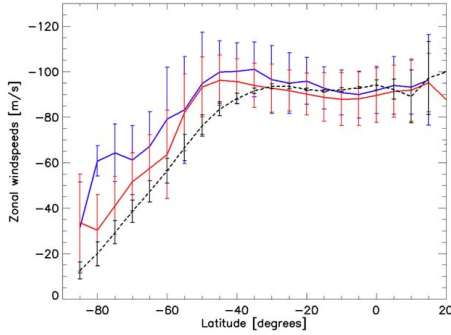


Figure 2.18: Latitude zonal wind profiles derived from cloud tracking of VMC UV images. Curves correspond to different tracking methods: paired visual tracking (red line), sequential visual tracking (blue line), and digital tracking (black line). Errors bars represent standard deviation due to uncertainties of individual measurements (Moissl et al., 2009).

higher latitudes, mostly due to change in morphology and difficulties in finding well defined UV markings. Figure 2.19 shows result for the meridional wind. Meridional wind speeds are found to slightly increase from about -5 m s^{-1} at the equator to a peak value of $\sim -10 \text{ m s}^{-1}$ between 40 and 50°S and then to decrease again toward the pole. This result is consistent with previous measurements and is in agreement with the assumption of a Hadley cell circulation between the equator and the mid latitudes (Schubert, 1983). However, large uncertainties on meridional wind speed require to take any conclusion on latitude variability cautiously. VMC local time coverage allows to investigate the dependence of zonal wind on local time (Fig. 2.20). It has been found a minimum speed at $\sim 11.5 \text{ h}$ upstream of the subsolar point, wind speed then accelerates in the afternoon at low latitudes. At middle latitudes zonal winds appear higher on average and show less local time variability. At higher latitudes south of 60°S an increase of speed with local time is clearly observed. Figure 2.21 compares zonal wind profiles derived from VMC with those retrieved from VIRTIS UV images. Wind profiles derived from both experiments are in good agreement although between $0 - 40^\circ$ latitude VIRTIS shows systematically stronger winds by $\sim 10 \text{ m s}^{-1}$.

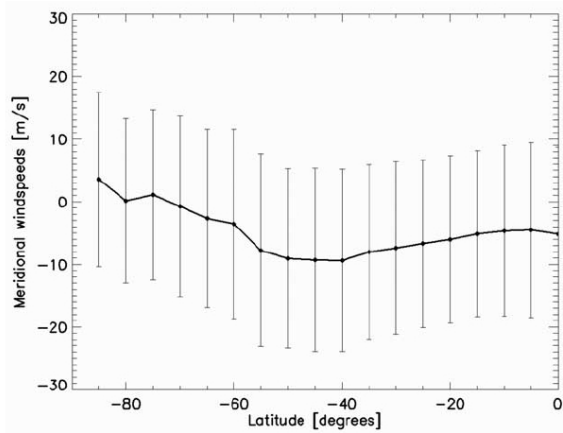


Figure 2.19: Average meridional wind profile obtained from VMC UV cloud tracking. Error bars represent RMS deviation of measurements in one bin (Moissl et al., 2009).

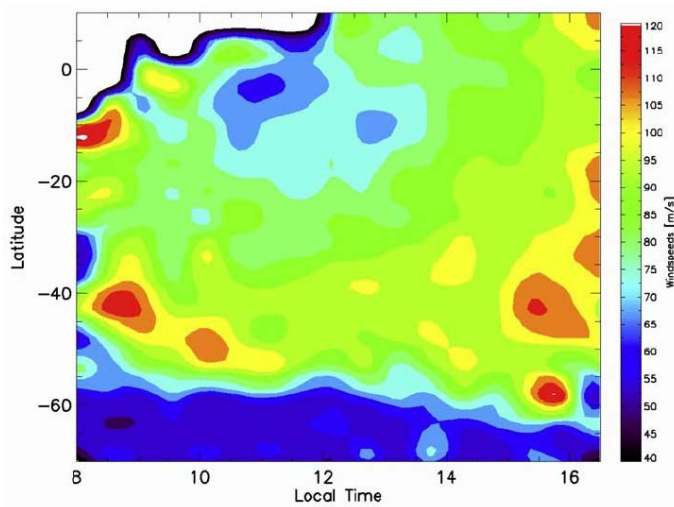


Figure 2.20: Local time - latitude cross section of zonal wind. (Moissl et al., 2009).

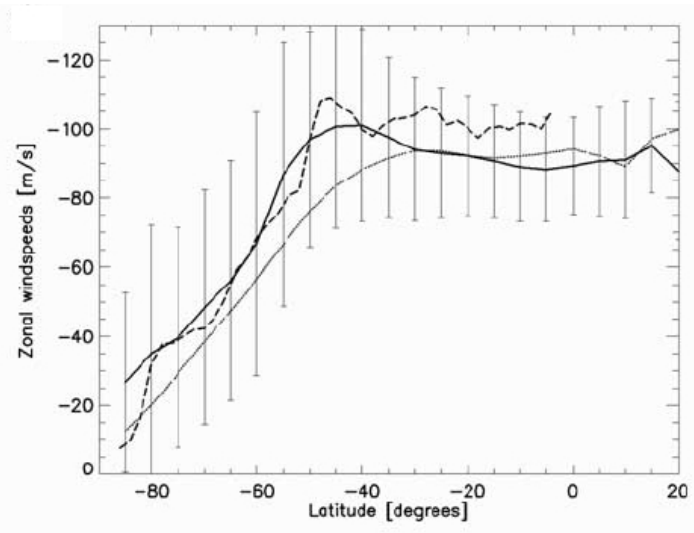


Figure 2.21: Average zonal wind speed profiles from VMC visual (solid line) and digital (dotted line) (Moissl et al., 2009) in comparison with data from VIRTIS (dashed line) (Sánchez-Lavega et al., 2008).

3 Methods of wind determination

3.1 Wind determinations

Different techniques have been used to obtain direct observations of wind at various altitudes: tracking of clouds in ultraviolet (UV) and near infrared (NIR) images can give information on wind speed at cloud top (~ 70 km altitude) (Moissl et al., 2009; Sánchez-Lavega et al., 2008) and within the clouds (~ 47 km, ~ 61 km) (Sánchez-Lavega et al., 2008) while groundbased measurements of Doppler shift in CO₂ band at $10 \mu\text{m}$ (Sornig et al., 2008) and in several CO millimeter lines (Rengel et al., 2008) provide wind speeds above the clouds up to ~ 110 km of altitude. The deep atmosphere from the surface up to the cloud top has been investigated through the Doppler tracking of descent probes and balloons (Counselman et al., 1980; Preston et al., 1986; Kerzhanovich and Limaye, 1985). At altitudes where direct observations of wind cannot be made it is possible to derive zonal wind speeds using an approximation of the thermal wind equation, the cyclostrophic balance, directly from the temperature field measured remotely from orbit (Fig. 3.1).

3.1.1 Direct measurements

3.1.1.1 Cloud-tracking winds

Images taken at different wavelengths allow to investigate the circulation of Venus mesosphere at the cloud top and within the clouds by tracking apparent motions of cloud features. A dataset of high resolution images was obtained by different spacecrafts, however, the limitations in their spatial and temporal coverage have so far prevented to obtain a complete understanding of the general circulation within the cloud layers. Venera 9 orbiter (Kerzhanovich and Limaye, 1985), Mariner 10 (Limaye and Suomi, 1981) and Galileo (Peralta et al., 2007) flybys were limited in temporal coverage; Pioneer Venus orbiter obtained over three years the most extensive dataset, however, the cloud-tracking was mainly at a single wavelength (365 nm) (Rossow et al., 1980; Limaye, 2007). At present, Venus Express (Moissl et al., 2009; Sánchez-Lavega et al., 2008) is investigating the dynamics of Venus with a very high resolution in space and time at different altitude levels within the cloud cover. At the cloud top (~ 65 km) winds have been inferred from tracking of UV markings in ultraviolet images. Near-infrared images allow to sound the atmosphere within the cloud layer: at 980 nm the base of the upper cloud within an altitude range 58 – 64 km is investigated; nightside images of Venus acquired at wavelengths of 1.74 and $2.3 \mu\text{m}$ allow to sound the lower cloud level at ~ 48 km of altitude. There is uncertainty in the altitude of the cloud features observed at each wavelength because of

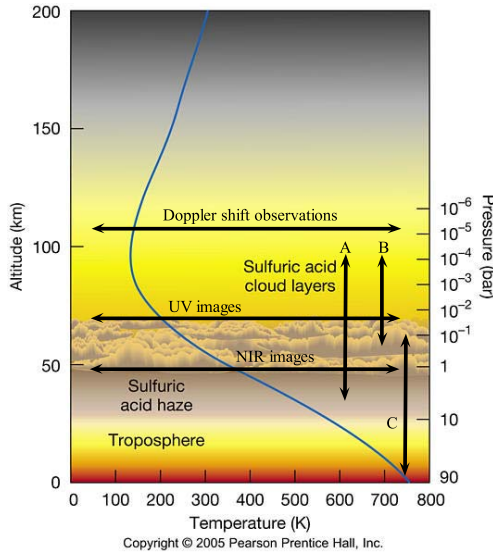


Figure 3.1: Simple scheme of Venus atmosphere. Black arrows show approximately altitudes where direct observations of wind are available. Arrows (A) and (B) indicate respectively altitude ranges of thermal wind calculations from occultation and thermal emission spectroscopy temperature sounding. Arrow (C) covers the altitude range investigated by descent probes and balloons.

lack of knowledge of the cloud vertical structure variability (Rossow et al., 1990). The method used to determine cloud’s altitudes is described in detail in Sánchez-Lavega et al. (2008). There are two general approaches for the cloud tracking: manual tracking of cloud features, conducted by human experimenters, and automatic tracking, executed by a recognition algorithm. To infer the motion of the atmosphere, cloud features on images are identified and their position is determined. Displacement of features on pairs or sequences of images is then measured and the zonal and meridional components of the cloud level flows are calculated as:

$$u(\lambda, \varphi, t) = \frac{\Delta\lambda \cdot R_c}{\Delta t} \cos \varphi; \quad v(\varphi, t) = \frac{\Delta\varphi \cdot R_c}{\Delta t}$$

where u and v are the zonal and meridional wind speed components, $\Delta\lambda$ and $\Delta\varphi$ are longitudinal and latitudinal displacement between images, R_c is defined as $R_c = a + z$, where a is the Venus radius and z is the altitude, and Δt is the time between images. Accuracy of wind speed measurements is affected by uncertainty in the altitude of the cloud features observed at each wavelength, image resolution, measurement accuracy and possible bias from different methods or observers. Figure 2.18 in chapter 2 shows an example of cloud tracked winds derived from VMC ultraviolet images at ~ 70 km altitude (Moissl et al., 2009).

<i>Alt. (km)</i>	$v_{zonal}^{equatorial}$ (m/s)	$v_{zonal}^{highlat.}$ (m/s)	v_{max} (m/s)	<i>Year</i>	<i>Citation</i>
110	25±15	–	120±30	1985 – 1987	Goldstein et al. (1991)
	130±15	–	95±15	1991	Lellouch et al. (1994)
	39.6±2.6	–	118.5±1.5	1990	Schmuelling et al. (2000)
	34.7±1.1	–	129.2±1.2	1991	Schmuelling et al. (2000)
	3±7	< 32±4	52±9	2007	Sornig et al. (2008)
105	–	–	90±12	1991	Lellouch et al. (1994)
99	–	132±10	40	1988	Shah et al. (1991)
	60±15	–	65±15	1991	Lellouch et al. (1994)
95	–	–	40±15	1991	Lellouch et al. (1994)
74	75	–	–	2001 and 2002	Widemann et al. (2007)
67	–	–	40±22.5	2001 and 2002	Widemann et al. (2007)

Table 3.1: Overview of ground-based wind measurements on Venus probing different altitudes from 67 to 110 km (Sornig et al., 2008).

3.1.1.2 Doppler shifts measurements

Above the clouds, where diagnostic cloud features are absent, ground-based measurements of Doppler shifts on molecular lines provide the possibility to probe the upper mesosphere/lower thermosphere. The motion of an air mass along the line of sight induces a frequency shift in the centre of the observed molecular line. From the comparison of the observed spectra to a synthetic spectra is possible to evaluate the shifts and thus to evaluate the global wind field. In order to exactly measure the line position a very high spectral resolution is required. Generally, wind velocities retrieved with this method are a combination of zonal and subsolar-to-antisolar (SS-AS) flows. In order to discriminate between the different dynamical contributions an accurate choice of the location of observations is required: SS-AS flow velocity is low near the subsolar point, where zonal winds can be more easily inferred. Molecular lines used to derive direct observations of wind in the mesosphere/lower thermosphere are visible and 10 μm lines of CO_2 , millimeter and 4.7 μm lines of CO. Visible observations probe primarily near the cloud tops (Widemann et al., 2007), while 10 μm CO_2 sounds altitudes near ~ 110 km (Sornig et al., 2008), within the transition region where the circulation is a combination of the zonal super-rotation and the SS-AS flow. Millimeter measurements of CO probe the mesosphere/thermosphere at $\sim 95 - 105$ and $\sim 105 - 120$ km altitude depending on the observed isotope (Rengel et al., 2008). Since Doppler shifts measurements are obtained only in ground-based observations, they lack a good spatial resolution. Table 3.1 gives an overview of previous observations.

3.1.1.3 Doppler tracking of balloons and descent probes

The Doppler tracking of entry probes and balloons provides the possibility to investigate the dynamics of the deep atmosphere of Venus from the surface up to ~ 65 km of altitude. So far, 15 descent probes have successfully measured vertical profiles of winds in the lower atmosphere, covering low and midlatitudes (-3° to 59°), and 0 to 14h local solar time (Table 3.2). Due to aerodynamic properties, the Pioneer and Venera probes could acquire the horizontal velocity of the atmosphere to within a few m s^{-1} only beneath 60 km of altitude, thus, in the altitude range 60 – 68 km between the vertical profiles from the probes and the ultraviolet cloud-tracking level, direct observations of winds are not

<i>Probe</i>	<i>Date</i>	<i>Lat. (deg.)</i>	<i>Lon. (deg.)</i>	<i>Local solar time</i>	<i>Solar zenith angle (deg.)</i>
Venera 4	Oct 18, 1967	19	38	4:40	110
Venera 5	May 16, 1967	-3	18	4:12	117
Venera 6	May 17, 1969	-5	23	4:18	115
Venera 7	Dec 15, 1970	-5	351	4:42	117
Venera 8	Jul 22, 1972	-10	335	6:24	85
Venera 9	Oct 22, 1975	32	291	13:12	36
Venera 10	Oct 25, 1975	16	291	13:42	28
Venera 11	Dec 25, 1978	-14	299	11:10	17
Venera 12	Dec 21, 1978	-7	294	11:16	20
Venera 13	Mar 1, 1982	-7.5	303	9:27	38
Venera 14	Mar 5, 1982	-13.4	310.2	9:54	33
Vega 1	Jun 11, 1985				
Vega 2	Jun 15, 1985				
Pioneer:					
Large	Dec 9, 1978	4.4	304.0	7:38	65.7
North	Dec 9, 1978	59.3	4.8	3:35	108.0
Day	Dec 9, 1978	-31.7	317.0	6:46	79.9
Night	Dec 9, 1978	-28.7	56.7	0:07	150.7
Bus	Dec 9, 1978	-37.9	290.9	8:30	60.7

Table 3.2: Atmospheric entry probes locations and times (Kerzhavovich and Limaye, 1985).

reliable (Gierasch et al., 1997). At altitudes less than 55 km the probes give the horizontal wind to within about 1 m s^{-1} , with an altitude resolution of 1 km deep in the atmosphere and a few km near 55 km of altitude (Counselman et al., 1980). Figure 1.6(a) in chapter 1 shows the vertical profiles of zonal winds measured from Pioneer and Venera probes. These data show that the east-to-west rotation is predominant at all altitudes between ~ 10 km and the cloud tops; winds increase in speed with altitudes from $\leq 10 \text{ m s}^{-1}$ at 10 km to 100 m s^{-1} at cloud level. Below 10 km of altitude both zonal and meridional wind speeds are only few m s^{-1} ; however, measurements in the deep atmosphere are too scarce to draw any conclusion. In addition, tracking of the VEGA balloons has provided the first continuous record of atmospheric motion over two days each (Preston et al., 1986; Kerzhavovich and Limaye, 1985). The two Vega balloons sampled the large-scale flow at about 53 km of altitude and at latitudes of about $\pm 7^\circ$. They were inserted four days apart and each drifted for approximately two days, covering more than 100° of longitude, in the altitude range 50 – 55 km. The balloons measured a east-west velocity of about 65 m s^{-1} , in good agreement with measurements from descent probes (Crisp et al., 1990).

3.1.2 Thermal winds

In regions of the mesosphere between 45 – 85 km of altitude, where direct measurements are not available (Fig. 3.1), the only method to acquire informations on the circulation is to derive the zonal wind field from vertical temperature profiles. Earlier studies (Newman et al., 1984; Roos-Serote et al., 1995; Zasova and Khatountsev, 1997) have proved that the strong zonal winds near the cloud top are well described by the thermal wind equation, which directly relates the zonal winds to the mesospheric temperature field. The thermal wind equation is obtained assuming the cyclostrophic approximation, which consists in

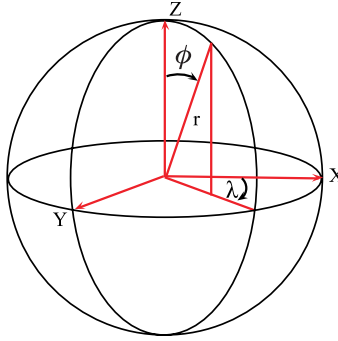


Figure 3.2: Spherical coordinate system (λ, ϕ, z) , where λ is longitude, ϕ is latitude and z is altitude. In the figure r is the distance to the center of the planet and is related to z by $r = a + z$, where a is the radius of the planet.

the balance between the equatorward component of the centrifugal force and the poleward component of the pressure gradient force. Figure 3.1 shows that the altitude range where thermal winds can be derived partially overlaps with heights at which cloud-tracked winds can be inferred. Therefore, simultaneous wind tracking and temperature sounding can be used to validate the cyclostrophic assumption. In the next section a more detailed description of the cyclostrophic balance is given.

3.1.2.1 Thermal wind equation and cyclostrophic balance

The motion of a fluid parcel is described by the Navier-Stokes equation (or momentum equation). In a rotating frame of reference, the general form of the equation of fluid motion is (Holton, 2004):

$$\frac{D\mathbf{U}}{Dt} = -2\boldsymbol{\Omega} \times \mathbf{U} - \frac{1}{\rho}\nabla p + \mathbf{g} + \mathbf{F}_r \quad (3.1)$$

where D/Dt is the material derivative defined as $D/Dt = \partial/\partial t + \mathbf{U} \cdot \nabla$, \mathbf{U} is the fluid's velocity, $\boldsymbol{\Omega}$ is the angular velocity of the coordinate system, ρ is the density of the fluid, ∇p is the pressure gradient, \mathbf{g} is the gravitational field and \mathbf{F}_r designates the frictional force. The first term on the right side of equation (3.1) is the Coriolis term which applies particularly to moving particles in rotating frames. For purposes of theoretical analysis and numerical prediction, it is convenient to expand the vectorial momentum equation (3.1) into its scalar components. A convenient set of axes at any point on a planet's surface is the spherical coordinate system, whose coordinate axes are (λ, ϕ, z) , where λ is longitude, ϕ is latitude and z is altitude (Fig. 3.2). The unit vectors are defined such as \mathbf{i} is directed towards the east, \mathbf{j} towards the north and \mathbf{k} vertically upwards. If u, v, w are the components of the velocity \mathbf{U} in the $\mathbf{i}, \mathbf{j}, \mathbf{k}$ directions respectively, x and y are defined as the eastward and the northward distance then equation (3.1) can be written in component form as follows (for a more detailed description see: Andrews, 2000; Holton, 2004; Houghton, 2002):

Scale	Symbol	Venus	Earth
Vertical scale	H	15.9 km $\approx 10^4$ m	~ 10 km
Zonal velocity	U	~ 100 m s $^{-1}$	~ 10 m s $^{-1}$
Meridional velocity	V	~ 10 m s $^{-1}$	~ 10 m s $^{-1}$
Vertical velocity	W	≤ 1 m s $^{-1}$	~ 1 cm s $^{-1}$
Radius	a	$\sim 6.0 \times 10^6$ m	$\sim 6.0 \times 10^6$ m
Rotation rate	Ω	2.99×10^{-7} rad s $^{-1}$	7.29×10^{-5} rad s $^{-1}$
Acceleration of gravity	g	8.8 m s $^{-2}$	9.81 m s $^{-2}$
Timescale	T	$\sim 10^6$ s	$\sim 10^5$ s

Table 3.3: Scales characteristic of Venus mesosphere (Kerzhanovich and Limaye, 1985) and of Earth atmosphere (Holton, 2004).

$$\frac{Du}{Dt} - \frac{uv \tan \phi}{r} + \frac{uw}{r} = -\frac{1}{\rho} \frac{\partial p}{\partial x} + 2\Omega v \sin \phi - 2\Omega w \cos \phi + F_{rx} \quad (3.2)$$

$$\frac{Dv}{Dt} + \frac{u^2 \tan \phi}{r} + \frac{vw}{r} = -\frac{1}{\rho} \frac{\partial p}{\partial y} - 2\Omega u \sin \phi + F_{ry} \quad (3.3)$$

$$\frac{Dw}{Dt} - \frac{u^2 + v^2}{r} = -\frac{1}{\rho} \frac{\partial p}{\partial z} - g + 2\Omega u \cos \phi + F_{rz} \quad (3.4)$$

Where ϕ is the latitude and r is defined such as $r = a + z$, where z is the vertical distance from the planet's surface and a is Venus radius. The complete equations of motion [(3.2) – (3.4)] describe all types and scales of atmospheric motions. These equations are complicated, but approximate versions are sufficient for modelling many atmospheric dynamical phenomena. The magnitudes of the various terms in equations (3.2) – (3.4) will be very different depending on the scale of the motion under study. In table (3.3) are given some characteristic scales valid for Venus mesosphere.

The following simplifications can be made:

- In the first place, it is possible to replace the distance r by Venus radius a with a negligible error; since Venus neutral atmosphere has a depth of ~ 200 km it can be considered thin compared to its radius $a \approx 6052$ km.
- The molecular friction term \mathbf{F}_r has an order of magnitude of $\sim 10^{-12}$ m s $^{-2}$ and can be neglected for all motions except the smallest scale turbulent motions near the ground.
- As can be seen in table (3.3), vertical velocities are very much smaller than horizontal velocities, so that, in the momentum equations (3.2) – (3.4) terms involving w can, to a first approximation, be neglected. Such motion is said to be *horizontal*.
- In Venus mesosphere the meridional wind component v is smaller than the zonal wind component u of an order of magnitude, it is possible, thus, to a first approximation, to consider the circulation on Venus as a purely zonal motion and to neglect all terms involving v .

Term in eq. (3.2) – (3.4)	Venus (m s ⁻²)	Earth (m s ⁻²)
$\frac{u^2}{a}$	10 ⁻³	10 ⁻⁵
$2\Omega u \cos \phi$	10 ⁻⁵	10 ⁻³
$\frac{Du}{Dt}$	10 ⁻⁴	10 ⁻⁴
$\frac{u^2 \tan \phi}{r}$	10 ⁻³	10 ⁻⁵
$2\Omega u \sin \phi$	10 ⁻⁵	10 ⁻³
$-\frac{1}{\rho} \frac{\partial p}{\partial y}$	10 ⁻³	10 ⁻³
\mathbf{F}_r	10 ⁻¹²	10 ⁻¹²

Table 3.4: Scales analysis of the momentum equation.

- Consider now equation (3.4), the terms $\frac{u^2}{a}$ ($\sim 10^{-3}$ m s⁻²) and $2\Omega u \cos \phi$ ($\sim 10^{-5}$ m s⁻²) are very much smaller than $g = 8.8$ m s⁻². Eventually, we obtain:

$$\frac{\partial p}{\partial z} = -g\rho$$

The vertical momentum equation (3.4) reduces thus to *hydrostatic balance*.

- For a zonal wind the timescale of $\frac{Du}{Dt}$ can be considered, to a first approximation, the seasonal timescale of the planet (Zhu, 2006). Although Venus orbital period is ~ 224 Earth days, its orbit obliquity ($\sim 177^\circ$) and eccentricity (0.0067) are small compared to the Earth's; thus, Venus seasonal timescale can be approximated to 90 Earth days ($\sim \frac{1}{4}$ Earth year). In the equation (3.2), the term $\frac{Du}{Dt}$ can be written as:

$$\frac{Du}{Dt} = \frac{\partial u}{\partial t} + u \frac{\partial u}{\partial x} \sim \frac{U}{T} + \frac{U}{T} \sim 10^{-4} \text{ms}^{-2}$$

which, to a first approximation, can then be neglected.

With these assumptions, summarised in table 3.4, equations (3.2) – (3.4) reduce to:

$$\frac{u^2 \tan \phi}{r} + 2\Omega u \sin \phi = -\frac{1}{\rho} \frac{\partial p}{\partial y} \quad (3.5)$$

Equation (3.5) is the *general thermal wind equation*; it is a powerful tool to investigate the dynamics and circulation of planetary atmospheres. The equation assumes the balance between the meridional pressure gradient force and the sum of the horizontal components of the Coriolis and centrifugal force. For large-scale atmospheric motions on quickly rotating planets like Earth and Mars the Coriolis force is approximately balanced by the pressure gradient (Table 3.4), this is known as the *geostrophic approximation*. Geostrophic winds have proved to be a good approximation on both planets (Zurek et al., 1992; Holton, 2004). In the mesospheres of slowly rotating planets, like Venus and Titan, strong zonal winds are assumed to be in *cyclostrophic balance* (Leovy, 1973; Flasar et al., 2005). This suggests equality between the equatorward component of the centrifugal force and the meridional pressure gradient force (Fig. 3.3, Table 3.4). [The following

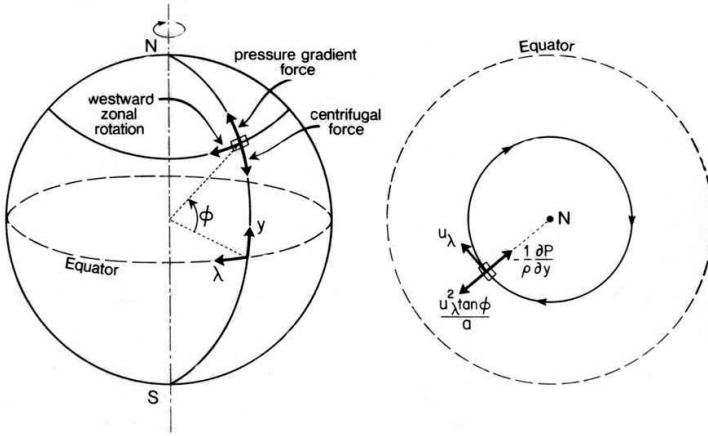


Figure 3.3: Forces acting on a rotating atmospheric parcel in cyclostrophic balance (Schubert, 1983).

is an excerpt from Newman et al. (1984)]. The cyclostrophic balance can be written as:

$$\frac{u^2 \tan \phi}{r} = -\frac{1}{\rho} \frac{\partial p}{\partial y} \quad (3.6)$$

Except for Earth, applying equation (3.6) is not always possible, since it is difficult to measure pressure remotely. On the contrary, Venus temperature structure is routinely measured, thus, equation (3.6) needs to be re-written in a form that directly relates the zonal wind speed $u(z)$ to the vertical temperature structure $T(y)$.

If we define the geopotential as: $\Phi = gz$ (z is height, g is the acceleration of gravity) and assume hydrostatic approximation:

$$\frac{\partial p}{\partial z} = -g\rho$$

Equation (3.6) can then be written as:

$$\frac{u^2 \tan \phi}{a} = -\frac{1}{\rho} \frac{\partial p}{\partial y} = \frac{1}{\rho} \frac{\partial p}{\partial z} \frac{\partial z}{\partial y} = -g \frac{\partial z}{\partial y} = -\frac{\partial \Phi}{\partial y} = -\frac{1}{a} \frac{\partial \Phi}{\partial \phi} \quad (3.7)$$

In terms of the logarithmic pressure coordinate $\xi = -\ln \frac{p}{p_{ref}}$, where p_{ref} is the pressure at the reference level, the hydrostatic equation (3.7) reduces to:

$$\frac{\partial p}{\partial \Phi} = \frac{1}{g} \frac{\partial p}{\partial z} = -\rho$$

Using the perfect gas law $p = \rho RT$, where $R = 191.4 \text{ J kg}^{-1} \text{ K}^{-1}$ is the gas constant of the Venus atmosphere, we can then write:

$$p \frac{\partial \Phi}{\partial p} = -\frac{p}{\rho} = -RT = -\frac{\partial \Phi}{\partial \xi}$$

$$\frac{\partial \Phi}{\partial \xi} = RT \quad (3.8)$$

By differentiating (3.7) with respect to ξ and substituting (3.8), we obtain:

$$2u \frac{\partial u}{\partial \xi} = -\frac{1}{\tan \phi} \frac{\partial \Phi}{\partial \xi \partial \phi} = -\frac{R}{\tan \phi} \frac{\partial T}{\partial \phi} \Big|_{p=\text{const}} \quad (3.9)$$

Equation (3.9) is the *thermal wind equation* for cyclostrophic balance. Compared with the geostrophic balance, this is a non-linear equation in u . We can observe from equation (3.9) that generally an increase (decrease) of T towards the pole produces a decrease (increase) of u with height. It should be pointed out that at the equator and at the pole the cyclostrophic approximation ceases to be valid, since the term $\tan \phi$ in equation (3.9) goes to zero at the equator and to infinite at the pole; therefore, other forces in the original Navier-Stokes equation become dominant. Equation (3.9) can then be integrated using a basic trapezoidal differencing formula to infer zonal wind speeds directly from temperature retrievals:

$$u_{n+1}^2 = u_n^2 - \frac{R\Delta\xi}{2 \tan \phi} \left(\frac{\partial T}{\partial \phi_{n+1}} + \frac{\partial T}{\partial \phi_n} \right) \quad (3.10)$$

To resolve equation (3.10) a lower boundary condition u_0 must be fixed at the reference level and the latitudinal temperature gradient $\frac{\partial T}{\partial \phi_n}$ must be evaluated at each pressure levels.

If the vertical pressure profiles $p(y)$ can be measured, then an alternative method to calculate the zonal wind speed is to use the equation:

$$u^2 = -\frac{g}{\tan \phi} \left(\frac{\partial z}{\partial \phi} \right)_p \quad (3.11)$$

derived from (3.7). Equation (3.11) has been used by Limaye (1985) to derive the zonal wind directly from meridional slope of the pressure surfaces and it has the advantage not to require a lower boundary velocity and to avoid integration.

In the next chapter the retrieval method used to derive wind speeds from VIRTIS and VeRa temperature profiles applying the cyclostrophic balance is discussed more in detail. The infrared imaging spectrometer VIRTIS and the radio science experiment VeRa provide both vertical temperature profiles; however, vertical pressure profiles can be inferred only from the radio science experiment.

4 Thermal zonal wind retrieval

The main goal of this work was to derive thermal zonal winds using the cyclostrophic approximation from temperature fields retrieved from VIRTIS and VeRa temperature soundings. VIRTIS sounds the night side of Venus Southern hemisphere in the altitude range 65 – 90 km with a very good spatial and temporal coverage (Grassi et al., 2008). VeRa observes both north and south hemispheres between 40 – 90 km of altitude with a vertical resolution of ~ 500 m; observations cover the day and night sides (Tellmann et al., 2009). VeRa is acquiring also vertical pressure profiles, that allows to derive the zonal thermal winds using a special form of the cyclostrophic approximation (Eq. 3.11) which does not need a lower boundary velocity (Section 3.1.2). This procedure can be used to check the sensitivity of the derived wind on the lower boundary condition and to test the retrieval method. A more detailed description of the experiments VIRTIS and VeRa can be found in chapter 2. In this section the method used to retrieve zonal winds, their uncertainties, sensitivity on the lower boundary condition, and results are described in detail.

4.1 Wind retrievals from VIRTIS temperature soundings

4.1.1 Retrieval method

VIRTIS temperature profiles were used to derive the zonal wind velocity assuming cyclostrophic balance (Eq. 3.9). Figure 4.1 shows examples of latitude dependence of temperatures at constant pressure levels. Latitudinal temperature fields have been described in detail in chapter 2. The fitting curves used to evaluate the latitudinal temperature gradient are also shown in this figure. In order to determine the fitting curves, the retrieved air temperatures $T(\phi)$ were first binned to a latitudinal grid of 1° and then smoothed over 10° latitude intervals.

The most important structures of Venus temperature field can be observed in figure 4.1: the cold collar is clearly visible between 50°S and 70°S latitude at 40 and 90 mbar; above 75 km of altitude (~ 20 mbar) the warm polar mesosphere is also present. Both positive temperature gradient in the high mesosphere and cold collar right at the cloud tops were observed by the Pioneer Venus (Taylor et al., 1983; Newman et al., 1984) and Venera - 15 (Zasova et al., 2007) missions in the Northern hemisphere. VIRTIS observations in the south strongly suggest global hemispheric symmetry of the temperature field, in good agreement with previous observations from Venera-15 (Zasova et al., 2007). The lower boundary condition needed to solve differential equation (3.10) was taken at the reference pressure level $p_{\text{ref}} = 275$ mbar (~ 58 km) using the equation adopted by Counselman et al.

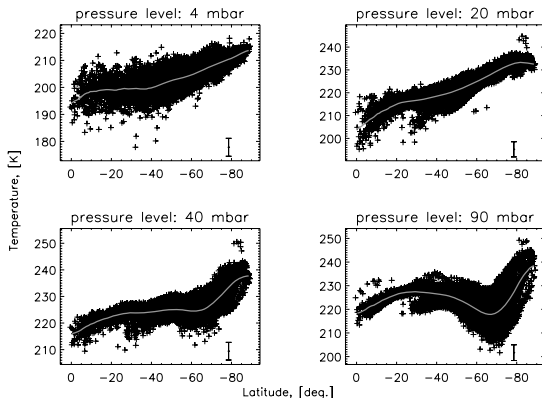


Figure 4.1: Plots of temperature at different pressure levels. Fitting curves are also shown (solid line). Error bar shows random error of air temperature retrieval. Data used for this and next figures of section 4.1 refer to five VIRTIS-M orbits observed during June and July 2006.

(1980); coefficients were selected to fit the Venus Monitoring Camera (VMC) direct measurements of wind profile and were provided by I. Khatuntsev (personal communications, 2008):

$$u_0(\phi) = \left[45 \cdot \operatorname{sech}\left(\frac{\phi - 56}{9}\right) + 75 \right] \cos \phi \quad (4.1)$$

In order to test our retrieval code we used temperature field retrieved from Venera - 15 Fourier Spectrometer (FS) data (Zasova and Khatuntsev, 1997). Our test calculations were in good agreement with original results (Fig. 4.2). Discrepancies are mainly due to the choice of the approximating curve.

4.1.2 Thermal winds

Thermal zonal winds were retrieved from VIRTIS temperature field applying the cyclostrophic balance. Figure 4.3(b) shows an example of thermal wind derived from a combination of five VIRTIS-M orbits. The main feature in the plot is the midlatitude jet centered at about 50° latitude and 67 km of altitude with a maximum speed of 90 m s^{-1} . The vertical wind shear $du/d\xi$ was also calculated (Fig. 4.4). Comparison of the wind field (Fig. 4.3(b)) with the temperature field (Fig. 4.3(a)) shows that the midlatitude jet is related to the cold collar. The negative latitudinal temperature gradient at $\sim 55 - 70^\circ$ latitude at cloud tops causes the positive vertical wind shear and wind acceleration in the lower part of the jet (Fig. 4.4). The thermal feature known as the warm polar mesosphere, characterised by an increase of temperature toward the pole on isobaric surfaces between 75 – 90 km of altitude, forces the thermal wind to decrease to zero very fast at high latitudes and it is responsible for the negative vertical wind shear observed in figure 4.4. It

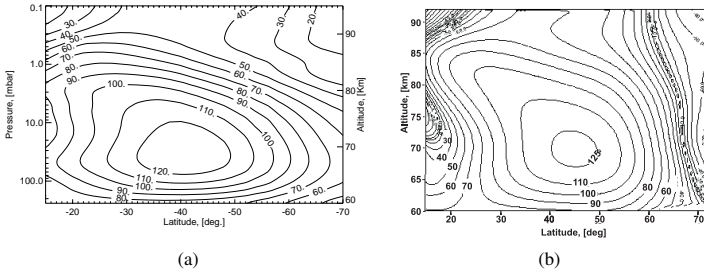


Figure 4.2: (a) Zonal thermal wind field derived from Venera 15 data applying the retrieval method used in this thesis. (b) Zonal thermal wind field derived from Venera 15 data using the retrieval method described in Zasova et al. (2000). Data were provided by I. Khatuntsev (personal communication, 2009).

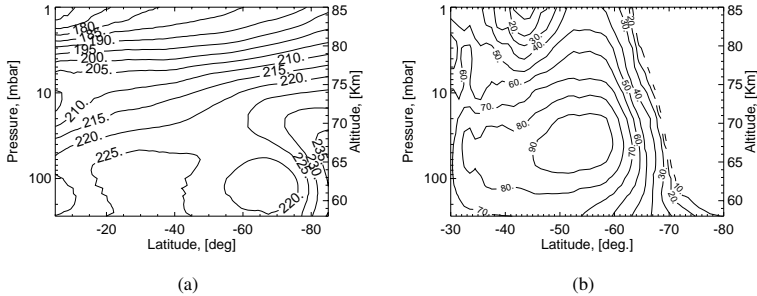


Figure 4.3: (a) Meridional cross section of temperature (K). Contour interval is 10 K. (b) Latitude-height cross section of zonal thermal wind speed (m s^{-1}) derived from VIRTIS temperature profiles assuming cyclostrophic balance. Contour interval is 10 m/s .

is important to note, however, that for latitudes lower than 30° and higher than 75° the cyclostrophic balance fails: as will be further discussed in section 4.2.1, this means that the necessary condition for validity of cyclostrophic balance fails and other forces in the Navier-Stokes equation (3.1) must be taken in account. Thus, wind retrievals at these latitudes should not be taken in account. Layers of high positive vertical wind shear between $\sim 58 - 68$ km of altitude and layers of negative wind shear above ~ 70 km of altitude are in good agreement with previous observations (Fig. 4.4; Schubert et al., 1980; Newman et al., 1984; Kerzhanovich et al., 1987). The VIRTIS observations completely covered the night side of the Southern hemisphere that allowed us to estimate the dependence of temperature field on local time. Figure 2.8 shows Latitude-height cross sections of tem-

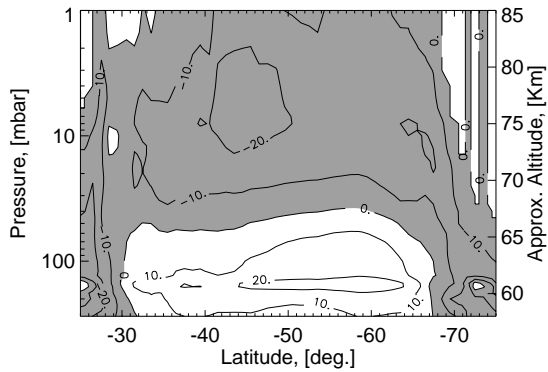


Figure 4.4: Contours of vertical wind shear $du/d\xi$ (m s^{-1}). Negative shear regions are represented in gray. Contour interval is 10 m s^{-1} .

perature for 3-hour local time bins. Changes in temperature structure with local time also affect the thermal wind field. An example of the effect of diurnal variations of temperature structure is shown in figure 4.5. Wind field has been retrieved for four different local time ranges combining the temperature profiles of five VIRTIS orbits acquired between May and December 2006. The velocity of the midlatitude jet tends to increase during the night reaching a maximum value at dawn of 110 m s^{-1} ; this behaviour is closely related to the temperature structure which cools during the night. It must be noticed that the VIRTIS temperature field depends also on the cloud structure postulated in retrievals; this can also affect the retrieval of thermal winds.

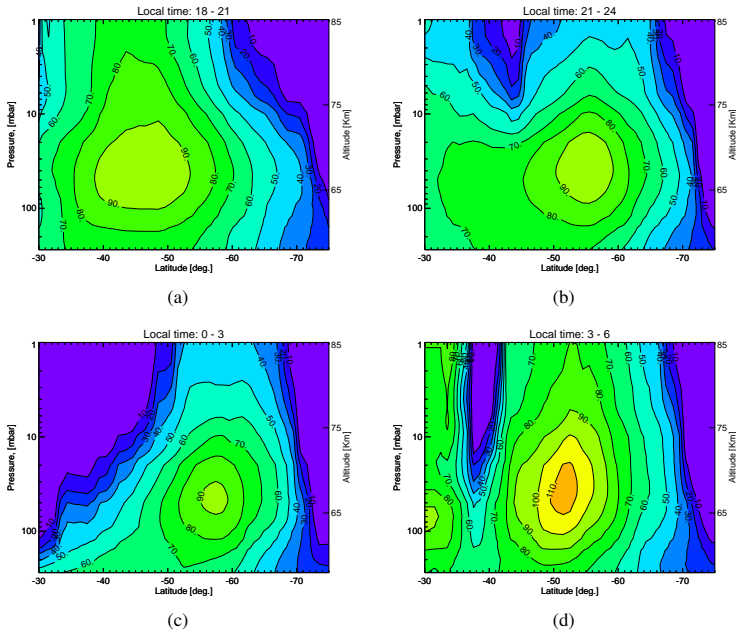


Figure 4.5: Latitude-height cross sections of zonal thermal wind (m s^{-1}). Data have been divided in four local time bins: (a) 18 – 21 LT; (b) 21 – 24 LT; (c) 00 – 03 LT; and (d) 03 – 06 LT. Contour interval is 10 m s^{-1} .

4.2 Wind retrievals from VeRa radio occultation data

4.2.1 Retrieval method

Equation (3.9) has been used to infer the zonal wind speeds directly from VeRa temperature retrievals. A detailed description of VeRa latitudinal temperature field can be found in section 2.2.2. In order to facilitate the evaluation of the latitudinal temperature gradient, the retrieved temperatures were first binned to a 5° latitudinal grid and then smoothed over 10° latitude intervals (Fig. 4.6). From equation (3.9) it is possible to observe that generally an increase (decrease) of temperature towards the pole corresponds to a decrease (increase) of zonal wind speed with height. Hence, we expect an increase of zonal wind in the altitude region 200 – 30 mbar enhanced by the negative latitudinal temperature gradient in the latitude range 30°S to 65°S and a deceleration of wind above ~ 20 mbar caused by the warm polar mesosphere. The reference pressure p_{ref} was fixed at 1700 mbar (~ 45 km altitude) and the velocity used as lower boundary condition is the cloud-tracked wind profile retrieved from VIRTIS/VEx $1.74 \mu\text{m}$ images corresponding to a nominal altitude of ~ 47 km (Sánchez-Lavega et al., 2008). The VeRa experiment provides also vertical pressure profiles, that allows to evaluate the latitudinal gradient of pressure. A negative pressure gradient is a necessary condition for validity of cyclostrophic balance. To display the latitudinal pressure gradient, altitude profiles of the ratio of atmospheric pressures at $0 - 30^\circ\text{S}$ and $75 - 90^\circ\text{S}$ latitudes are presented in figure 4.7. In order for the cyclostrophic balance to be valid, the latitudinal pressure gradient must be directed towards the pole (Eq. 3.6); therefore, low- to high-latitude ratios greater than unity indicate regions where the cyclostrophic approximation can be valid. The vertical pressure profiles observed by VeRa radio occultation suggest that cyclostrophic balance can be valid in the mesosphere up to ~ 80 km of altitude; this is in good agreement with previous observations by Pioneer-Venus radio occultations (Taylor et al., 1980; Clancy and Muhleman, 1991).

4.2.2 Thermal winds

Assuming cyclostrophic balance, thermal zonal wind was derived from VeRa temperature profiles in figure 4.6. Vertical wind shear $du/d\xi$ was also calculated (Fig. 4.8(b)). As can be seen in figure 4.8(a), the main feature of the wind field is a midlatitude jet with a maximum speed of $\sim 140 \text{ m s}^{-1}$ centered at an altitude of ~ 68 km and extending between 30° and 55°S latitude. The jet is directly driven from the negative latitudinal temperature gradient observed in the altitude range 50 – 65 km which produces a positive wind shear in the same altitude range (Fig. 4.8(b)). Above ~ 70 km of altitude, a positive latitudinal temperature gradient is responsible for the negative vertical wind shear which forces the wind to decrease to zero at high latitudes above the midlatitude jet. The positive wind shear layer reaches greater altitudes ($\sim 65 - 70$ km) at midlatitudes ($\sim 25^\circ - 60^\circ\text{S}$) compared to higher and lower latitudes. The zones of low and high vertical wind shear are in a reasonable good agreement with previous observations obtained from Pioneer Venus radio-occultation (Newman et al., 1984) and Pioneer Venus, Vega 1 and 2 descent probes (Schubert et al., 1980; Kerzhanovich et al., 1987).

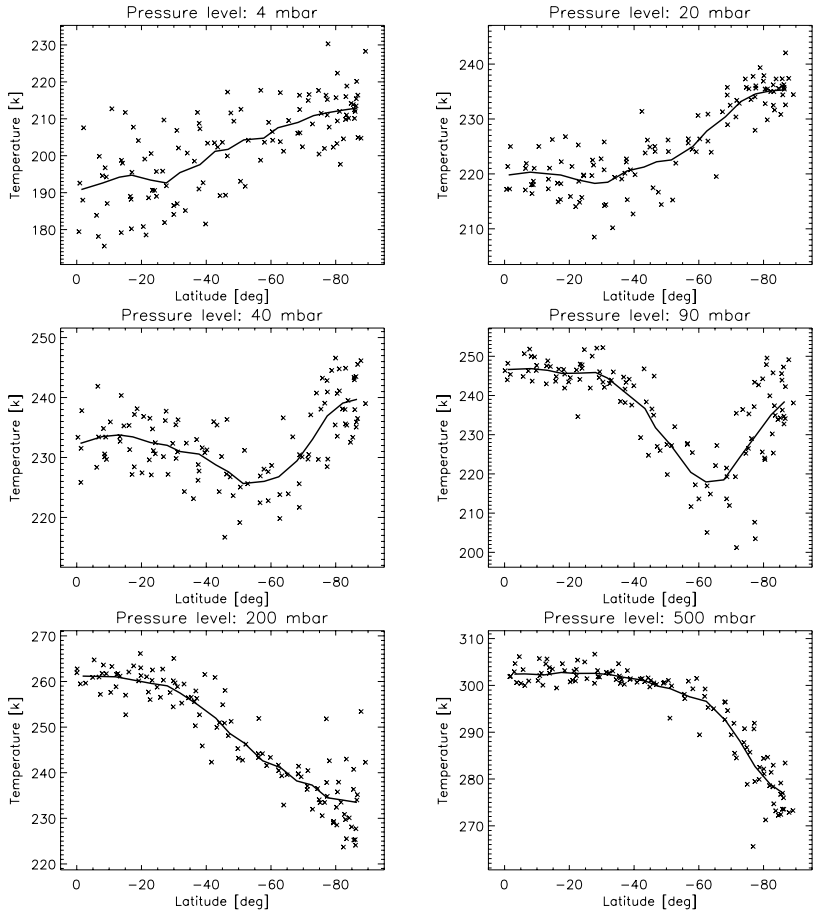


Figure 4.6: Latitude temperature profiles at different pressure levels. Fitting curves are also shown (solid lines). Data used for this and next figures refer to 116 VeRa profiles.

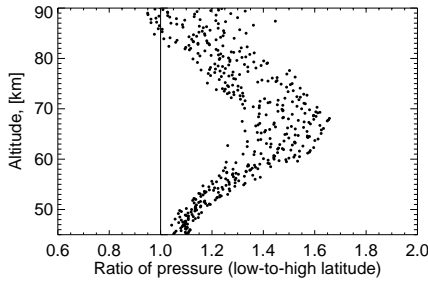


Figure 4.7: Latitudinal pressure gradient calculated as the ratio of atmospheric pressures at 0 – 30° and 75 – 90° latitude.

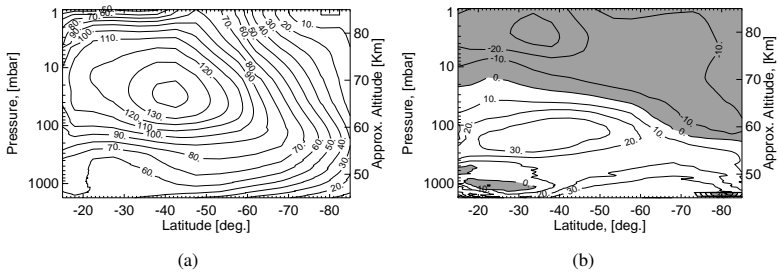


Figure 4.8: (a) Latitude-height cross section of zonal thermal wind speed (m s^{-1}) derived from VeRa temperature profiles assuming cyclostrophic balance. Contour interval is 10 m s^{-1} . (b) Contours of vertical wind shear $du/d\xi$ (m s^{-1}). Negative shear regions are represented in gray. Contour interval is 10 m s^{-1} .

4.2.3 Alternative retrieval method

Zonal wind velocities were retrieved from the meridional slope of the pressure surfaces using equation (3.11). The meridional gradient of the height of the pressure surfaces has been evaluated by binning height profiles to a 5° latitudinal grid and then by smoothing over 10° latitude intervals (Fig. 4.9). Pressure height profiles in figure 4.9 are in good agreement with previous radio occultation observations (Newman et al., 1984). Figure 4.10 shows the zonal wind field derived from the gradient of pressure height profiles. The main structure of the wind field is a midlatitude jet at the cloud top with a maximum speed of 140 m s^{-1} ; the jet extends from $\sim 50^\circ\text{S}$ to $\sim 20^\circ\text{S}$ latitude. Equation (3.11) does not require a lower boundary velocity, thus, it allows to test the sensitivity of the zonal wind derived from equation (3.9) (standard method) on the choice of the lower

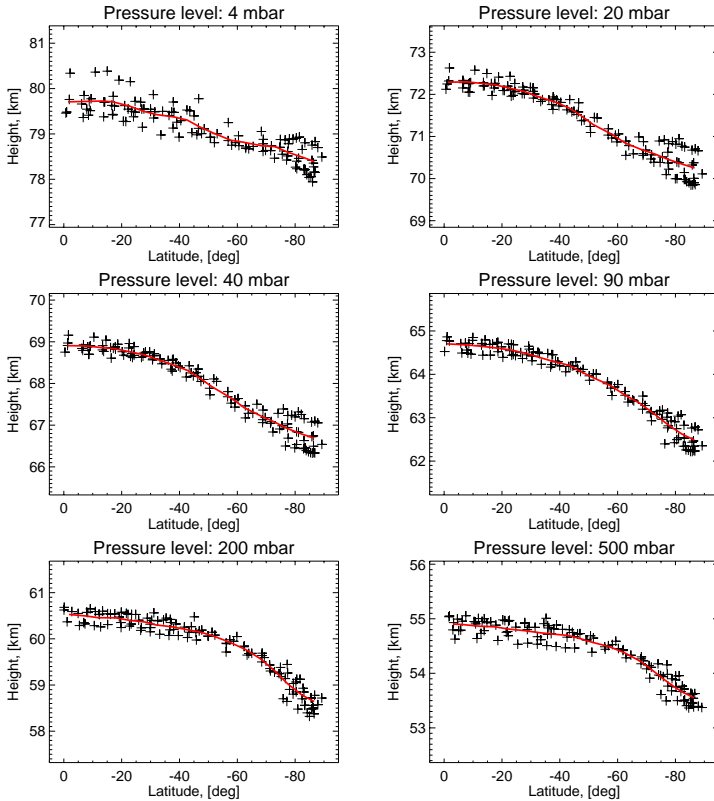


Figure 4.9: Plots of latitude height profiles at different pressure levels. Fitting curve are also shown (red line).

boundary condition. Comparison of the zonal wind fields obtained from equation (3.11) and (3.9) shows a good agreement, therefore, validating the standard retrieval method and confirming the independence of the retrieved zonal wind field on the lower boundary condition (Fig. 4.10; Fig. 4.8(a)).

4.3 Sensitivity to the lower boundary condition

I studied sensitivity of calculated thermal winds to lower boundary conditions by applying different functions as lower boundary condition. Figures 4.11 and 4.12 display

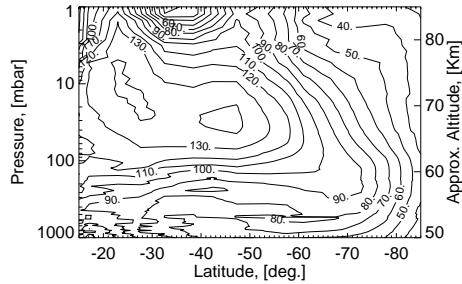


Figure 4.10: Latitude-height cross section of zonal thermal wind speed (m s^{-1}) derived from VeRa pressure height profiles assuming cyclostrophic balance. Contour interval is 10 m s^{-1} .

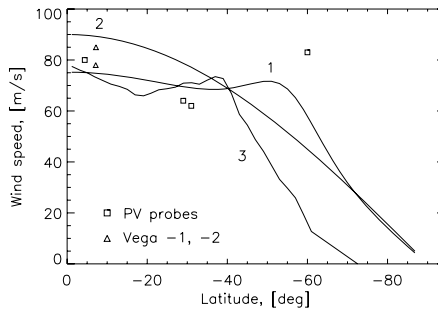


Figure 4.11: Functions used as lower boundary condition. Curve 1 is the function described by equation (4.1) used for the nominal case; curve 2 is the solid body rotation function $u_0 = 90 \cos \phi$; curve 3 represents the cloud-tracked wind derived from Galileo SSI NIR images (Peralta et al., 2007). Wind measurements obtained from Vega-1 and Vega-2 descent vehicles and Pioneer Venus landing probes are also shown for comparison.

respectively the curves used to test the sensitivity of VIRTIS and VeRa thermal winds. We calculated the difference between the zonal wind field derived from the temperature fields using the nominal curve as lower boundary condition and that obtained using the other curves. As can be seen in figures 4.13(a, b) and 4.14(a,b,c), the zonal thermal wind is only slightly dependent on the choice of the base wind. In figure 4.13(a) the difference reaches maximum value of 20 m s^{-1} due to the absence in curve 2 of the midlatitude bulge present in curve 1 that forces winds to slow down with altitude faster than in the nominal case. In figure 4.13(b) a bigger discrepancy is observed caused by the strong wind

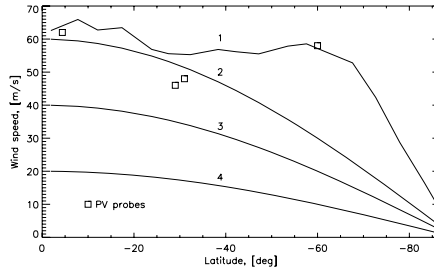


Figure 4.12: Velocities used as lower boundary condition. Curve 1 is the cloud-tracked wind derived from VIRTIS/VEx images (Sánchez-Lavega et al., 2008). Curve 2, 3 and 4 correspond to the solid body rotation functions $u_0 = u_0(\phi = 0) \cos \phi$ where $u_0(\phi = 0) = 20, 40, 60 \text{ m s}^{-1}$. Curve 1 is used for the nominal case. Winds derived from Pioneer Venus probes are also added.

decrease at midlatitudes seen in Galileo NIR images. In figure 4.14(a,b,c) a maximum difference of 30 m s^{-1} occurs for all cases at high latitudes due to the strong decrease of wind. In the region of the midlatitude jet ($\sim 42^\circ$ latitude) a maximum difference of 15 m s^{-1} can be seen. Both test cases show that lower boundary condition does not affect the region of the jet.

4.4 Uncertainties in wind speeds

Errors in the temperature retrievals are the source of uncertainty on the derived wind speed. We followed the approach used by Newman et al. (1984) to assess the propagation of temperature retrieval error on the wind field. The same method has been applied to zonal thermal winds derived from VIRTIS and VeRa temperature fields. Temperatures have been binned to 2° (5° in the case of VeRa) latitudinal grid and standard deviation has been calculated on each pressure level. An approximation curve was fitted through the standard deviations and added to the original fitting curve to produce the $+1\sigma$ curve. The -1σ and $\pm 2\sigma$ curves were calculated in a similar way. Figure 4.15(a,b) shows that almost all data points are within $\pm 2\sigma$ range. Since scattering of the retrieved temperatures depends on latitude, the gradients of $\pm 1\sigma$, $\pm 2\sigma$ curves differ from that of the original approximation curve, that results in distortions of the wind field. Wind speeds were retrieved from $\pm 1\sigma$, $\pm 2\sigma$ curves, using equation (3.9) and the nominal boundary condition to assess the error in wind velocity determination.

Uncertainties on VIRTIS wind field: For the curves $+1\sigma$, $+2\sigma$ the position of the jet is shifted to $\sim 42^\circ$; the jet of curves -1σ , -2σ can be observed at about $\sim 52^\circ$ (Fig. 4.16). The wind field calculated for 1σ and 2σ curves has respectively a midlatitude jet speed

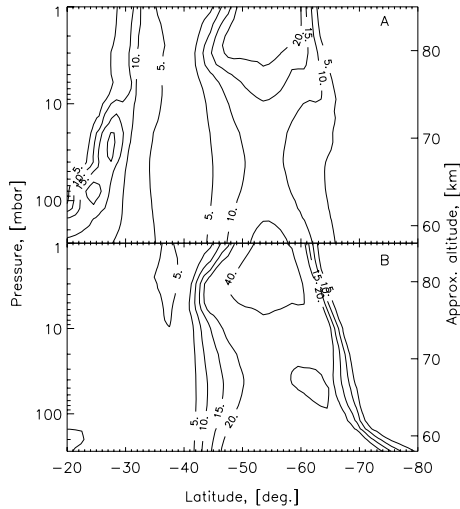


Figure 4.13: Contours of the difference absolute value (m s^{-1}) between the zonal thermal wind speed derived from VIRTIS temperature retrievals assuming $u_0(\phi) = [45 \cdot \text{sech}((\phi - 56)/9) + 75] \cos \phi$ as lower boundary condition and the zonal thermal wind derived assuming: (a) $u_0 = 90 \cos \phi$ and (b) cloud-tracked winds derived from Galileo SSI NIR images as lower boundary condition.

of $\sim 85 \text{ m s}^{-1}$ and $\sim 100 \text{ m s}^{-1}$. On the other hand for the -1σ and -2σ curves the speed of the jet reaches a value of $\sim 100 \text{ m s}^{-1}$ at $\sim 52^\circ$ respectively. Systematic error due to cloud structure assumption needs to be estimated.

Uncertainties on VeRa wind field: As can be observed in figure (4.17), for all cases, the position of the jet is not changed within 5° latitude. The wind speed retrieved from curve 1σ show a max jet velocity of 147 m s^{-1} at 42° latitude. Wind field obtained from curve -1σ has a jet speed of 141 m s^{-1} at 42° . Jets for curves $\pm 2\sigma$ present a speed of 150 m s^{-1} and 138 m s^{-1} at 42° respectively.

As an esteem of retrieval error on the midlatitude jet speed, it seems reasonable to take a value of $\pm 15 \text{ m s}^{-1}$ which is comparable to the uncertainties on cloud - tracked winds derived from the Venus Monitoring Camera (Moissl et al., 2009).

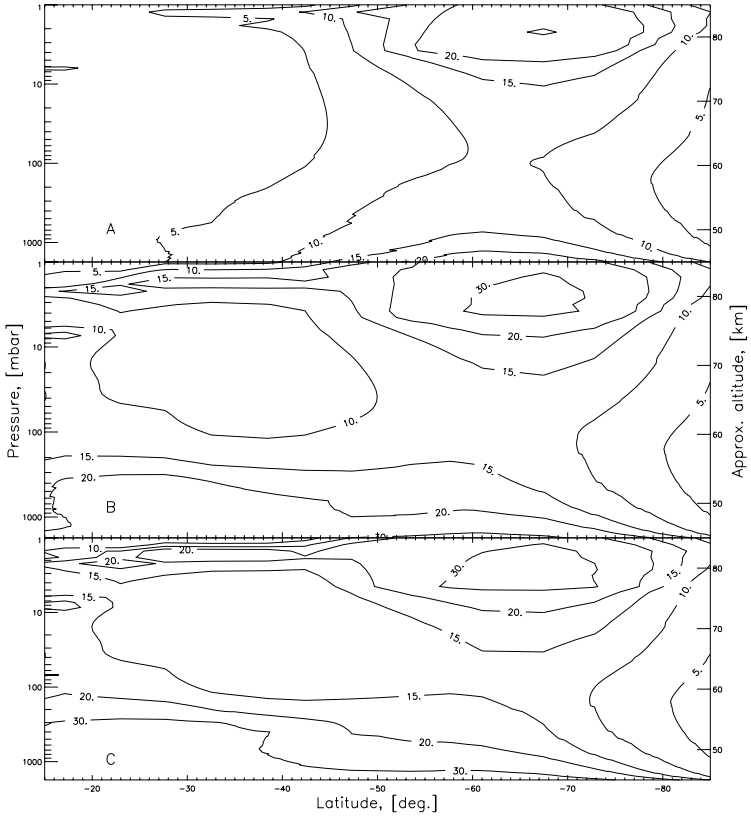


Figure 4.14: Contours of the difference absolute value (m s^{-1}) between the zonal wind field derived from VeRa temperature profiles using VIRTIS cloud-tracked wind as lower boundary condition and those obtained assuming (a) $u_0 = 60 \cos \phi$; (b) $u_0 = 40 \cos \phi$; (c) $u_0 = 20 \cos \phi$ as lower boundary conditions.

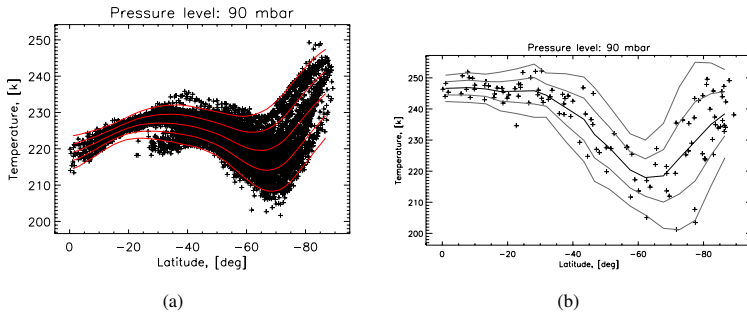


Figure 4.15: Latitude dependence of temperatures at a pressure level of 90 mbar. The fitting curve is also shown together with the $\pm 1\sigma$, $\pm 2\sigma$ curves. (a) VIRTIS temperature profile; (b) VeRa temperature profile.

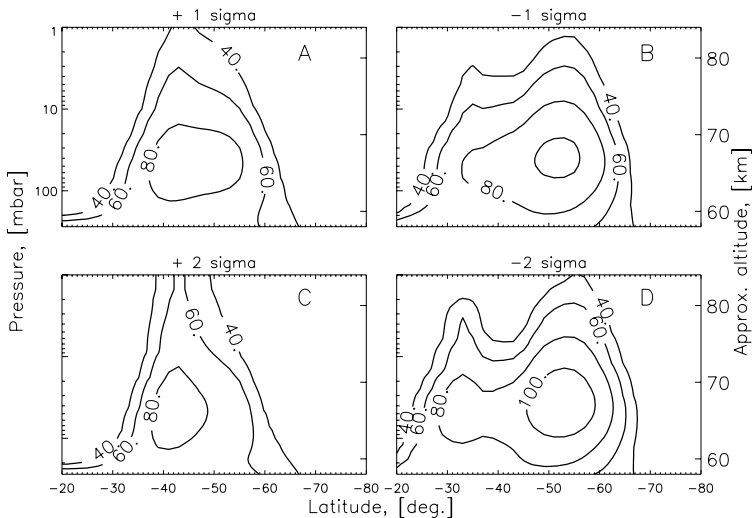


Figure 4.16: Contours of the zonal thermal wind speed (m s^{-1}) derived under the assumption of cyclostrophic balance from the curves: $\pm 1\sigma$; $\pm 2\sigma$. VIRTIS data were used. Contour interval is 20 m s^{-1} .

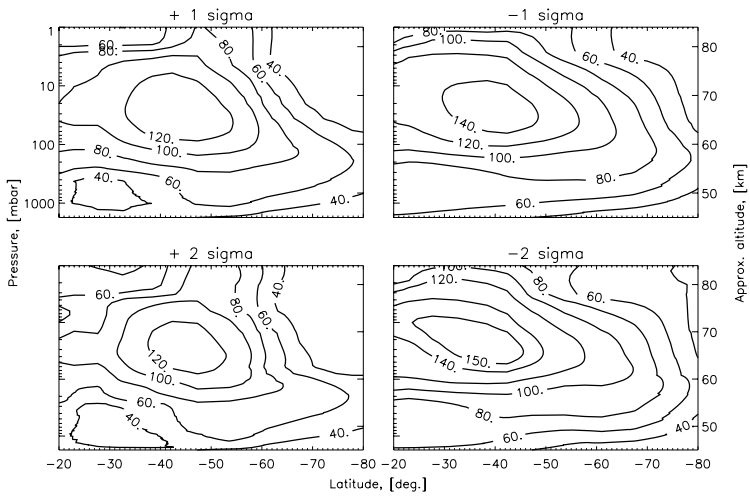


Figure 4.17: Latitude-height cross section of zonal thermal winds (m s^{-1}) derived from $\pm 1\sigma$ and $\pm 2\sigma$ curves applying cyclostrophic balance. VeRa data were used. Contour interval is $20 \text{ (m s}^{-1}\text{)}$.

5 Discussion

5.1 Zonal thermal winds from Venus Express observations

Cyclostrophic winds were calculated from the Venus Express temperature soundings. Temperature profiles were retrieved from two different experiments on board the Venus Express spacecraft: the mapping spectrometer VIRTIS-M and the radio science experiment VeRa. The retrieved velocity fields are presented in figures 4.3(b) and 4.8. Vertical wind shear $du/d\xi$ has also been calculated (Fig. 4.4; 4.8(b)). The main features of the wind field are:

1. A midlatitude jet occurring at the cloud tops ($\sim 68 - 70$ km altitude) with a wind speed up to ~ 140 m s⁻¹ extending between $35 - 60^\circ$ latitude.
2. Fast decrease of zonal winds poleward from 60° S with zero velocity reached at $\sim 70^\circ$ S.
3. Gradual decrease of thermal wind with altitude above the jet (Fig. 4.4; 4.8(b)).

These features correlate with the behaviour of the temperature field (Fig. 4.3(a)). According to the thermal wind equation (Eq. 3.9) the negative latitude gradient within the upper cloud (< 70 km) associated with the cold collar produces a positive wind shear and accelerates the wind in the same altitude range (Fig. 4.8(b); 4.4). This trend changes with reversal of the temperature gradient above the cloud that corresponds to a negative vertical wind shear which forces the wind to decrease to zero at high latitudes above the midlatitude jet. This deceleration is the strongest in high latitudes ($> 65^\circ$ S) that results in that cyclostrophic balance breaks down in polar mesosphere where other forces become significant such as eddies, turbulent motions, vertical viscosities (Fig. 4.3(b); 4.8). The positive wind shear layer reaches greater altitudes ($\sim 65 - 70$ km) at midlatitudes ($\sim 25^\circ - 60^\circ$ S) compared to higher and lower latitudes. The thermal wind field and the zones of low and high vertical wind shear are in a reasonable good agreement with previous observations obtained from Pioneer Venus radio-occultation (Newman et al., 1984; Limaye, 1985), Venera-15 (Zasova et al., 2007), Galileo-NIMS (Roos-Serote et al., 1995), and Pioneer Venus, Vega 1 and 2 descent probes (Schubert et al., 1980; Kerzhanovich et al., 1987).

Local time variability: The VIRTIS observations completely covered the night side of the Southern hemisphere that allowed us to estimate the dependence of temperature and

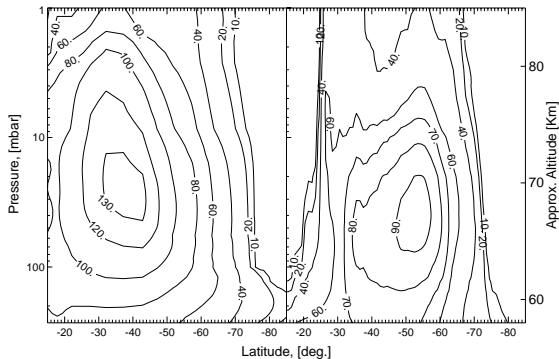


Figure 5.1: Meridional cross sections of zonal thermal winds derived from (left) VeRa and (right) VIRTIS temperature profiles applying cyclostrophic approximation. The lower boundary condition was fixed for both zonal wind at ~ 58 km of altitude (~ 275 mbar), the velocity used as lower boundary condition is the function $u_0 = (45 \cdot \text{sech}((\phi - 56)/9) + 75)$.

wind field on local time. Following the earlier studies, especially the one by Zasova et al. (2007), local time variability has been searched in the properties of the mid-latitude jet. The temperature field clearly indicates radiative cooling by ~ 15 K of the night side atmosphere at the cloud tops (Fig. 2.6) which also propagates to the thermal wind field (Fig. 4.5). However, conclusions on this basis must be taken cautiously. First, the coverage by VIRTIS temperature sounding that have been used so far is limited by the night side. And, second and probably more important, the weak meandering of the thermal wind field of $10 - 20 \text{ m s}^{-1}$ that results from diurnal variations of temperature structure seems to be within the "ignorance" range of the cyclostrophic hypothesis itself. For instance, the equation (3.9) was derived ignoring the meridional wind component which is of $\sim 15 \text{ m s}^{-1}$. So there could be some doubt that the wind field variations of $10 - 20 \text{ m s}^{-1}$, although derived by correct numerical procedures, are physically meaningful.

Comparison VIRTIS-VeRa wind retrievals: A comparison between the zonal wind field derived from VeRa temperature profiles and that obtained from VIRTIS temperature retrievals is shown in figure 5.1. For a better comparison the same lower boundary condition was chosen for both wind fields: it was fixed at ~ 58 km of altitude (~ 275 mbar) and the velocity used as lower boundary was $u_0 = (45 \cdot \text{sech}((\phi - 56)/9) + 75) \cos \phi$ (Piccialli et al., 2008). VIRTIS temperatures used to derive the wind are a combination of five orbits acquired between July 2006 and August 2008. The main feature observed in both figures is the midlatitude jet: the VeRa jet (Fig. 5.1, left) has a maximum speed of 130 m s^{-1} at the cloud top around $\sim 40^\circ\text{S}$ latitude, the VIRTIS wind field (Fig. 5.1, right) presents a jet with a maximum speed of 100 m s^{-1} centered around $\sim 50^\circ\text{S}$ latitude at 67 km of altitude.

Analysis shows that this discrepancy mainly results from peculiarities of temperature sounding techniques. VeRa radio-occultation data provide temperature structure with

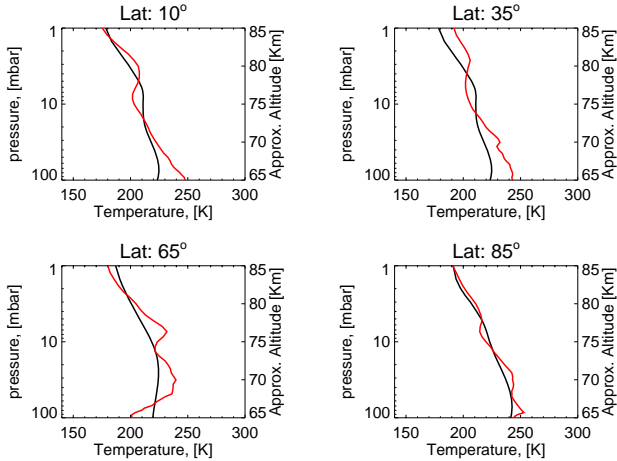


Figure 5.2: Vertical temperature profiles derived from VIRTIS (black) and VeRa (red) sounding at four different latitudes. VIRTIS and VeRa temperature have been selected in order to have approx. same local time.

vertical resolution of few hundred meters that allows the measurements to completely resolve deep temperature inversions typical for the cold collar regions. Vertical resolution in VIRTIS thermal emission spectroscopy in the $4.3 \mu\text{m}$ CO_2 bands does not exceed few kilometers. This smoothes temperature inversions and effectively reduces the latitudinal gradient of temperature that eventually accelerates the wind.

It is important to notice that VeRa temperature sounding is not sensitive to clouds; on the contrary, the cloud structure is assumed in VIRTIS temperature retrievals and uncertainty in the cloud model result in systematic temperature retrieval errors. Figure 5.2 shows the comparison between VIRTIS and VeRa vertical temperature profiles; VIRTIS temperatures near the equator at the cloud top ($\sim 65 - 70$ km altitude) are systematically ~ 30 K lower than VeRa temperatures. As a consequence, the negative latitudinal temperature gradient in the altitude range $50 - 65$ km which produces the midlatitude jet is less pronounced for VIRTIS than for VeRa, this in turn implies a lower VIRTIS jet speed compared to VeRa's.

The reason of the difference between VIRTIS and VeRa temperatures near the equator is still not clear. One possible explanation is that at low latitudes the emission angle of VIRTIS (angle between the spacecraft, the target point and the vector normal to the planet's surface) reaches often values higher than 60° , this implies that the instrument is sounding a thicker layer of atmosphere than at midlatitudes, therefore, VIRTIS temperature retrievals could be more affected by uncertainties on cloud properties at low latitudes than at midlatitudes.

VeRa sounds much deeper in the atmosphere than VIRTIS, reaching altitudes as low as $\sim 40 - 45$ km; however, a disadvantage of VeRa is that it takes ~ 1 month to build a

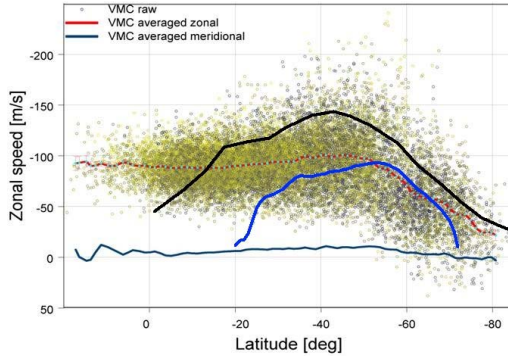


Figure 5.3: Comparison between the latitudinal profiles of cyclostrophic wind derived from VeRa (thick black curve) and VIRTIS (thick blue curve) temperature retrievals at an altitude of ~ 68 km (~ 36 mbar) and the VMC cloud-tracked wind. (Khatuntsev, personal communication)

meridional cross-section of temperature used for thermal wind calculation.

Earlier studies have shown a similar discrepancy: zonal winds derived from Venera-15 Fourier spectrometer temperature retrievals display a maximum jet speed of $90 - 100 \text{ m s}^{-1}$ (Zasova et al., 2000), while winds derived from Pioneer Venus radio occultation data present a maximum speed of $140 - 160 \text{ m s}^{-1}$ (Newman et al., 1984).

5.2 Comparison with cloud-tracked winds

Combination of temperature sounding and imaging measurements onboard Venus Express gives a unique chance to compare thermal wind field with cloud-tracked winds measured in the same temporal period; this allows validation of the cyclostrophic balance. Winds have been derived from the tracking of cloud features in the VMC and VIRTIS UV images at $\sim 66 - 70$ km altitude and in the VIRTIS near infrared images at altitudes of ~ 48 km and ~ 61 km (Sánchez-Lavega et al., 2008; Moissl et al., 2009). The zonal wind profile determined from VIRTIS data at 48 km altitude has been used as lower boundary condition to solve the thermal wind equation (Eq. 3.6) for VeRa temperature retrievals (Fig. 4.12). Cloud-tracked winds from VMC and VIRTIS images at 66 km and 61 km have been compared to thermal zonal winds derived from VIRTIS and VeRa temperature sounding at the same altitudes.

Figures 5.3 and 5.4 display the comparison between cloud-tracked winds derived from the VMC and VIRTIS images and thermal winds derived from VIRTIS and VeRa temperature retrievals. Zonal cyclostrophic winds derived from VIRTIS temperature sounding in first order agree with the Venus Express measurements of the cloud top winds (~ 66

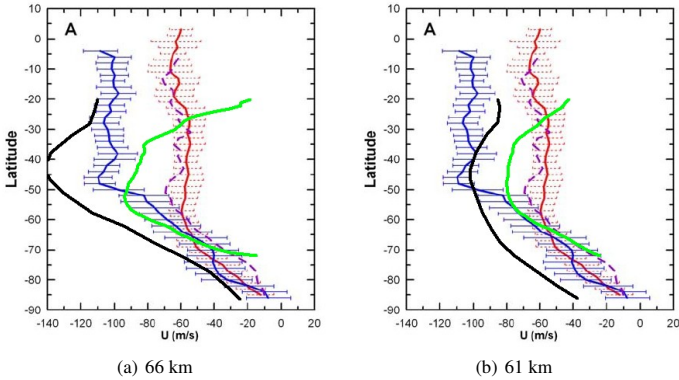


Figure 5.4: VIRTIS cloud-tracked winds observed at different altitudes: (blue) ~ 66 km; (violet) ~ 61 km; and (red) ~ 48 km. Zonal thermal winds derived from VIRTIS (green) and VeRa (black) vertical temperature profiles are shown for comparison (Sánchez-Lavega et al., 2008).

km altitude) that gave the wind speed of $80 - 100 \text{ m s}^{-1}$ at $\sim 50^\circ \text{ S}$ and fast decrease of zonal wind poleward (Fig. 5.3; 5.4(a)). However, our thermal wind deviates from the observed one in low latitudes ($< 20^\circ \text{ S}$) indicating that cyclostrophic balance is not valid here. The core of the cyclostrophic jet is located almost exactly at the cloud tops (~ 70 km) in all thermal wind calculations. Comparison between VIRTIS thermal winds and VIRTIS cloud-tracked winds at ~ 61 km altitude shows a good agreement at high latitudes, however, thermal winds present a stronger jet and a maximum difference of $\sim 20 \text{ m s}^{-1}$ is reached at $\sim 50^\circ \text{ S}$ latitude where VIRTIS midlatitude jet is observed. VeRa thermal winds display at all altitudes a strong midlatitude jet with a maximum speed of $\sim 150 \text{ m s}^{-1}$. However, in figure 5.3 the difference between cyclostrophic and cloud-tracked winds appears comparable to the scatter in cloud tracked winds. As reported by Limaye (2007), a disagreement between zonal thermal winds derived from the cyclostrophic assumption and cloud-tracked winds was observed in previous studies. Zonal thermal winds obtained from the direct application of cyclostrophic balance (Limaye, 1985) and from the thermal wind equation (Newman et al., 1984) applied to Pioneer Venus temperature retrievals displayed a similar zonal flow structure with a midlatitude jet speed up to $\sim 140 \text{ m s}^{-1}$. Venera 15 and Galileo NIMS observations produced similar results (Zasova et al., 2000; Roos-Serote et al., 1995). Cloud-tracked winds inferred from Pioneer Venus OCPP between 1979 and 1985 did not show any pronounced jet at all. It is important to notice, however, that the data used to derive the cyclostrophic winds was acquired in a period of time different from that in which cloud-tracked winds were measured. Therefore, one possible reason for their differences is that circulation on Venus is variable. On the contrary, Venus Express' observations used to derive cyclostrophic and cloud-tracking winds were acquired almost simultaneously. The reason of their disagreement is not yet understood, there could be several possibilities:

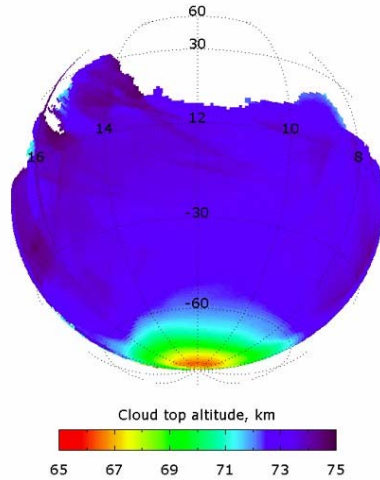


Figure 5.5: Mean cloud top altitude as function of latitude and local time (Ignatiev et al., 2009).

- **The midlatitude jet and the UV features used to measure the zonal flow could be at different altitudes:** uncertainty on the altitude of the UV absorber is one of main source of error on cloud-tracked winds. Ignatiev et al. (2009) has mapped recently the cloud top altitude and related it to the UV markings. In low and middle latitudes the cloud top is located at 74 ± 1 km. Its altitude decreases poleward from $\sim 50^\circ$ and reaches 63 – 69 km in the polar regions (Fig. 5.5). Due to the variation of cloud top altitude with latitude, the latitudinal wind profile derived from cloud-tracking might not refer to a constant altitude.
- **Limitation of the cyclostrophic approximation:** the cyclostrophic balance gives an approximate relationship between the pressure field and the zonal wind velocity. The approximation (Eq. 3.6) is applied to zonal flow only and neglects meridional velocity, which is $\sim 10 \text{ m s}^{-1}$, and eddies, turbulent motion and vertical viscosities which have been shown to play a major rule in the maintenance of the circulation.

5.2.1 Cloud top morphology

The Venus Monitoring Camera (VMC) is acquiring UV images of Venus at $0.365 \mu\text{m}$, the characteristic wavelength of the unknown ultraviolet absorber. The UV images display contrast features that are produced by inhomogeneous spatial and vertical distribution of the unknown absorber in the upper cloud. Morphology of the UV markings indicates variations of dynamic state at about 70 km altitude. Figure 5.6 shows VMC UV images taken at different latitudes. At low latitudes ($< 40^\circ\text{S}$) the mottled and patchy clouds indicate significant role of convection and turbulence near the subsolar point (Fig. 5.6(a); 5.6(b)). At $\sim 50^\circ\text{S}$ the outer edge of the bright midlatitude band marks a transition between the dark and turbulent low latitudes, where zonal wind is almost constant with latitude, and the bright and quiet midlatitude zone, where zonal wind quickly decreases towards the pole (Fig. 5.6(c); 5.6(d)). The studies of atmospheric chemical tracers, like carbon monoxide, suggest that this transition region could identify the poleward extent of the Hadley cell in the meridional circulation (Titov et al., 2008; Tsang et al., 2008). The VMC images (Fig. 5.6(c); 5.6(d)) give also a "visual" indication of the midlatitude jet at the edge of the bright midlatitude band. Figure 5.6(e) shows a close-up snapshot of the polar region dominated by a bright almost featureless band.

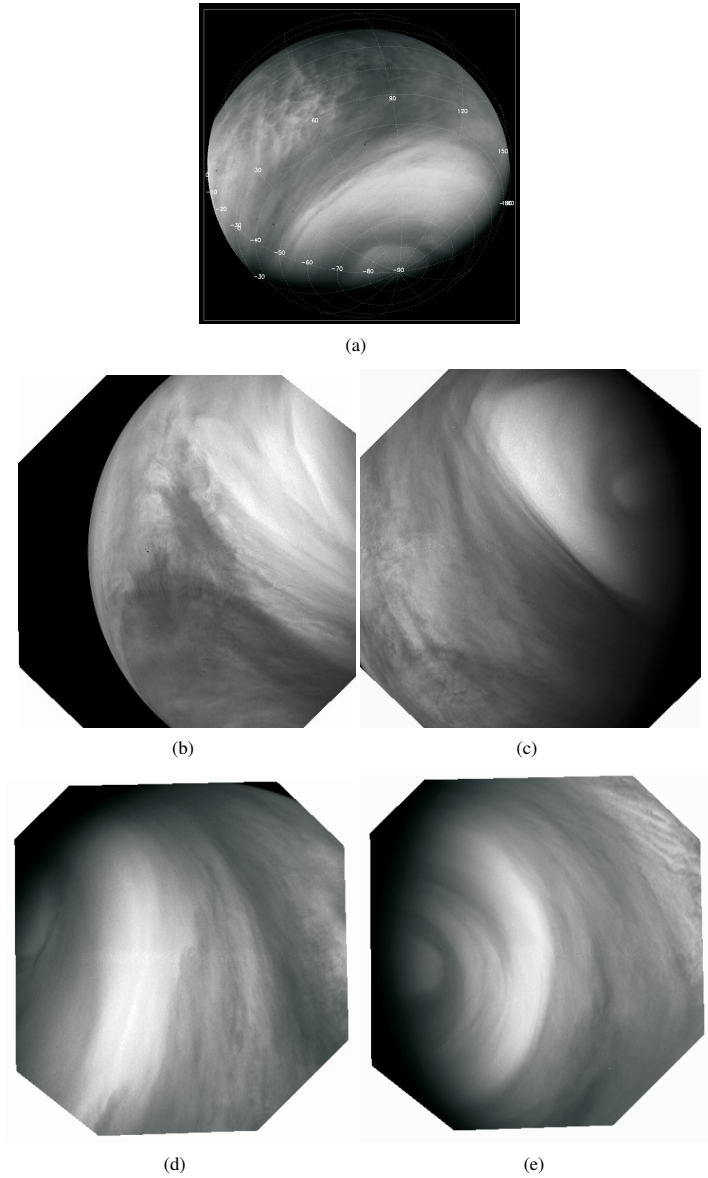


Figure 5.6: VMC UV images of Venus: global view (a), equatorial regions (b), transition zone and polar vortex (c, d, e).

5.3 Comparison with ground-based observations

Dynamics of the region above ~ 85 km is difficult to probe from spacecraft, in the absence of cloud tracers. It is expected to be a transition region between the zonal super-rotation in the lower atmosphere and the solar-antisolar regime which prevails in the thermosphere. Ground-based observations of Doppler shifts of molecular spectral lines allow to sound this region (Section 3.1.1.2). However, they have limited spatial and temporal resolutions, and often do not allow to separate the super-rotation and the solar-antisolar components (Lellouch and Witasse, 2008).

From 23 May 2007 to 9 June a world-wide coordinated Earth-based Venus observational campaign was carried out in support of the Venus Express mission. Different techniques of ground-based observations have been used to sound the altitude range from the cloud top to ~ 110 km. Comparison between zonal thermal winds and ground-based measurements is difficult, since different altitudes are probed and a different vertical and horizontal resolution is used. However, comparing the results obtained from different techniques can help to better constrain the mesosphere's circulation. Figure 5.7 shows a comparison between zonal thermal winds and ground-based measurements. The winds inferred by Rengel et al. (2008) and Clancy et al. (2008) refer to the combined retrograde zonal and subsolar-to-antisolar circulations winds. Rengel et al. (2008) sounds the altitude range 85 – 110 km, right above VeRa sounded region, integrating over the Venus' disc. Clancy et al. (2008) sounds the altitude centered at about the 0.01 mbar pressure level (103 ± 5 km) over the latitude range $30^\circ\text{N} - 30^\circ\text{S}$. Sornig et al. (2008) retrieves zonal wind at ~ 110 km of altitude, at different latitudes. Zonal wind velocities retrieved by Sornig et al. (2008) range from 3 ± 7 m s⁻¹ at the equator to the maximum of 32 ± 4 m s⁻¹ at midlatitudes (45°S), decreasing at higher altitudes in good agreement with zonal thermal wind. Wind speeds inferred by Clancy et al. (2008) and Rengel et al. (2008) show much higher values, mainly due to the combination of the zonal super-rotation and solar-antisolar circulation. Ground-based measurements indicate that the transition region is characterised by strong and variable winds.

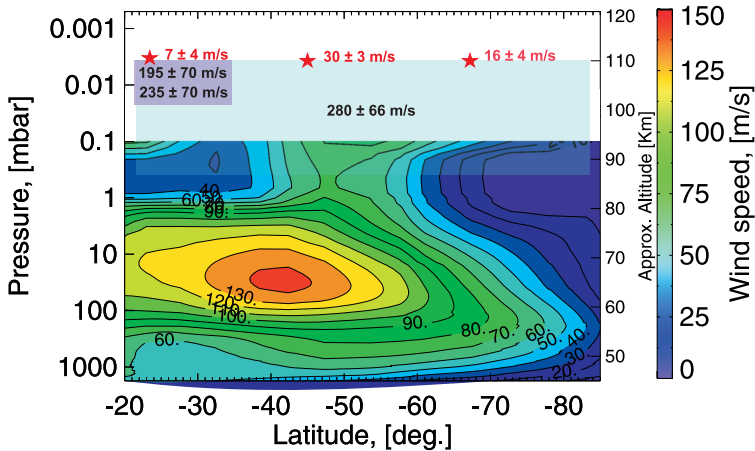


Figure 5.7: Zonal thermal wind (m s^{-1}) derived from VeRA temperature profiles compared to ground-based observations. *Light blue rectangle*: Rengel et al. (2008); *red star*: Sornig et al. (2008); *purple rectangle*: Clancy et al. (2008). Rectangles show the approximate vertical and latitudinal coverage of the ground based measurements. Winds inferred by Rengel et al. (2008) and Clancy et al. (2008) are a combination of the super-rotation and the subsolar-to-antisolar components.

5.4 Dynamical properties

The retrograde super-rotation, which dominates in the lower atmosphere of Venus that rotates about 50 times faster than the planet itself, has been known for over three decades. Yet, the basic processes responsible for maintaining the zonal super-rotation in the lower atmosphere and its transition to the solar-antisolar circulation in the upper atmosphere are still poorly understood Schubert et al. (2007). Many numerical models based on Earth-like general circulation models (GCMs) have been developed using realistic formulations of the Venus atmosphere but all attempts to model the zonal super-rotation have had only a partial success so far, indicating that the basic mechanisms of this phenomenon are still unclear. There are mainly two mechanisms which have been proposed to maintain the zonal super-rotation (Lebonnois et al., 2010):

- The first one is called the *Gierasch-Rossow-Williams mechanism* (Gierasch, 1975; Rossow and Williams, 1979). The angular momentum of the planet solid body is transported upward and poleward by the meridional circulation which consists of a thermally direct single Hadley cell upwelling at the equator, flowing poleward at the cloud top, and descending at high latitudes (Schubert et al., 2007). The angular momentum is then redistributed back to the equator through waves, produced at the equatorward side of the midlatitude jet by barotropic instabilities.
- The second hypothesis takes in account the possible role of the diurnal motion of the

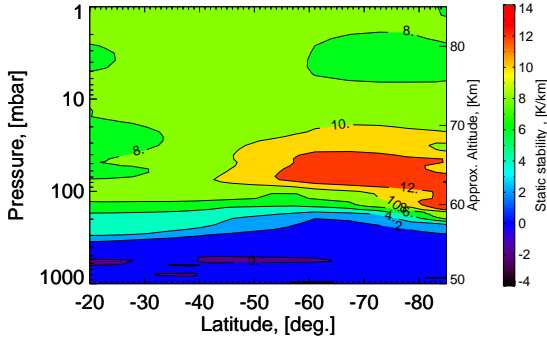


Figure 5.8: Contour plot of static stability $dT/dz - \Gamma$, (K/km) obtained from 116 VeRa profiles.

Sun, which can act on the total budget of angular momentum through two different mechanisms. One mechanism was proposed by Newman and Leovy (1992); the main idea is that the relative motion between the rotating atmosphere and the pattern of solar heating generates diurnal and semidiurnal thermal tides within and above the cloud layers. The combination of thermal tides, propagating vertically away from the cloud tops, and the meridional circulation has the net effect to transport angular momentum at lower latitudes and to accelerate the mean zonal flow at the equator. A second possibility is the *moving flame mechanism*: vertical eddies are induced by absorption of sunlight near the surface and within the upper cloud deck and are tilted by the eastward motion of the Sun so as to transport westward angular momentum upward (Schubert, 1983).

Within this section some of the properties that characterise the structure and dynamics of the Venus atmosphere are investigated in detail. The stability of the mesosphere between 50 – 85 km altitude is analysed by deriving the Richardson number Ri , a parameter used to predict formation of turbulence. We examined the possible presence of a transport barrier associated to the midlatitude jet by deriving the Ertel potential vorticity. Finally, conditions for barotropic instability to occur are analysed in detail.

5.4.1 Stability studies

Static stability: static stability is the ability of a fluid at rest to become turbulent or laminar due to the effects of buoyancy. The static stability is quantified as the difference between the measured temperature gradient dT/dz and its dry adiabatic lapse rate Γ :

$$\gamma = \frac{dT}{dz} - \Gamma \quad (5.1)$$

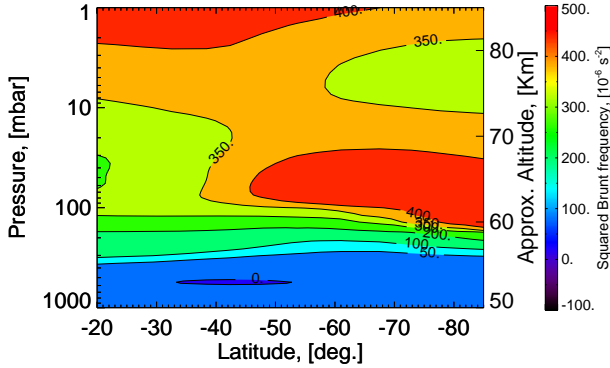


Figure 5.9: Meridional cross section of the squared Brunt-Väisälä frequency (10^{-6} s^{-2}). Data refers to 116 VeRa profiles.

where z is the geometric height of the atmosphere above the mean radius. The value of Γ in equation (5.1), has been derived for a real gas. A more detailed description of the method used to calculate Γ can be found in appendix A. Figure 5.8 displays meridional cross section of the static stability. High values of static stability indicate a stable stratified atmosphere, while negative values represent an atmosphere that is unstable against convective overturning. The adiabatic lapse rate can be considered as the temperature gradient established by convection. The static stability field showed in figure 5.8 is in good agreement with the vertical profiles of static stability from Tellmann et al. (2009). Right below the tropopause ($\sim 55 \text{ km}$ altitude) in the main cloud deck a region of low static stability is observed, indicating an atmosphere close to adiabatic. Above 60 km altitude poleward of 50° latitude a region of strong static stability can be seen which corresponds to the cold collar with strong temperature inversion.

Brunt-Väisälä frequency: The Brunt-Väisälä frequency N is the frequency at which an air parcel will oscillate when displaced vertically within statically stable environment. From equation (5.1) it is possible to define the Brunt-Väisälä frequency as:

$$N^2 = \frac{g}{T} \left[\left(\frac{dT}{dz} \right) - \Gamma \right] \quad (5.2)$$

It gives information on the static stability of the environment. If $N^2 > 0$ the air parcel will oscillate about its initial level. In the case $N = 0$ no accelerating force will exist and the parcel will be in neutral equilibrium at its new level. However, if $N^2 < 0$ the displacement will increase exponentially in time (Holton, 2004). The static stability criteria for dry air

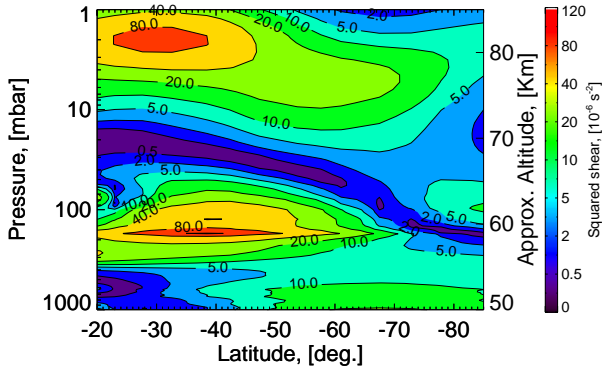


Figure 5.10: Contour plot of the squared wind shear (10^{-6} s^{-2}). Data refers to VeRa profiles.

can be summarised as follow:

$$N^2 > 0 \quad \text{Statically stable}$$

$$N^2 = 0 \quad \text{Statically neutral}$$

$$N^2 < 0 \quad \text{Statically unstable}$$

Figure 5.9 displays contour plot of the Brunt-Väisälä frequency. Temperature profiles derived from VeRa have been used, data were smoothed with a 1.5 km boxcar averaged before taking derivatives. The Brunt-Väisälä frequency is close to adiabatic over the altitude range of the middle cloud, between 50 – 57 km altitude, where N^2 is low, and shows variability with latitude. The stability contour plots (Fig. 5.8; 5.9) exhibits convective regions ($N^2 < 0$) only in very shallow layers within the middle cloud deck. In the upper cloud, above ~ 60 km altitude, a rapid transition to strong stability is observed. This transition level has been defined as the tropopause (Seiff, 1983). The high stability region clearly visible at latitudes $> 50^\circ$ at the cloud top corresponds to the location of the bright midlatitude band, seen in VMC images (Fig. 5.6), and correlates with the cold collar (Titov et al., 2008).

Richardson number: The Richardson number can be evaluated from the ratio of the stability and the shear (Gierasch et al., 1997):

$$Ri = \frac{N^2}{S^2} \quad (5.3)$$

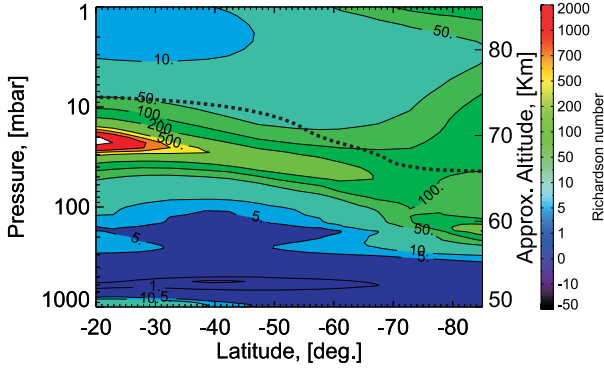


Figure 5.11: Latitude-height section of Richardson number calculated from VeRa data. Dot line follows the approximate altitude of cloud top.

Where S^2 is the squared shear and is define as:

$$S^2 = \left(\frac{\partial u}{\partial z} \right)^2 \quad (5.4)$$

where z is height and u is the westward zonal wind. Figure 5.10 shows meridional cross section of the squared wind shear derived from the thermal wind field in figure 4.8(a). Wind shear is discussed in section 4.2.2. The Richardson number is an important stability parameter and it is used to indicate dynamic stability¹ and the formation of turbulence: if the boundary layer is unstable (numerator of equation (5.3) is negative), then $Ri < 0$ and turbulence is sustained by convection. For stable conditions (numerator is positive) Ri will be greater than zero. The Glossary of Meteorology of the American Meteorology Society defines the critical Richardson number as "the values of the Richardson number below which air becomes dynamically unstable and turbulent. This value is usually taken as $Ri_c = 0.25$, although suggestions in the literature range from 0.2 to 1.0". More recent experimental, observational and theoretical results indicate that a single-valued critical Richardson number does not exist and that turbulence could survive also for $Ri \gg 1$ (Galperin et al., 2007). Figure 5.11 displays meridional cross section of the Richardson number. Note that the calculation of Ri requires the first derivative of a smoothed temperature and wind field; therefore, only gross features should be taken in account. The uncertainty in the Richardson number due to measurement uncertainties is hard to define quantitatively. An approach similar to that applied to determine uncertainty on zonal wind speed has been followed. An uncertainty of about $\sim 1 - 5$ has been found in the altitude range 50 – 60 km. It is possible to observe a layer where Ri has low values centered at ~ 54 km altitude. This nearly adiabatic middle cloud layer terminates near 60 km altitude, where Ri increases rapidly with altitude. A small positive value of Richardson number is a necessary condition for Kelvin-Helmholtz instability to occur (Schubert,

¹A measure of the ability of a fluid to resist or recover from infinitesimal perturbations of a steady state.

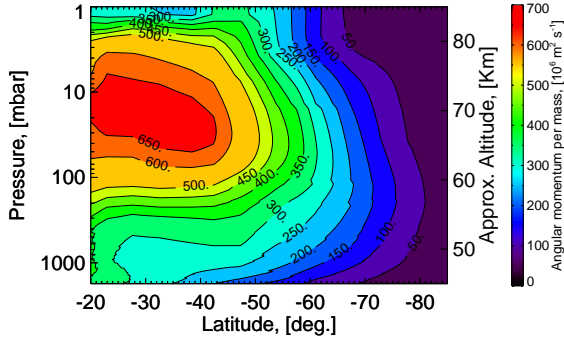


Figure 5.12: Zonal angular momentum per unit mass, calculated from VeRa zonal thermal winds in fig. 4.8.

1983). The Kelvin-Helmholtz instability results from velocity shears between two media. Recently, VMC and VIRTIS have detected at low-mid latitudes at the cloud top and within the cloud layer wave-like disturbance patterns that have been interpreted as gravity waves (Markiewicz et al., 2007; Peralta et al., 2008). A possible source of gravity waves is Kelvin-Helmholtz instability, even if convective processes generated in the stability layers between 48 – 55 km altitude are supposed to have a mayor role (Peralta et al., 2008). Between 60 – 70 km altitude Ri reaches very large values, this level corresponds to the jet core in the vertical profile of the derived thermal wind, where $\partial u / \partial z \rightarrow 0$, producing therefore a large Richardson number. Thus, this region is characterised by an high stability. A similar trend has been observed from Pioneer Venus radio occultation (Allison et al., 1994).

5.4.2 Angular momentum

From the calculated zonal mean winds it is possible to estimate the zonal mean angular momentum per unit mass:

$$M = (\Omega r \cos \phi + u)r \cos \phi \quad (5.5)$$

Where $\Omega = 2.99 \times 10^{-7} \text{ rad s}^{-1}$ is the rotation rate of Venus; $r = 6052 \text{ km}$ is the radius of the planet; ϕ is latitude; and u is the zonal velocity. Figure 5.12 displays the zonal angular momentum per unit mass derived from VeRa zonal wind field. Angular momentum reaches a maximum value at the cloud tops around $\sim 38^\circ$ corresponding to the region of the midlatitude jet (Fig. 4.8) and then decreases poleward with latitude. The excess of angular momentum at midlatitudes requires a mechanism of supply in order to sustain the midlatitude jet. Earlier studies have suggested that the midlatitude jet is maintained by the upper branch of the Hadley circulation which transport retrograde angular momentum

poleward. This hypothesis has been supported by analysis of Mariner 10 (Limaye and Suomi, 1981) and Pioneer Venus (Limaye et al., 1982) ultraviolet images.

5.4.3 Ertel potential vorticity

The use of atmospheric tracers can provide information on the dynamics of the atmosphere in regions where direct observations of the circulation are not possible. Atmospheric tracers generally can be divided in chemical and dynamical tracers. A chemical tracer is a minor atmospheric species with a lifetime longer than the transport process under study and a spatial variability. Dynamical tracer are properties of the flow which remain conserved following the motion under certain conditions. A commonly used dynamical tracer is potential vorticity, that is conserved for adiabatic frictionless flows (Holton, 2004). Potential vorticity can be considered a measure of the efficiency of baroclinic/barotropic instabilities in mixing horizontally the atmosphere (Schubert et al., 2007). Therefore, a strong horizontal gradient in potential vorticity indicates a weak horizontal mixing and corresponds to a mixing barrier.

Recent studies on Titan (Teanby et al., 2008) have made use of potential vorticity maps together with composition measurements to deduce the presence of a mixing barrier at high latitudes. A similar analysis can be done also for Venus. Studies of carbon monoxide (Tsang et al., 2008), an atmospheric chemical tracer, in the Venus atmosphere have shown an enhancement of CO from the equator to the pole with a peak at $\sim 60^\circ$ latitude at 35 km altitude. Poleward of 60°S CO decreases with latitude. Tsang et al. (2008) has suggested that the CO enrichment is caused by the descending branch of the Hadley cell which advects the trace gas from the cloud top, where it is produced, to the lower altitude of 35 km. The decrease of CO from 60° latitude to the pole could be an evidence, as on Titan, of the presence of a mixing barrier.

In order to investigate more in detail this possibility, we estimated the zonal mean of the Ertel potential vorticity from VeRa thermal zonal mean winds. Under the hydrostatic approximation, the general definition of Ertel potential vorticity (PV) becomes [The following is an excerpt from Read et al. (2006)]:

$$\begin{aligned} q &= \frac{(2\Omega + \nabla \times \mathbf{u}) \cdot \nabla \theta}{\rho} \\ &\simeq \frac{(f + \zeta_\theta) \partial \theta}{\rho \partial z} \\ &\simeq -g(f + \zeta_\theta) \frac{\partial \theta}{\partial p} \end{aligned} \quad (5.6)$$

where g is gravitational acceleration, \mathbf{u} is the velocity of the flow, $f = 2\Omega \sin \phi$ is the Coriolis parameter, Ω is the angular rotation rate of Venus, ϕ is latitude, θ is potential temperature, p is pressure, and ζ_θ is the vertical component of absolute vorticity calculated at constant potential temperature given by (Teanby et al., 2008):

$$\zeta_\theta = -\frac{1}{r^2 \cos \phi} \frac{\partial}{\partial \phi} (ru \cos \phi) \quad (5.7)$$

To evaluate ζ_θ , VeRa zonal thermal wind u has been used. Because Venus' atmosphere can be considered thin compared to the planet's radius, r can be assumed constant and

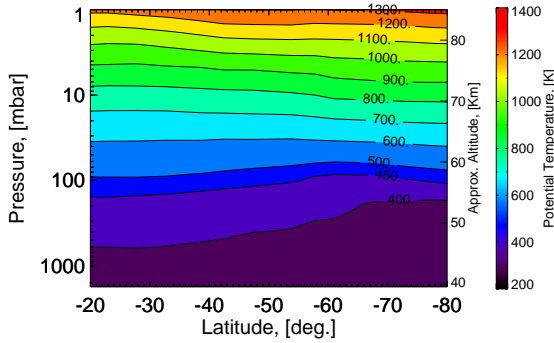


Figure 5.13: Potential temperature calculated from VeRa temperatures in fig. 2.14.

can be brought outside the differential term in equation (5.7). The potential temperature θ is the temperature which a parcel of dry air at pressure p and temperature T would have if it were expanded or compressed adiabatically to a standard pressure p_0 and it is defined by (Holton, 2004)

$$\theta = T \left(\frac{p_0}{p} \right)^\kappa$$

where p_0 is the reference pressure at 1700 mbar and κ is the ratio of heat capacities $(C_p - C_v)/C_p$. Values of C_p and C_v at different altitudes have been taken from the VIRA model (Seiff et al., 1985). Figure 5.13 shows the meridional cross section of potential temperature. The $1/p$ factor causes q to increase exponentially with altitude, making horizontal trends difficult to determine. Therefore, following Read et al. (2006), the potential vorticity has been normalised on potential temperature surfaces by $-g < \partial\theta/\partial p >$, where $\langle \rangle$ implies the horizontal mean value. Contour plot of scaled Ertel potential vorticity is displayed in figure 5.14. As can be observed in this figure, potential vorticity presents the same sign between 30 – 70° latitude and slightly increases from equator to pole. However, it does not show any region of strong latitudinal gradient, as should be expected in presence of a mixing barrier. Yet, this does not exclude completely the possible existence of a transport barrier. In a recent work, Beron-Vera et al. (2008) investigated transport barrier associated to the core of westward jets characterised by a small potential vorticity gradient. A new barrier mechanism, referred to as *strong KAM stability* is analysed; this mechanism predicts the existence of barriers at latitudes where $u'(\phi) = 0$, with $u' = du/d\phi$; u zonal wind, and ϕ latitude. Beron-Vera et al. (2008) used the strong KAM stability mechanism to explain observations of Jupiter's weather layer and Earth's subtropical stratosphere. The horizontal wind shear $u'(\phi)$ is plotted in figure 5.15; the condition $u'(\phi) = 0$ is satisfied in the core of the midlatitude jet. However, this argument alone can not be considered as an evidence of a transport barrier, more detailed investi-

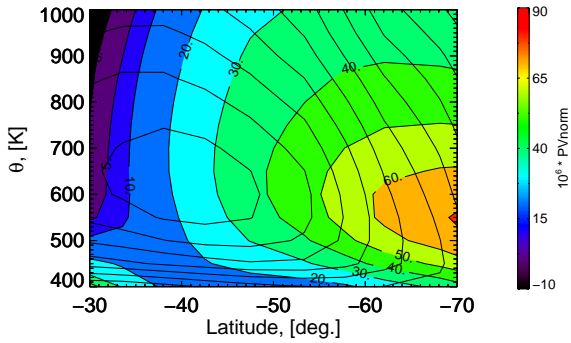


Figure 5.14: Contour plot of the Ertel potential vorticity (s^{-1}) of the zonal wind field of fig. 4.8. VeRa zonal wind field (m s^{-1}) has been overlotted for comparison.

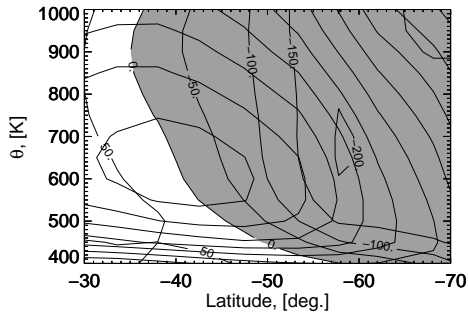


Figure 5.15: Contour plot of the horizontal wind shear $du/d\phi$ (m s^{-1}), where ϕ is latitude. Negative regions are represented in grey. VeRa zonal wind field (m s^{-1}) has been overlotted for comparison.

gation of chemical tracers is needed. For future studies, one possibility could be to use Venus Express observations of the atmospheric composition to investigate the possible presence of a mixing barrier. Venus Express uses two techniques to study the atmospheric composition. SPICAV/SOIR provides vertical profiles of atmospheric trace gases in the mesosphere (70 – 110 km altitude). VIRTIS investigates the composition of the low atmosphere (Titov et al., 2009).

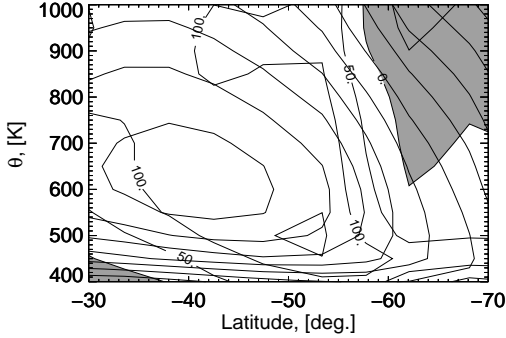


Figure 5.16: Contour plot of $\partial\zeta_a/\partial\phi$; units are 10^{-6} s^{-1} . Negative regions are represented in grey. VeRa zonal wind field (m s^{-1}) has been overlotted for comparison.

5.4.4 Barotropic instability

Origin of eddies in Venus atmosphere is an important question. Previous studies (Young et al., 1984; Michelangeli et al., 1987) have investigated the likely existence of barotropic or baroclinic instabilities near the midlatitude jet above the clouds. Here, we analysed in detail the conditions for barotropic instability to occur. Barotropic instability is a wave instability associated with horizontal shear in a zonal flow (Holton, 2004). The necessary condition for barotropic instability, known as *Rayleigh's criterion*, is that the latitudinal gradient of the absolute vorticity of the zonal flow changes its sign: $\partial\zeta_a/\partial\phi = 0$ (Houghton, 2002). This condition is equivalent to:

$$\frac{1}{r} \frac{\partial}{\partial\phi} \left(u \tan\phi - \frac{\partial u}{\partial\phi} \right) = 0 \quad (5.8)$$

somewhere on a constant potential temperature surface (Houghton, 2002). Figure 5.16 shows a contour plot of the gradient of absolute vorticity. Equation 5.8 is satisfied on the poleward side of the midlatitude jet. A similar result was obtained also by Newman et al. (1984) using Pioneer Venus radio occultation data. Different types of wave patterns have been observed in the VMC images at middle to high Northern latitudes between $40 - 70^\circ$ (Fig. 5.17) (Markiewicz et al., 2007). A combination of long waves and short wave trains was observed in the transition region between dark and bright cloud at $\sim 60^\circ\text{N}$ (Fig. 5.17(b)). Unusual long waves with small wavelength were detected at $\sim 45^\circ\text{N}$ (Fig. 5.17(a)).

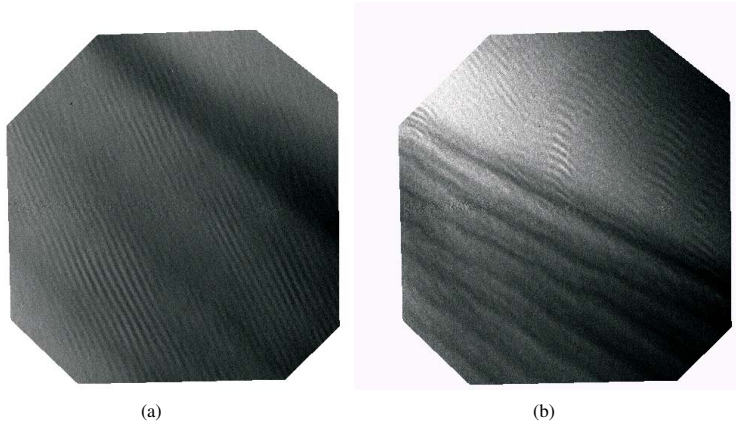


Figure 5.17: Waves observed in (a) middle ($\sim 45^\circ\text{N}$) and (b) high ($\sim 60^\circ\text{N}$) latitudes from VMC/VEx.

5.5 Other cyclostrophic systems

Venus, Earth, Mars and Titan provide a representative set of terrestrial atmospheres that allow one to study their dynamics and meteorology for broad range of conditions. Venus plays an important role as a natural laboratory to investigate the circulation on a slowly rotating planet. The basic processes maintaining super-rotation and other dynamical features of Venus circulation are still poorly understood. Therefore, comparing the dynamics and circulation of terrestrial planets (including Titan) and applying methods and techniques used to investigate one planet also to other planets will provide a better understanding of the current conditions and evolution of their climate. Venus is not the only body in the solar system where cyclostrophic approximation is valid. Saturn's satellite Titan, like Venus, is a slow rotator and the strong zonal winds in its stratosphere are in cyclostrophic balance. The cyclostrophic approximation is also valid on smaller scales, such as in Earth cyclones or Mars and Earth dust devils. Cyclostrophic balance is satisfied when the Coriolis force is negligible compared to the centrifugal force, that is for flows characterised by large Rossby number. The Rossby number, Ro , is the ratio of inertial to Coriolis forces, and is defined by:

$$Ro = \frac{V}{2\Omega L} \quad (5.9)$$

where V is the flow speed, L is a length characteristic of the flow, and Ω is the angular velocity of the planet's rotation. Table 5.1 compares the values of Rossby number for different systems. The comparison between Venus and Titan super-rotation, between Venus polar vortex and Earth cyclones, and Earth stratospheric polar vortices are only an example of the potentiality of comparative meteorology.

	Rossby number Ro
Venus	$\sim 10^3$
Earth	~ 1
Titan	$\gg 1$
Dust devils	$\sim 10^2 - 10^3$
Tornadoes	$\sim 10^3$
Hurricanes	$\gg 1$

Table 5.1: Values of Rossby number for different systems.

	Venus	Earth	Titan
Distance from the Sun (AU)	0.7	1	10
Radius (km)	6052	6376	2575
Surface pressure (bar)	92	1	1.5
Surface temperature (K)	730	288	94
Rotation period (Earth days)	243	1	16
Main atmospheric constituents	CO ₂ 97%	N ₂ 79%	N ₂ 95%
	N ₂ 3%	O ₂ 18%	CH ₄ 5%
		Ar 1%	
		H ₂ O 2%	
		CO ₂ 0.035%	
Bond albedo	0.76	0.3	0.2
Radiative Equilibrium temperature (K)	230	255	85
Scale height (km)	16	8.5	20 – 40

Table 5.2: Approximate value of parameters relevant to the climate of Venus, Earth and Titan (Taylor, 2006a).

5.5.1 Super-rotation on Titan

Saturn's giant moon, Titan, is unique in the solar system and owes one of the most intriguing atmospheres: its thick atmosphere is dominated by nitrogen and methane, and characterised by an extremely complex dynamics. Titan present many similarities to Venus and to the Earth (Taylor, 2006a), as can be seen in table 5.2. Titan's surface pressure is approximately 50 per cent larger than the Earth's, but it is much colder. Methane is the principal greenhouse gas and it causes Titan's surface temperature to increase by 12 K above the radiative equilibrium temperature. Like Venus, Titan is a slow rotating planet: it is tidally locked with Saturn and presents always the same face toward Saturn, so that its day has the same length that its orbital period, which is ~ 15.9 Earth days. Observations have shown the presence in Titan's stratosphere of strong zonal winds; therefore, like on Venus, the global wind system is cyclostrophic (Achterberg et al., 2008). Unlike Venus, however, Titan experiences seasons because of Saturn's obliquity of 26.7° . Figure 5.18(a) displays the vertical structure of Titan's atmospheric temperature observed by the Cassini Composite Infrared Radiometer-Spectrometer (CIRS) instrument on the NASA Cassini Saturn Orbiter. For pressure greater than ~ 0.5 mbar, the warmest temperatures occur at the equator with much larger gradients in the northern (winter) hemisphere than in the southern hemisphere (Fig. 5.18). At lower pressures, temperatures in the North Polar region are the warmest in the atmosphere, with values higher than 200 K (Achterberg et al.,

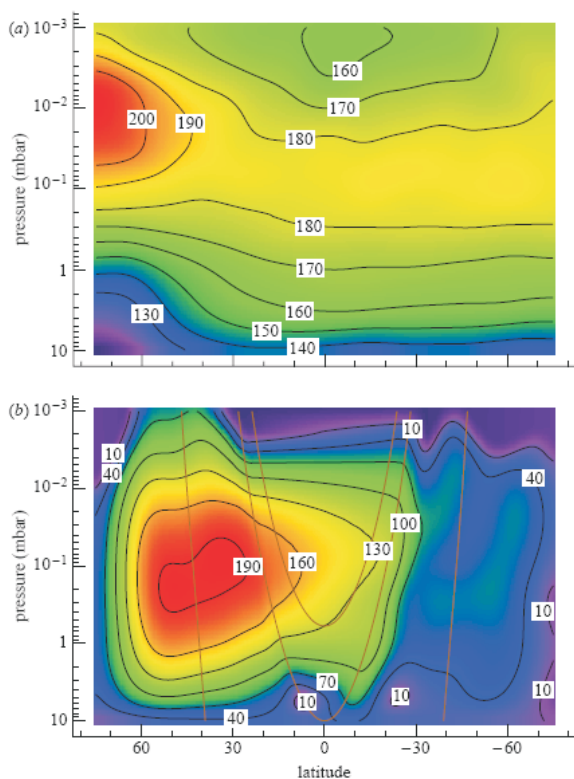


Figure 5.18: (a) Meridional cross section of temperature (K) derived from CIRS limb and nadir spectra in the mid-infrared. (b) Zonal winds (m s^{-1}) derived from temperature in figure (a) applying the thermal wind equation (Achterberg et al., 2008).

2008). Applying the thermal wind equation (3.5), zonal winds have been derived from temperatures in figure 5.18(a). As can be observed in figure 5.18(b), the main feature of the wind field is a broad midlatitude jet with a maximum speed of 190 m s^{-1} extending between 30° and 55° N and centered at an altitude of $0.1 - 0.2$ mbar. The jet is directly driven from the large gradient in temperatures observed at the level of the cold North Pole (Fig. 5.18(a)). In the Southern hemisphere, the winds are much slower, in consistence with the weaker meridional temperature gradients. Observations from CIRS have shown an enhancements in the abundance of nitriles and some trace hydrocarbons (HCN , HC_3N , C_2H_2 , C_3H_4 , and C_4H_2) at latitudes within and poleward of the jet (Flasar et al., 2005). These species act as atmospheric tracers and can be used to probe the dynamics of the polar vortex.

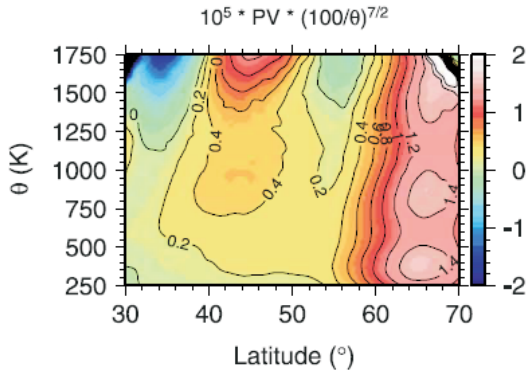


Figure 5.19: Potential vorticity derived from temperature field of Achterberg et al. (2008) and applying the thermal wind equation Teanby et al., 2008.

In a recent paper, Teanby et al. (2008) has derived potential vorticity map (Equation 5.6) from the zonal thermal winds (Fig. 5.19). The derived potential vorticity field displays a strong horizontal gradient occurring poleward of the midlatitude jet in correspondence with the observed composition enhancement. This provides a strong evidence of that the vortex acts as a mixing barrier in the stratosphere and mesosphere which inhibits mixing by planetary waves across it. The structure of Titan's winter polar stratosphere is similar in many respects to the winter polar vortex on Earth: a similar dynamical isolation occurs also in Earth's Antarctic polar vortex, causing depletion of trace species and producing an ozone hole within the vortex (Teanby et al., 2008).

5.5.2 Dust devils on Earth and Mars

Dust devils are low pressure, warm-core vortices found on both Earth (Fig. 5.20) and Mars (Fig. 5.21). They are characterised by high rotating wind speeds, significant electrostatic fields and are made visible by up-lifted dust and sand. They are distinct from tornadoes in that tornadoes are associated with thunderstorms, while dust devils form under clear skies. Moreover, dust devils are powered only by insolation, rather than release of latent heat, as in the case of tornadoes (Balme and Greeley, 2006). Dust devils are efficient erosional agents and can lift substantial amounts of dust-grade particles changing in this way the surface albedo and affecting the climate and air quality. On Earth, investigations of dust devils is fundamental to understand their role in convection, arid zone erosion and their danger to light and unpowered aircraft. On Mars, dust devils can have an important effect on the global dust cycle and in view of future robotic and perhaps first human missions is necessary to understand their potential hazards.

Observations on Earth: Dust devils usually occur in the summer in hot desert regions.



Figure 5.20: A large dust devil observed in the Arizona desert. Credit: NASA.



Figure 5.21: A dust devil on Mars photographed by the Spirit rover. Credit: NASA.

The frequency of occurrence of dust devils seems to be affected by many factors such as the season, time of day, and location. From observations, the most active dust devils regions appear to be arid, flat surfaces, especially those close to irrigated fields. Dust devils form most frequently in the late morning and the early afternoon. There is some evidence that a period of particularly intense dust devil activity is followed by a more quiescent period. Terrestrial dust devils are transient events and most last for only a few minutes. However, rare occurrences of large dust devils with lifetimes of 30 min to several hours have been reported (Balme and Greeley, 2006). Dust devils range in height from a few meters to over 1 km and are generally less than 100 m in diameter. They vary widely in morphology: from columnar to inverted cones to disordered, rotating dust clouds. Sin-

clair (1969a) has divided the vertical structure of a typical dust devil into three regions. Region 1 is the surface interface region, heavily loaded with particles. It includes the vortex boundary layer in which turbulent inflow occurs toward the center of the dust devil. Region 2 is the main part of the dust devil and it is characterised by a near-vertical column of rotating dust with little exchange of dust between the column and the surrounding air. Region 3, at the top of the dust devil, is where the rotation decays and dust is expelled outside the main column of air. Accurate wind speed, temperature, pressure, and dust load measurements can be acquired by in situ or remote sensing observations. Temperature measurements have shown the presence of a warm core surrounded by a cooler ring of air. Temperature excursions in the core can be as great as 20°C. In addition to the positive temperature excursion, negative pressure excursions or "pressure wells" are common at the centre of dust devils. Measurements of the rotation sense have shown that dust devils have no preferred sense of rotation, in agreement with theory. Within the dust devil, horizontal wind speed reaches values of about 25 m s⁻¹, while vertical wind speed is generally < 10 m s⁻¹. Significant electrostatic fields have been observed in dust devils caused by the contact between grains and between grains and the surface.

Observations on Mars: Dust devils on Mars were first identified in Viking orbiter images as small bright clouds with long conic shadows (Thomas and Gierasch, 1985). In addition to active dust devils, dust devil tracks were seen in the Mars Orbiter Camera images (Balme and Greeley, 2006) and were also imaged directly from the surface by a large number of landers (Metzger et al., 1999; Schofield et al., 1997). Martian and terrestrial dust devils seem to be similar in morphology. However, Martian dust devils appear to be an order of magnitude larger than terrestrial ones, often a few kilometers high and hundreds of meters in diameter with narrow bases and broader tops (Thomas and Gierasch, 1985). Dust devils activity follows the season of maximum insolation: most dust devil tracks are seen in images taken during regional spring and summer (Balme et al., 2003) and most vortices occur between 1200 and 1300 local time, as for terrestrial dust devils. Data on wind speed, temperature and pressure are scarce. Wind speeds calculated from meteorology data acquired by Viking 1 and 2 landers show a maximum speed of 42 m s⁻¹ at 1.6 m height (Ryan and Lucich, 1983). But wind speeds of up to ~ 100 m s⁻¹ were inferred for vortices that passed within about five core radii of the sensors (Ringrose et al., 2003). Positive temperature excursions within vortices measured by the Viking showed values similar to terrestrial measurements. Mars Pathfinder recorded pressure drops from ~ 0.5 to ~ 5 Pa (Murphy and Nelli, 2002). As on Earth, any preference for rotation sense was found (Ryan and Lucich, 1983; Ringrose et al., 2003).

Formation and maintenance of dust devils: Conditions necessary for the formation of dust devils are (Sinclair, 1969a):

- A superadiabatic lapse rate², causing an unstable stratified atmosphere and strong convection. The frequency and size of dust devils seem to be controlled by the strength of the superadiabatic lapse rate: stronger superadiabatic lapse rate are associated with more and larger dust devils (Ryan and Carroll, 1970).

²A lapse rate steeper than the dry adiabat. Superadiabatic lapse rates usually only occur near the surface as a result of insolation of dry soil under clear skies and windless conditions.

- A source of vorticity. A variety of vorticity sources has been hypothesised. Observations on Earth have shown that dust devils form frequently near the boundary of irrigated fields (Sinclair, 1969b), this has led Renno et al. (2004) to suggest that a vorticity source could be horizontal atmospheric vortices formed from the contrast between cold and warm air currents that are then moved in the vertical by convection. On Mars, numerical simulations have shown that dust devils are generated purely through the action of convection.
- A supply of sand, dust or debris.

Rennó et al. (1998) proposed a simple thermodynamical model which provides a physical interpretation for many of the observed characteristics of dust devils. Rennó et al. (1998) describes a dust devil as a heat engine: heat engines are devices that convert heat into mechanical energy; therefore, any natural convective phenomenon is an heat engine. Steady states vortices are modelled assuming that the heat input is due to surface heat flux from insolation, that heat output is in the form of thermal radiation emitted by air parcels subsiding outside of the vortex, and that losses are due to mechanical friction at the surface. Renno's theory predicts that the potential pressure depression between the centre of a dust devils and its environment is a function only of the ambient thermodynamic variables. Thus, given the environmental conditions, the potential pressure depression of a dust devil is a known variable. In addition, dust devils are assumed to be in cyclostrophic balance. Estimated values of Rossby number for terrestrial and Martian dust devils reach orders of magnitude of $\sim 10^2 - 10^3$ (Table 5.1). As a result, in dust devils the Coriolis force is negligible, and balance is between pressure and centrifugal forces. Applying cyclostrophic balance, wind speed around dust devils can be directly derived from the pressure drop. Thus, the wind speed and the value of the pressure depression of a dust devil depend only on the thermodynamics of its heat engine, which is governed by environmental conditions. The Renno thermodynamic model has been used to describe individual dust devils both on Earth and Mars.

5.5.3 Tornadoes and hurricanes on Earth

Other small scale cyclostrophic systems are hurricanes and tornadoes; they are characterised by a low pressure centre and strong winds. Typical values of the Rossby number (Eq. 5.9) for tornadoes and the core of a hurricane are respectively $\sim 10^3$ and $\gg 1$ (Table 5.1). Therefore, the Coriolis force can be neglected in tornadoes and hurricanes, and balance can be assumed between centrifugal and pressure gradient forces.

Tornado: According to the Glossary of Meteorology (AMS 2000), a tornado is a violently rotating column of air, in contact with the ground and the cloud base, and often (but not always) visible as a funnel cloud (Fig. 5.22). Most tornadoes have wind speeds between 18 m s^{-1} and 135 m s^{-1} . Its vortex has a typical diameter of few hundred meters and usually rotates cyclonically (counterclockwise) in the Northern Hemisphere. Tornadoes occur on all continents but are most common in the United States, where the average number of reported tornadoes is roughly 1000 per year, with the majority of them on the central plains and in the southeastern states. Tornadoes are associated with heavy thunderstorms and are powered by warm, moist inflow. Generally they are the result of instability



Figure 5.22: One of the several tornadoes observed by the VORTEX-99 team on May 3, 1999, in central Oklahoma (copyright National Oceanic and Atmospheric Administration (NOAA)).

due to temperature and moisture differences between the surface and the upper levels of the thunderstorm (Houghton, 1986).

Hurricane: Hurricane is the name used to indicate tropical cyclones occurring in the Atlantic or eastern Pacific oceans. Hurricanes are marked by a calm central region of sinking air, the eye, enclosed by strong thunderstorms associated to intense winds and rains. As in the case of tornadoes, the energy of tropical hurricanes is provided principally by release of latent heat in moist air (Houghton, 1986). Hurricanes on Earth form in tropical regions above warm oceans, and break up when they move over land, where their heat source is cut off and their strength diminishes rapidly (de Pater and Lissauer, 2001).

Recently, Limaye et al. (2009) has highlighted the presence of dynamical and morphological similarities between the Venus polar vortex and tropical cyclones on Earth (Fig. 5.23). Venus vortex and hurricanes are characterised by a different horizontal scale and lifetime: Venus vortex has a radial size of 12,000 km and it appears to be permanent; the largest tropical cyclones observed on Earth have a radius of less than 1000 km and last about one to two week in their mature phase. Energy source is also different for Venus vortex and Earth hurricanes: source of energy for hurricanes is the release of latent heat; Venus polar vortex, instead, receives a supply of energy from the deposition of solar radiation at cloud level and from thermal emission in the lower atmosphere. Despite their differences, Venus vortex and hurricanes circulation are very similar, both include features in the core region, such as transverse waves on spiral bands, which appear to be produced by barotropic instability (Limaye et al., 2009). From the comparison between Venus and Earth vortices a deeper understanding of Venus dynamics can be achieved.

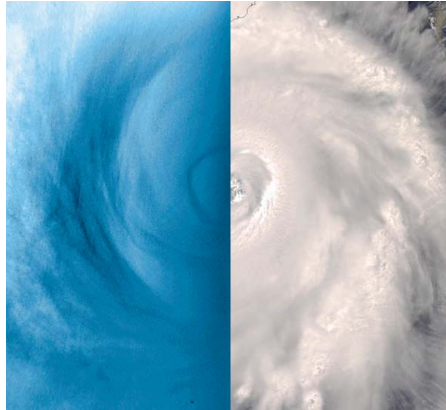


Figure 5.23: (*left*) VMC images of Venus south polar vortex; (*right*) Hurricane Frances on Earth (Limaye et al., 2009).

6 Conclusions and outlook

6.1 Conclusions

In this dissertation we investigated the dynamics of Venus mesosphere, using observations by the Venus Express (VEx) mission. Venus Express has acquired a wealth of data on atmospheric structure and dynamics with complete coverage in latitude and solar time that lacked in previous missions. The temperature structure of Venus mesosphere is investigated by two experiments on board Venus Express: VIRTIS (Visible and Infrared Thermal Imaging Spectrometer) and VeRa (Radio Science Experiment). In addition, Venus Monitoring Camera (VMC/VEx) is providing UV images used to measure cloud-tracked winds at cloud top (Chapter 2). In the frame of this work, zonal thermal winds were derived from the VIRTIS and VeRa temperature sounding by applying the thermal wind equation and were compared to the cloud-tracked winds to validate the cyclostrophic assumption. Thanks to Venus Express capabilities, the variability of zonal wind with latitude, altitude and local time was analysed in detail. The main results of this work are summarised in the following.

- Zonal thermal winds were derived from VIRTIS and VeRa temperature retrievals using an approximation of the thermal wind equation that implies the balance between the equatorward component of the centrifugal force and the meridional pressure gradient. This equation gives a possibility to reconstruct the zonal wind u if the temperature field is known, together with a suitable lower boundary condition on u . The main features of the retrieved thermal winds are: (1) a midlatitude jet with a maximum speed up to $140 \pm 15 \text{ m s}^{-1}$ centered around 50°S latitude at 70 km altitude; (2) the fast decrease of the wind speed from 60°S toward the pole; (3) the decrease of the wind speed with height above the jet (Fig. 4.3(b); 4.8). These results agree well with the thermal wind pattern derived from the earlier temperature soundings.
- The sensitivity of the zonal thermal wind to the lower boundary condition on u was tested by applying different velocities as lower boundary condition (Fig. 4.11; 4.12). Results showed that zonal winds are only slightly affected by the choice of boundary condition with a maximum difference of $\sim 20 \text{ m s}^{-1}$ in the region of the midlatitude jet (Section 4.3). We also applied an alternative form of the cyclostrophic equation to the VeRa temperature field. Equation (3.11) does not require integration, and thus retrieved thermal wind is independent on lower boundary condition. Comparison between zonal wind fields obtained from both retrieval methods confirmed the weak dependence of the retrieved zonal wind field on the

lower boundary condition (Section 4.2.3).

- VIRTIS observations completely cover the night side of the Southern hemisphere. This allowed to analyse the behaviour of temperature and zonal wind during the night. The temperature field shows a radiative cooling of ~ 15 K of the night side atmosphere at cloud tops (Fig. 2.6), which has also an effect on the zonal wind field. The midlatitude jet speed increases by $10 - 20$ m s^{-1} during the night (Fig. 4.5). However, any conclusion must be taken cautiously, since the weak change of wind speed with local time is within the uncertainties on wind speed itself (~ 15 m s^{-1}).
- The synergy between temperature soundings and the imaging observations on board Venus Express gave a unique chance to test the cyclostrophic approximation by comparing zonal thermal winds to the winds derived from tracking UV cloud markings. Cyclostrophic winds showed satisfactory agreement with the cloud-tracked winds derived from the Venus Monitoring Camera (VMC/VEx) UV images at $30 - 70^\circ$ latitudes (Fig. 5.3; 5.4), meaning that the cyclostrophic balance governs the circulation at these latitudes. A disagreement is observed at the equator and near the pole where the cyclostrophic approximation ceases to be valid. The breakdown of the cyclostrophic balance implies that other forces, such as turbulent motions, vertical viscosities, and eddies, become dominant in the original Navier-Stokes equation.
- Knowledge of both temperature and wind fields allowed us to study stability of the atmosphere with respect to convection and turbulence. The Richardson number Ri is an important parameter used to predict the occurrence of turbulence (Eq. 5.3). High positive values of Ri indicate a stable atmosphere. A statically unstable atmosphere sustained by convection is characterised by a negative value of Ri . A low positive value of Richardson number ($Ri \lesssim 1$) can indicate turbulence. The Richardson number was evaluated from zonal field of measured temperatures and thermal winds. The atmosphere is characterised by a low value of Richardson number from ~ 45 km up to ~ 60 km altitude at all latitudes that corresponds to the lower and middle cloud layer (Fig. 5.11). Convective regions ($Ri < 0$) are seen only in very shallow layers within the middle cloud deck. A high value of Richardson number was found in the region of the midlatitude jet indicating highly stable atmosphere. This distribution of stability is in qualitative agreement with VMC imaging, that shows turbulent cloud patterns in low-middle latitudes and laminar flow at middle-high latitudes (Section 5.2.1).
- As shown by previous studies, planetary waves arisen from horizontal shear instabilities of the zonal flow (barotropic instability) are expected to play an important role in the maintenance of the circulation. The necessary condition for barotropic instability was verified (Eq. 5.8): it is satisfied on the poleward side of the midlatitude jet, indicating the possible presence of wave instability (Fig. 5.16). Different types of wave patterns were also observed at middle to high Northern latitudes in VMC images (Markiewicz et al., 2007).

6.2 Future work and outlook

This work is opened to further development. The cyclostrophic balance allows to obtain information on the zonal circulation at altitudes where direct observations of winds are not possible. Although the cyclostrophic approximation is the simplest form of the thermal wind equation, it describes well the general features of zonal flow. However, a more detailed view of Venus circulation can be obtained by using a more accurate form of the thermal wind equation which takes into account the meridional component of wind whose magnitude is $\sim 15 \text{ m s}^{-1}$. Terms in the Navier-Stokes equations responsible for eddies, turbulent motions and vertical viscosities, can be particularly important at high latitudes and could be estimated by using General Circulation Models (GCMs). Different instruments on Venus Express revealed the presence of propagating waves at cloud levels (Markiewicz et al., 2007; Peralta et al., 2008). These could be playing an important role in the maintenance of the atmospheric circulation of Venus, as well as wind temporal variability observed at various time scales in the mesosphere. Detailed studies of these instabilities could help in understanding the mechanism of super-rotation. Limaye et al. (2009) first noted morphological similarities between Venus polar vortex and a tropical cyclone on Earth, although the Venus planetary vortex is 3 – 4 times larger. Numerical modelling of the barotropic instability in the vortex managed to reproduce variable shapes observed in the polar eye (Limaye et al., 2009). VIRTIS and VMC on board Venus Express are providing multispectral high resolution images of the polar vortex in the Southern hemisphere. Comparison and combination of observations obtained using different techniques supported by numerical modelling and comparison with vortices on Earth can allow for the first time to derive a description of the polar dynamics and its evolution in time.

For the future, the Japanese Planet-C orbiter (Akatsuki), expected to be launched in May 2010 (Nakamura et al., 2007), will join Venus Express, whose mission has been extended until 2012. Akatsuki will orbit Venus in an equatorial orbit; the angular velocity of the spacecraft is roughly synchronised with the super-rotational flow near the cloud base ($\sim 50 \text{ km}$ altitude), thus providing long term tracking of cloud features and allowing to measure the meridional circulation, mid-latitude jets and various wave activities. The joint effort of Venus Express and of the Venus Climate orbiter will allow to obtain for the first time ever long term observations of the atmosphere dynamics taken simultaneously from different perspectives. In the more distant future it is scheduled to modify the orbit of Venus Express by aerobraking and bringing the apocentre closer to the planet (Titov et al., 2009). The low eccentricity orbit will allow to increase the resolution of images of the Southern hemisphere. Yet, there are many questions which cannot be addressed by orbital measurements alone and require long term in-situ observations. A possible scenario would be the employment of several balloons at variable altitudes transported by the super-rotation around the planet and slowly driven toward the poles by the meridional circulation (The Eve Team et al., 2009).

A The adiabatic lapse rate in Venus atmosphere

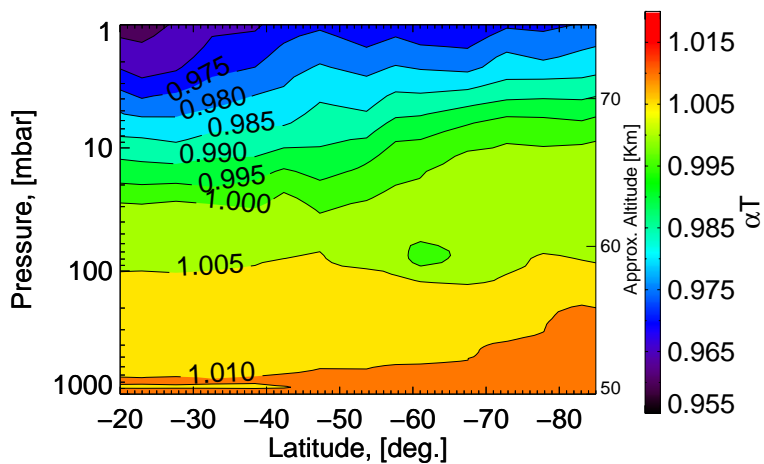
The adiabatic lapse rate used in evaluating the static stability (Eq. 5.1) has been derived for a real gas following the method adopted by Seiff et al. (1980). An atmosphere composed by pure CO₂ has been assumed. As showed by Seiff et al. (1980), the influence of trace constituents on the computation of Γ is negligible. The relation used to derive Γ is (Staley, 1970):

$$\Gamma = -\alpha T \frac{g}{C_p} \tag{A.1}$$

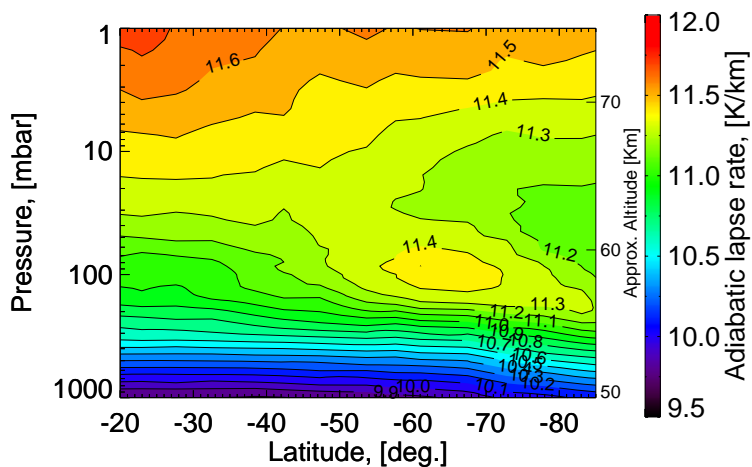
where $C_p = C_p(T, p)$ is the specific heat at constant pressure, ρ density, p pressure, T temperature, and g gravity. The factor αT , which is unity for a perfect gas, has been evaluated from:

$$\alpha = -\frac{1}{\rho} \left(\frac{\partial \rho}{\partial T} \right)_p \tag{A.2}$$

The partial derivative in (A.2) has been evaluated from the Hilsenrath (1960) tables. Specific heats are also provided by Hilsenrath (1960). Values of g at different altitudes in Venus atmosphere were taken from the VIRA model (Seiff et al., 1985). The correction factor αT ranges from 0.95 to 1.01 in the pressure range 1000 – 1 mbar. The results of the calculations are displayed in figures A.1. Hilsenrath (1960) tables are limited to a minimum pressure of 10 mbar. Values of the correction factor αT and of Γ in the pressure range 10 – 1 mbar were obtained from interpolation and must be considered cautiously. For a complete discussion of Γ see Staley (1970).



(a)



(b)

Figure A.1: Contour plots of (a) the correction factor αT ; (b) the adiabatic lapse rate for a pure CO_2 atmosphere.

Bibliography

- R. K. Achterberg, B. J. Conrath, P. J. Gierasch, F. M. Flasar, and C. A. Nixon. Titan's middle-atmospheric temperatures and dynamics observed by the Cassini Composite Infrared Spectrometer. *Icarus*, 194:263–277, 2008. doi: 10.1016/j.icarus.2007.09.029.
- B. Ahmad and G. L. Tyler. Progress in Understanding Horizontal Resolution of Radio Occultation Measurements. In *Bulletin of the American Astronomical Society*, volume 29 of *Bulletin of the American Astronomical Society*, page 969, July 1997.
- D. A. Allen and J. W. Crawford. Cloud structure on the dark side of Venus. *Nature*, 307: 222–224, 1984. doi: 10.1038/307222a0.
- M. Allison, A. D. del Genio, and W. Zhou. Zero potential vorticity envelopes for the zonal-mean velocity of the Venus/Titan atmospheres. *Journal of Atmospheric Sciences*, 51:694–702, 1994. doi: 10.1175/1520-0469(1994)051.
- D. G. Andrews. *An Introduction to Atmospheric Physics*. 2000.
- D. G. Andrews, J. R. Holton, and C. B. Leovy. *Middle atmosphere dynamics*. 1987.
- N. L. Baker and C. B. Leovy. Zonal winds near Venus' cloud top level - A model study of the interaction between the zonal mean circulation and the semidiurnal tide. *Icarus*, 69:202–220, 1987. doi: 10.1016/0019-1035(87)90100-X.
- M. Balme and R. Greeley. Dust devils on Earth and Mars. *Reviews of Geophysics*, 44: 3003, 2006. doi: 10.1029/2005RG000188.
- M. R. Balme, P. L. Whelley, and R. Greeley. Mars: Dust devil track survey in Argyre Planitia and Hellas Basin. *Journal of Geophysical Research (Planets)*, 108:5086, 2003. doi: 10.1029/2003JE002096.
- S. Barabash, J.-A. Sauvaud, H. Gunell, H. Andersson, A. Grigoriev, K. Brinkfeldt, M. Holmström, R. Lundin, M. Yamauchi, K. Asamura, W. Baumjohann, T. L. Zhang, A. J. Coates, D. R. Linder, D. O. Kataria, C. C. Curtis, K. C. Hsieh, B. R. Sandel, A. Fedorov, C. Mazelle, J.-J. Thocaven, M. Grande, H. E. J. Koskinen, E. Kallio, T. Säles, P. Riihela, J. Kozyra, N. Krupp, J. Woch, J. Luhmann, S. McKenna-Lawlor, S. Orsini, R. Cerulli-Irelli, M. Mura, M. Milillo, M. Maggi, E. Roelof, P. Brandt, C. T. Russell, K. Szego, J. D. Winningham, R. A. Frahm, J. Scherrer, J. R. Sharber, P. Wurz, and P. Bochslers. The Analyser of Space Plasmas and Energetic Atoms (ASPERA-4) for the Venus Express mission. *Planetary and Space Science*, 55:1772–1792, 2007. doi: 10.1016/j.pss.2007.01.014.

- F. J. Beron-Vera, M. G. Brown, M. J. Olascoaga, I. I. Rypina, H. Koçak, and I. A. Udovychenkov. Zonal Jets as Transport Barriers in Planetary Atmospheres. *Journal of Atmospheric Sciences*, 65:3316, 2008. doi: 10.1175/2008JAS2579.1.
- J.-L. Bertaux, D. Nevejans, O. Korablev, E. Villard, E. Quémerais, E. Neefs, F. Montmessin, F. Leblanc, J. P. Dubois, E. Dimarellis, A. Hauchecorne, F. Lefèvre, P. Rannou, J. Y. Chaufray, M. Cabane, G. Cernogora, G. Souchon, F. Semelin, A. Reberac, E. van Ransbeek, S. Berkenbosch, R. Clairquin, C. Muller, F. Forget, F. Hourdin, O. Talagrand, A. Rodin, A. Fedorova, A. Stepanov, I. Vinogradov, A. Kiselev, Y. Kalinnikov, G. Durrý, B. Sandel, A. Stern, and J. C. Gérard. SPICAV on Venus Express: Three spectrometers to study the global structure and composition of the Venus atmosphere. *Planetary and Space Science*, 55:1673–1700, 2007. doi: 10.1016/j.pss.2007.01.016.
- S. W. Bougher, M. J. Alexander, and H. G. Mayr. Upper Atmosphere Dynamics: Global Circulation and Gravity Waves. In S. W. Bougher, D. M. Hunten, & R. J. Philips, editor, *Venus II: Geology, Geophysics, Atmosphere, and Solar Wind Environment*, page 259, 1997.
- R. W. Carlson, K. H. Baines, L. W. Kamp, P. R. Weissman, W. D. Smythe, A. C. Ocampo, T. V. Johnson, D. L. Matson, J. B. Pollack, and D. Grinspoon. Galileo infrared imaging spectroscopy measurements at Venus. *Science*, 253:1541–1548, 1991. doi: 10.1126/science.253.5027.1541.
- R. T. Clancy and D. O. Muhleman. Long-term (1979-1990) changes in the thermal, dynamical, and compositional structure of the Venus mesosphere as inferred from microwave spectral line observations of C-12O, C-13O, and CO-18. *Icarus*, 89:129–146, 1991. doi: 10.1016/0019-1035(91)90093-9.
- R. T. Clancy, B. J. Sandor, and G. H. Moriarty-Schieven. Venus upper atmospheric CO₂ temperature, and winds across the afternoon/evening terminator from June 2007 JCMT sub-millimeter line observations. *Planetary and Space Science*, 56:1344–1354, 2008. doi: 10.1016/j.pss.2008.05.007.
- E. Cochrane. Book Review: The many faces of Venus / Aeon Press, 2001. *Culture and Cosmos*, 6:75, 2002.
- C. C. Counselman, S. A. Gourevitch, R. W. King, G. B. Lorient, and E. S. Ginsberg. Zonal and meridional circulation of the lower atmosphere of Venus determined by radio interferometry. *Journal of Geophysical Research*, 85:8026–8030, 1980. doi: 10.1029/JA085iA13p08026.
- D. Crisp, A. P. Ingersoll, C. E. Hildebrand, and R. A. Preston. VEGA balloon meteorological measurements. *Advances in Space Research*, 10:109–124, 1990. doi: 10.1016/0273-1177(90)90172-V.
- D. Crisp, S. McMuldroy, S. K. Stephens, W. M. Sinton, B. Ragent, K.-W. Hodapp, R. G. Probst, L. R. Doyle, D. A. Allen, and J. Elias. Ground-based near-infrared imaging observations of Venus during the Galileo encounter. *Science*, 253:1538–1541, 1991. doi: 10.1126/science.253.5027.1538.

- D. P. Cruikshank. *The development of studies of Venus*, pages 1–9. 1983.
- I. de Pater and J. J. Lissauer. *Planetary Sciences*. 2001.
- P. Drossart, G. Piccioni, A. Adriani, F. Angrilli, G. Arnold, K. H. Baines, G. Bellucci, J. Benkhoff, B. Bézard, J.-P. Bibring, A. Blanco, M. I. Blecka, R. W. Carlson, A. Coradini, A. di Lellis, T. Encrenaz, S. Erard, S. Fonti, V. Formisano, T. Fouchet, R. Garcia, R. Haus, J. Helbert, N. I. Ignatiev, P. G. J. Irwin, Y. Langevin, S. Lebonnois, M. A. Lopez-Valverde, D. Luz, L. Marinangeli, V. Orofino, A. V. Rodin, M. C. Roos-Serote, B. Saggin, A. Sanchez-Lavega, D. M. Stam, F. W. Taylor, D. Titov, G. Visconti, M. Zambelli, R. Hueso, C. C. C. Tsang, C. F. Wilson, and T. Z. Afanasenko. Scientific goals for the observation of Venus by VIRTIS on ESA/Venus express mission. *Planetary and Space Science*, 55:1653–1672, 2007. doi: 10.1016/j.pss.2007.01.003.
- V. R. Eshleman. The radio occultation method for the study of planetary atmospheres. *Planetary and Space Science*, 21:1521–1531, 1973. doi: 10.1016/0032-0633(73)90059-7.
- L. W. Esposito, R. G. Knollenberg, M. I. Marov, O. B. Toon, and R. P. Turco. The clouds are hazes of Venus. In Hunten, D. M., Colin, L., Donahue, T. M., & Moroz, V. I., editor, *Venus*, pages 484–564, 1983.
- L. W. Esposito, J.-L. Bertaux, V. Krasnopolsky, V. I. Moroz, and L. V. Zasova. Chemistry of Lower Atmosphere and Clouds. In S. W. Bougher, D. M. Hunten, & R. J. Philips, editor, *Venus II: Geology, Geophysics, Atmosphere, and Solar Wind Environment*, page 415, 1997.
- G. Fjeldbo, A. J. Kliore, and V. R. Eshleman. The Neutral Atmosphere of Venus as Studied with the Mariner V Radio Occultation Experiments. *Astronomical Journal*, 76:123, 1971. doi: 10.1086/111096.
- F. M. Flasar, R. K. Achterberg, B. J. Conrath, P. J. Gierasch, V. G. Kunde, C. A. Nixon, G. L. Bjoraker, D. E. Jennings, P. N. Romani, A. A. Simon-Miller, B. Bézard, A. Coustenis, P. G. J. Irwin, N. A. Teanby, J. Brasunas, J. C. Pearl, M. E. Segura, R. C. Carlson, A. Mamoutkine, P. J. Schinder, A. Barucci, R. Courtin, T. Fouchet, D. Gautier, E. Lellouch, A. Marten, R. Prangé, S. Vinatier, D. F. Strobel, S. B. Calcutt, P. L. Read, F. W. Taylor, N. Bowles, R. E. Samuelson, G. S. Orton, L. J. Spilker, T. C. Owen, J. R. Spencer, M. R. Showalter, C. Ferrari, M. M. Abbas, F. Raulin, S. Edgington, P. Ade, and E. H. Wishnow. Titan’s Atmospheric Temperatures, Winds, and Composition. *Science*, 308:975–978, 2005. doi: 10.1126/science.1111150.
- V. Formisano, F. Angrilli, G. Arnold, S. Atreya, K. H. Baines, G. Bellucci, B. Bézard, F. Billebaud, D. Biondi, M. I. Blecka, L. Colangeli, L. Comolli, D. Crisp, M. D’Amore, T. Encrenaz, A. Ekonomov, F. Esposito, C. Fiorenza, S. Fonti, M. Giuranna, D. Grassi, B. Grieger, A. Grigoriev, J. Helbert, H. Hirsch, N. Ignatiev, A. Jurewicz, I. Khatuntsev, S. Lebonnois, E. Lellouch, A. Mattana, A. Maturilli, E. Mencarelli, M. Michalska, J. Lopez Moreno, B. Moshkin, F. Nespola, Y. Nikolsky, F. Nuccilli, P. Orleanski, E. Palomba, G. Piccioni, M. Rataj, G. Rinaldi, M. Rossi, B. Saggin, D. Stam, D. Titov,

- G. Visconti, and L. Zasova. The planetary fourier spectrometer (PFS) onboard the European Venus Express mission. *Planetary and Space Science*, 54:1298–1314, 2006. doi: 10.1016/j.pss.2006.04.033.
- J. L. Fox and S. W. Bougher. Structure, luminosity, and dynamics of the Venus thermosphere. *Space Science Reviews*, 55:357–489, 1991. doi: 10.1007/BF00177141.
- B. Galperin, S. Sukoriansky, and P. S. Anderson. On the critical Richardson number in stably stratified turbulence. *Atmospheric Science Letters*, 8:65–69, 2007. doi: 10.1002/asl.153.
- P. J. Gierasch. Meridional circulation and the maintenance of the Venus atmospheric rotation. *Journal of Atmospheric Sciences*, 32:1038–1044, 1975. doi: 10.1175/1520-0469(1975)032.
- P. J. Gierasch, R. M. Goody, R. E. Young, D. Crisp, C. Edwards, R. Kahn, D. Rider, A. del Genio, R. Greeley, A. Hou, C. B. Leovy, D. McCleese, and M. Newman. The General Circulation of the Venus Atmosphere: an Assessment. In S. W. Bougher, D. M. Hunten, & R. J. Philips, editor, *Venus II: Geology, Geophysics, Atmosphere, and Solar Wind Environment*, page 459, 1997.
- J. J. Goldstein, M. J. Mumma, T. Kostiuk, D. Deming, F. Espenak, and D. Zipoy. Absolute wind velocities in the lower thermosphere of Venus using infrared heterodyne spectroscopy. *Icarus*, 94:45–63, 1991. doi: 10.1016/0019-1035(91)90140-O.
- D. Grassi, P. Drossart, G. Piccioni, N. I. Ignatiev, L. V. Zasova, A. Adriani, M. L. Moriconi, P. G. J. Irwin, A. Negrão, and A. Migliorini. Retrieval of air temperature profiles in the Venusian mesosphere from VIRTIS-M data: Description and validation of algorithms. *Journal of Geophysical Research (Planets)*, 113, 2008. doi: 10.1029/2008JE003075.
- R. A. Hanel, B. J. Conrath, D. E. Jennings, and R. E. Samuelson. *Exploration of the Solar System by Infrared Remote Sensing: Second Edition*. 2003.
- B. Häusler, M. Pätzold, G. L. Tyler, R. A. Simpson, M. K. Bird, V. Dehant, J.-P. Barriot, W. Eidel, R. Mattei, S. Remus, J. Selle, S. Tellmann, and T. Imamura. Radio science investigations by VeRa onboard the Venus Express spacecraft. *Planetary and Space Science*, 54:1315–1335, 2006. doi: 10.1016/j.pss.2006.04.032.
- J. Hilsenrath. *Tables of Thermodynamic and Transport Properties of Air, Argon, Carbon Dioxide, Carbon Monoxide, Hydrogen, Nitrogen, Oxygen and Steam*. Pergamon Press (U.K.), 1960.
- J. R. Holton. *An introduction to dynamic meteorology*. 2004.
- D. M. Houghton. Handbook of Applied Meteorology. Edited by David D. Houghton, John Wiley Sons. 1985. Pp 1461. *Quarterly Journal of the Royal Meteorological Society*, 112:561–562, 1986. doi: 10.1002/qj.49711247217.
- J. Houghton. *The Physics of Atmospheres*. 2002.

- J. T. Houghton, F. W. Taylor, and C. D. Rodgers. *Remote sounding of atmospheres*. 1984.
- N. I. Ignatiev, D. V. Titov, G. Piccioni, P. Drossart, W. J. Markiewicz, V. Cottini, T. Roatsch, M. Almeida, and N. Manoel. Altimetry of the Venus cloud tops from the Venus Express observations. *Journal of Geophysical Research (Planets)*, 114, 2009. doi: 10.1029/2008JE003320.
- J. M. Jenkins, P. G. Steffes, D. P. Hinson, J. D. Twicken, and G. L. Tyler. Radio occultation studies of the Venus atmosphere with the Magellan spacecraft. 2: Results from the October 1991 experiments. *Icarus*, 110:79–94, 1994. doi: 10.1006/icar.1994.1108.
- G. M. Keating, J. L. Bertaux, S. W. Bougher, R. E. Dickinson, T. E. Cravens, and A. E. Hedín. Models of Venus neutral upper atmosphere - Structure and composition. *Advances in Space Research*, 5:117–171, 1985. doi: 10.1016/0273-1177(85)90200-5.
- V. V. Kerzhanovich and S. S. Limaye. Circulation of the atmosphere from the surface to 100 KM. *Advances in Space Research*, 5:59–83, 1985. doi: 10.1016/0273-1177(85)90198-X.
- V. V. Kerzhanovich, N. M. Antsibor, R. V. Bakit'ko, V. P. Lysov, and E. P. Molotov. VEGA 1 and 2 - Vertical profiles of wind velocity according to Doppler measurements on the descent modules. *Kosmicheskie Issledovaniia*, 25:673–677, 1987.
- S. Lebonnois, F. Hourdin, V. Eymet, A. Cresspin, R. Fournier, and F. Forget. Superrotation of Venus atmosphere analysed with a full General Circulation Model. *Journal of Geophysical Research*, 2010. doi: 10.1029/2009JE003515. in press.
- E. Lellouch and O. Witasse. A coordinated campaign of Venus ground-based observations and Venus Express measurements. *Planetary and Space Science*, 56:1317–1319, 2008. doi: 10.1016/j.pss.2008.07.001.
- E. Lellouch, J. J. Goldstein, J. Rosenqvist, S. W. Bougher, and G. Paubert. Global circulation, thermal structure, and carbon monoxide distribution in Venus' mesosphere in 1991. *Icarus*, 110:315–339, 1994. doi: 10.1006/icar.1994.1125.
- E. Lellouch, T. Clancy, D. Crisp, A. J. Kliore, D. Titov, and S. W. Bougher. Monitoring of Mesospheric Structure and Dynamics. In S. W. Bougher, D. M. Hunten, & R. J. Philips, editor, *Venus II: Geology, Geophysics, Atmosphere, and Solar Wind Environment*, page 295, 1997.
- C. B. Leovy. Rotation of the upper atmosphere of Venus. *Journal of Atmospheric Sciences*, 30:1218–1220, 1973. doi: 10.1175/1520-0469(1973)030.
- S. S. Limaye. Venus atmospheric circulation - Observations and implications of the thermal structure. *Advances in Space Research*, 5:51–62, 1985. doi: 10.1016/0273-1177(85)90270-4.
- S. S. Limaye. Venus atmospheric circulation: Known and unknown. *Journal of Geophysical Research (Planets)*, 112:4, 2007. doi: 10.1029/2006JE002814.

- S. S. Limaye and V. E. Suomi. Cloud motions on Venus - Global structure and organization. *Journal of Atmospheric Sciences*, 38:1220–1235, 1981. doi: 10.1175/1520-0469(1981)038.
- S. S. Limaye, C. J. Grund, and S. P. Burre. Zonal mean circulation at the cloud level on Venus - Spring and fall 1979 OCPP observations. *Icarus*, 51:416–439, 1982. doi: 10.1016/0019-1035(82)90092-6.
- S. S. Limaye, J. P. Kossin, C. Rozoff, G. Piccioni, D. V. Titov, and W. J. Markiewicz. Vortex circulation on Venus: Dynamical similarities with terrestrial hurricanes. *Geophysical Research Letters*, 36:4204, 2009. doi: 10.1029/2008GL036093.
- B. Lipa and G. L. Tyler. Statistical and computational uncertainties in atmospheric profiles from radio occultation - Mariner 10 at Venus. *Icarus*, 39:192–208, 1979. doi: 10.1016/0019-1035(79)90163-5.
- W. J. Markiewicz, D. V. Titov, N. Ignatiev, H. U. Keller, D. Crisp, S. S. Limaye, R. Jaumann, R. Moissl, N. Thomas, L. Esposito, S. Watanabe, B. Fiethe, T. Behnke, I. Szemerey, H. Michalik, H. Perplies, M. Wedemeier, I. Sebastian, W. Boogaerts, S. F. Hviid, C. Dierker, B. Osterloh, W. Böker, M. Koch, H. Michaelis, D. Belyaev, A. Dannenberg, M. Tschimmel, P. Russo, T. Roatsch, and K. D. Matz. Venus Monitoring Camera for Venus Express. *Planetary and Space Science*, 55:1701–1711, 2007. doi: 10.1016/j.pss.2007.01.004.
- S. M. Metzger, J. R. Carr, J. R. Johnson, T. J. Parker, and M. T. Lemmon. Dust devil vortices seen by the Mars Pathfinder camera. *Geophysical Research Letters*, 26:2781–2784, 1999. doi: 10.1029/1999GL008341.
- D. V. Michelangeli, R. W. Zurek, and L. S. Elson. Barotropic instability of midlatitude zonal jets on Mars, earth and Venus. *Journal of Atmospheric Sciences*, 44:2031–2041, 1987. doi: 10.1175/1520-0469(1987)044.
- R. Moissl, I. Khatuntsev, S. S. Limaye, D. V. Titov, W. J. Markiewicz, N. I. Ignatiev, T. Roatsch, K.-D. Matz, R. Jaumann, M. Almeida, G. Portyankina, T. Behnke, and S. F. Hviid. Venus cloud top winds from tracking UV features in Venus Monitoring Camera images. *Journal of Geophysical Research (Planets)*, 114, 2009. doi: 10.1029/2008JE003117.
- J. R. Murphy and S. Nelli. Mars Pathfinder convective vortices: Frequency of occurrence. *Geophysical Research Letters*, 29(23):230000–1, 2002. doi: 10.1029/2002GL015214.
- M. Nakamura, T. Imamura, M. Ueno, N. Iwagami, T. Satoh, S. Watanabe, M. Taguchi, Y. Takahashi, M. Suzuki, T. Abe, G. L. Hashimoto, T. Sakanoi, S. Okano, Y. Kasaba, J. Yoshida, M. Yamada, N. Ishii, T. Yamada, K. Uemizu, T. Fukuhara, and K.-I. Oyama. Planet-C: Venus Climate Orbiter mission of Japan. *Planetary and Space Science*, 55: 1831–1842, 2007. doi: 10.1016/j.pss.2007.01.009.
- M. Newman and C. Leovy. Maintenance of strong rotational winds in Venus' middle atmosphere by thermal tides. *Science*, 257:647–650, 1992. doi: 10.1126/science.257.5070.647.

- M. Newman, G. Schubert, A. J. Kliore, and I. R. Patel. Zonal winds in the middle atmosphere of Venus from Pioneer Venus radio occultation data. *Journal of Atmospheric Sciences*, 41:1901–1913, 1984. doi: 10.1175/1520-0469(1984)041.
- M. Pätzold, B. Häusler, M. K. Bird, S. Tellmann, R. Mattei, S. W. Asmar, V. Dehant, W. Eidel, T. Imamura, R. A. Simpson, and G. L. Tyler. The structure of Venus' middle atmosphere and ionosphere. *Nature*, 450:657–660, 2007. doi: 10.1038/nature06239.
- M. Pätzold, B. Haeusler, S. Tellmann, M. K. Bird, and L. Tyler. The Structure of the Venus Ionosphere. *AGU Fall Meeting Abstracts*, page A1431, 2008.
- J. Peralta, R. Hueso, and A. Sánchez-Lavega. A reanalysis of Venus winds at two cloud levels from Galileo SSI images. *Icarus*, 190:469–477, 2007. doi: 10.1016/j.icarus.2007.03.028.
- J. Peralta, R. Hueso, A. Sánchez-Lavega, G. Piccioni, O. Lanciano, and P. Drossart. Characterization of mesoscale gravity waves in the upper and lower clouds of Venus from VEX-VIRTIS images. *Journal of Geophysical Research (Planets)*, 113, 2008. doi: 10.1029/2008JE003185.
- A. Piccialli, D. V. Titov, D. Grassi, I. Khatuntsev, P. Drossart, G. Piccioni, and A. Migliorini. Cyclostrophic winds from the Visible and Infrared Thermal Imaging Spectrometer temperature sounding: A preliminary analysis. *Journal of Geophysical Research (Planets)*, 113(12), 2008. doi: 10.1029/2008JE003127.
- R. A. Preston, C. E. Hildebrand, G. H. Purcell, J. Ellis, C. T. Stelzried, S. G. Finley, R. Z. Sagdeev, V. M. Linkin, V. V. Kerzhanovich, V. I. Altunin, L. R. Kogan, V. I. Kostenko, L. I. Matveenko, S. V. Pogrebenko, I. A. Strukov, E. L. Akim, Y. N. Alexandrov, N. A. Armand, R. N. Bakitko, A. S. Vyshlov, A. F. Bogomolov, Y. N. Gorchankov, A. S. Selivanov, N. M. Ivanov, V. F. Tichonov, J. E. Blamont, L. Boloh, G. Laurans, A. Boisshot, F. Biraud, A. Ortega-Molina, C. Rosolen, and G. Petit. Determination of Venus winds by ground-based radio tracking of the VEGA balloons. *Science*, 231:1414–1416, 1986. doi: 10.1126/science.231.4744.1414.
- P. L. Read, P. J. Gierasch, B. J. Conrath, A. Simon-Miller, T. Fouchet, and Y. H. Yamazaki. Mapping potential-vorticity dynamics on Jupiter. I: Zonal-mean circulation from Cassini and Voyager 1 data. *Quarterly Journal of the Royal Meteorological Society*, 132:1577–1603, 2006.
- M. Rengel, P. Hartogh, and C. Jarchow. HHSMT observations of the Venusian mesospheric temperature, winds, and CO abundance around the MESSENGER flyby. *Planetary and Space Science*, 56:1688–1695, 2008. doi: 10.1016/j.pss.2008.07.014.
- N. O. Rennó, M. L. Burkett, and M. P. Larkin. A Simple Thermodynamical Theory for Dust Devils. *Journal of Atmospheric Sciences*, 55:3244–3252, 1998. doi: 10.1175/1520-0469(1998)055<3244:ASTTFD>2.0.CO;2.
- N. O. Renno, V. J. Abreu, J. Koch, P. H. Smith, O. K. Hartogensis, H. A. R. De Bruin, D. Burose, G. T. Delory, W. M. Farrell, C. J. Watts, J. Garatuza, M. Parker,

- and A. Carswell. MATADOR 2002: A pilot field experiment on convective plumes and dust devils. *Journal of Geophysical Research (Planets)*, 109:7001, 2004. doi: 10.1029/2003JE002219.
- T. J. Ringrose, M. C. Towner, and J. C. Zarnecki. Viking Lander 1 and 2 Revisited: The Characterisation and Detection of Martian Dust Devils. In A. L. Albee & H. H. Kieffer, editor, *Sixth International Conference on Mars*, page 3017, 2003.
- C. D. Rodgers. Retrieval of Atmospheric Temperature and Composition From Remote Measurements of Thermal Radiation. *Reviews of Geophysics and Space Physics*, 14: 609, 1976.
- M. Roos-Serote, P. Drossart, T. Encrenaz, E. Lellouch, R. W. Carlson, K. H. Baines, F. W. Taylor, and S. B. Calcutt. The thermal structure and dynamics of the atmosphere of Venus between 70 and 90 KM from the Galileo-NIMS spectra. *Icarus*, 114:300–309, 1995. doi: 10.1006/icar.1995.1063.
- W. B. Rossow and G. P. Williams. Large-scale motion in the Venus stratosphere. *Journal of Atmospheric Sciences*, 36:377–389, March 1979. doi: 10.1175/1520-0469(1979)036.
- W. B. Rossow, A. D. del Genio, S. S. Limaye, and L. D. Travis. Cloud morphology and motions from Pioneer Venus images. *Journal of Geophysical Research*, 85:8107–8128, 1980. doi: 10.1029/JA085iA13p08107.
- W. B. Rossow, A. D. del Genio, and T. Eichler. Cloud-tracked winds from Pioneer Venus OCPP images. *Journal of Atmospheric Sciences*, 47:2053–2084, 1990. doi: 10.1175/1520-0469(1990)047.
- J. A. Ryan and J. J. Carroll. Dust Devil Wind Velocities: Mature State. *Journal of Geophysical Research*, 75:531–541, 1970. doi: 10.1029/JC075i003p00531.
- J. A. Ryan and R. D. Lucich. Possible dust devils - Vortices on Mars. *Journal of Geophysical Research*, 88:11005–11011, 1983. doi: 10.1029/JC088iC15p11005.
- A. Sánchez-Lavega, R. Hueso, G. Piccioni, P. Drossart, J. Peralta, S. Pérez-Hoyos, C. F. Wilson, F. W. Taylor, K. H. Baines, D. Luz, S. Erard, and S. Lebonnois. Variable winds on Venus mapped in three dimensions. *Geophysical Research Letters*, 35:13204, 2008. doi: 10.1029/2008GL033817.
- F. Schmuelling, J. Goldstein, T. Kostiuik, T. Hewagama, and D. Zipoy. High precision Wind measurements in the upper Venus atmosphere. In *Bulletin of the American Astronomical Society*, volume 32 of *Bulletin of the American Astronomical Society*, page 1121, 2000.
- J. T. Schofield, J. R. Barnes, D. Crisp, R. M. Haberle, S. Larsen, J. A. Magalhaes, J. R. Murphy, A. Seiff, and G. Wilson. The Mars Pathfinder Atmospheric Structure Investigation/Meteorology. *Science*, 278:1752, 1997.

- G. Schubert. General circulation and the dynamical state of the Venus atmosphere. In U. von Zahn, S. Kumar, H. Niemann, and R. Prinn, editors, *Venus*, pages 681–765, 1983.
- G. Schubert, C. Covey, A. del Genio, L. S. Elson, G. Keating, A. Seiff, R. E. Young, J. Apt, C. C. Counselman, A. J. Kliore, S. S. Limaye, H. E. Revercomb, L. A. Sromovsky, V. E. Suomi, F. Taylor, R. Woo, and U. von Zahn. Structure and circulation of the Venus atmosphere. *Journal of Geophysical Research*, 85:8007–8025, 1980. doi: 10.1029/JA085iA13p08007.
- G. Schubert, S. W. Bougher, C. C. Covey, A. D. Del Genio, A. S. Grossman, J. L. Hollingsworth, S. S. Limaye, and R. E. Young. Venus atmosphere dynamics: a continuing enigma. In L. W. Esposito, E. R. Stofan, & Th. E. Cravens, editor, *Exploring Venus as terrestrial planet*, volume 176, pages 121–138. Geophys. Monogr. Ser., 2007.
- A. Seiff. *Thermal structure of the atmosphere of Venus*, pages 215–279. 1983.
- A. Seiff, D. B. Kirk, R. E. Young, R. C. Blanchard, J. T. Findlay, G. M. Kelly, and S. C. Sommer. Measurements of thermal structure and thermal contrasts in the atmosphere of Venus and related dynamical observations - Results from the four Pioneer Venus probes. *Journal of Geophysical Research*, 85:7903–7933, 1980. doi: 10.1029/JA085iA13p07903.
- A. Seiff, J. T. Schofield, A. J. Kliore, F. W. Taylor, and S. S. Limaye. Models of the structure of the atmosphere of Venus from the surface to 100 kilometers altitude. *Advances in Space Research*, 5:3–58, 1985. doi: 10.1016/0273-1177(85)90197-8.
- K. P. Shah, D. O. Muhleman, and G. L. Berge. Measurement of winds in Venus' upper mesosphere based on Doppler shifts of the 2.6-mm (C-12)O line. *Icarus*, 93:96–121, 1991. doi: 10.1016/0019-1035(91)90167-R.
- P. C. Sinclair. *General characteristics of dust devils*. Ph.D. thesis. Univ. of Ariz., Tucson, 1969a.
- P. C. Sinclair. General Characteristics of Dust Devils. *Journal of Applied Meteorology*, 8:32–45, 1969b. doi: 10.1175/1520-0450(1969).
- M. Sornig, T. Livengood, G. Sonnabend, P. Kroetz, D. Stupar, T. Kostiuik, and R. Schieder. Venus upper atmosphere winds from ground-based heterodyne spectroscopy of CO₂ at 10 μ m wavelength. *Planetary and Space Science*, 56:1399–1406, 2008. doi: 10.1016/j.pss.2008.05.006.
- D. O. Staley. The adiabatic lapse rate in the Venus atmosphere. *Journal of Atmospheric Sciences*, 27:219–223, 1970. doi: 10.1175/1520-0469(1970)027.
- H. Svedhem, D. V. Titov, D. McCoy, J.-P. Lebreton, S. Barabash, J.-L. Bertaux, P. Drossart, V. Formisano, B. Häusler, O. Korabiev, W. J. Markiewicz, D. Nevejans, M. Pätzold, G. Piccioni, T. L. Zhang, F. W. Taylor, E. Lellouch, D. Koschny,

- O. Witasse, H. Eggel, M. Warhaut, A. Accomazzo, J. Rodriguez-Canabal, J. Fabrega, T. Schirmann, A. Clochet, and M. Coradini. Venus Express - The first European mission to Venus. *Planetary and Space Science*, 55:1636–1652, 2007. doi: 10.1016/j.pss.2007.01.013.
- F. Taylor and D. Grinspoon. Climate evolution of Venus. *Journal of Geophysical Research (Planets)*, 114, 2009. doi: 10.1029/2008JE003316.
- F. W. Taylor. Climate Variability on Venus and Titan. *Space Science Reviews*, 125:445–455, 2006a. doi: 10.1007/s11214-006-9077-y.
- F. W. Taylor. Venus before Venus Express. *Planetary and Space Science*, 54:1249–1262, 2006b. doi: 10.1016/j.pss.2006.04.031.
- F. W. Taylor, R. Beer, M. T. Chahine, D. J. Diner, L. S. Elson, R. D. Haskins, D. J. McCleese, J. V. Martonchik, P. E. Reichley, S. P. Bradley, J. Delderfield, J. T. Schofield, C. B. Farmer, L. Froidevaux, J. Leung, M. T. Coffey, and J. C. Gille. Structure and meteorology of the middle atmosphere of Venus Infrared remote sensing from the Pioneer orbiter. *Journal of Geophysical Research*, 85:7963–8006, 1980. doi: 10.1029/JA085iA13p07963.
- F. W. Taylor, D. M. Hunten, and L. V. Ksanfomaliti. *The thermal balance of the middle and upper atmosphere of Venus*, pages 650–680. 1983.
- N. A. Teanby, R. de Kok, P. G. J. Irwin, S. Osprey, S. Vinatier, P. J. Gierasch, P. L. Read, F. M. Flasar, B. J. Conrath, R. K. Achterberg, B. Bézard, C. A. Nixon, and S. B. Calcutt. Titan’s winter polar vortex structure revealed by chemical tracers. *Journal of Geophysical Research (Planets)*, 113:12003, 2008. doi: 10.1029/2008JE003218.
- S. Tellmann, M. Pätzold, B. Häusler, M. K. Bird, and G. L. Tyler. Structure of the Venus neutral atmosphere as observed by the Radio Science experiment VeRa on Venus Express. *Journal of Geophysical Research (Planets)*, 114, 2009. doi: 10.1029/2008JE003204.
- The Eve Team, E. Chassefière, O. Korablev, T. Imamura, K. H. Baines, C. F. Wilson, D. V. Titov, K. L. Aplin, T. Balint, J. E. Blamont, C. G. Cochran, C. Ferencz, F. Ferri, M. Gerasimov, J. J. Leitner, J. Lopez-Moreno, B. Marty, M. Martynov, S. V. Pogrebenko, A. Rodin, J. A. Whiteway, L. V. Zasova, and the EVE team. European Venus Explorer: An in-situ mission to Venus using a balloon platform. *Advances in Space Research*, 44:106–115, 2009. doi: 10.1016/j.asr.2008.11.025.
- P. G. Thomas and P. Gierasch. Dust devils on Mars. *Journal of Geophysical Research Supplement*, 90:84–85, 1985.
- D. V. Titov, F. W. Taylor, H. Svedhem, N. I. Ignatiev, W. J. Markiewicz, G. Piccioni, and P. Drossart. Atmospheric structure and dynamics as the cause of ultraviolet markings in the clouds of Venus. *Nature*, 456:620–623, 2008. doi: 10.1038/nature07466.

- D. V. Titov, H. Svedhem, F. W. Taylor, S. Barabash, J.-L. Bertaux, P. Drossart, V. Formisano, B. Häusler, O. Korablev, W. J. Markiewicz, D. Nevejans, M. Pätzold, G. Piccioni, J.-A. Sauvaud, T. L. Zhang, O. Witasse, J.-C. Gerard, A. Fedorov, A. Sanchez-Lavega, J. Helbert, and R. Hoofs. Venus express: Highlights of the nominal mission. *Solar System Research*, 43:185–209, 2009. doi: 10.1134/S0038094609030010.
- C. C. C. Tsang, P. G. J. Irwin, C. F. Wilson, F. W. Taylor, C. Lee, R. de Kok, P. Drossart, G. Piccioni, B. Bezard, and S. Calcutt. Tropospheric carbon monoxide concentrations and variability on Venus from Venus Express/VIRTIS-M observations. *Journal of Geophysical Research (Planets)*, 113, 2008. doi: 10.1029/2008JE003089.
- T. Widemann, E. Lellouch, and A. Campargue. New wind measurements in Venus lower mesosphere from visible spectroscopy. *Planetary and Space Science*, 55:1741–1756, 2007. doi: 10.1016/j.pss.2007.01.005.
- R. E. Young, L. Pfister, and H. Houben. Baroclinic instability in the Venus atmosphere. *Journal of Atmospheric Sciences*, 41:2310–2333, 1984. doi: 10.1175/1520-0469(1984)041.
- L. V. Zasova and I. V. Khatountsev. Thermal zonal wind in the Venus middle atmosphere according to Venera 15 IR-spectrometry. *Advances in Space Research*, 19:1181–1190, 1997. doi: 10.1016/S0273-1177(97)00269-X.
- L. V. Zasova, I. A. Khatountsev, V. I. Moroz, and N. I. Ignatiev. Structure of the Venus middle atmosphere: Venera 15 fourier spectrometry data revisited. *Advances in Space Research*, 23:1559–1568, 1999. doi: 10.1016/S0273-1177(99)00169-6.
- L. V. Zasova, V. M. Linkin, and I. V. Khatuntsev. Zonal wind in the middle atmosphere of Venus. *Kosmicheskie Issledovaniia*, 38:54–70, 2000.
- L. V. Zasova, N. Ignatiev, I. Khatuntsev, and V. Linkin. Structure of the Venus atmosphere. *Planetary and Space Science*, 55:1712–1728, 2007. doi: 10.1016/j.pss.2007.01.011.
- T. L. Zhang, W. Baumjohann, M. Delva, H.-U. Auster, A. Balogh, C. T. Russell, S. Barabash, M. Balikhin, G. Berghofer, H. K. Biernat, H. Lammer, H. Lichtenegger, W. Magnes, R. Nakamura, T. Penz, K. Schwingenschuh, Z. Vörös, W. Zambelli, K.-H. Fornacon, K.-H. Glassmeier, I. Richter, C. Carr, K. Kudela, J. K. Shi, H. Zhao, U. Motschmann, and J.-P. Lebreton. Magnetic field investigation of the Venus plasma environment: Expected new results from Venus Express. *Planetary and Space Science*, 54:1336–1343, 2006. doi: 10.1016/j.pss.2006.04.018.
- X. Zhu. Maintenance of equatorial superrotation in the atmospheres of Venus and Titan. *Planetary and Space Science*, 54:761–773, 2006. doi: 10.1016/j.pss.2006.05.004.
- R. W. Zurek, J. R. Barnes, R. M. Haberle, J. B. Pollack, J. E. Tillman, and C. B. Leovy. *Dynamics of the atmosphere of Mars*, pages 835–933. 1992.

Publications

Refereed contributions

1. *Zonal thermal winds on Venus derived from the radio-occultation temperature sounding on board Venus Express.*
Piccialli, A., Tellmann, S., Titov, D.V., Paetzold, M., and Haeusler, B. (in preparation).
2. *Cyclostrophic winds from the Visible and Infrared Thermal Imaging Spectrometer temperature sounding: A preliminary analysis.*
Piccialli, A.; Titov, D. V.; Grassi, D.; Khatuntsev, I.; Drossart, P.; Piccioni, G.; Migliorini, A.
Journal of Geophysical Research, Volume 113, Issue 2, CiteID E00B11

Posters and Presentations

1. 10 November 2009:
VeRa SWTM
Brussels, Belgium.
Talk: 'Thermal winds from the VeRa temperature sounding ' by '**Piccialli, A.**, Tellmann, S., Titov, D. V., Pätzold, M., and Häusler B.'
2. 28 September - 2 October 2009:
IX Convegno Nazionale di Scienze Planetarie
Amalfi (Naples), Italy.
Talk: 'Zonal winds in Venus mesosphere derived from VIRTIS/VEEx temperature retrievals' by '**Piccialli, A.**, Titov, D. V., Migliorini, A., Grassi, D., Piccioni, G., Drossart, P., Tellmann, S., and Pätzold, M.'
3. 13 - 18 September 2009:
European Planetary Science Congress (EPSC)
Potsdam, Germany.
Talk: 'Thermal winds in Venus mesosphere derived from the VIRTIS and VeRa temperature sounding' by '**Piccialli, A.**, Titov, D. V., Tellmann, S., Migliorini, A., Grassi, D., Pätzold, M., Häusler, B., Piccioni, G., and Drossart, P.'

4. 26 - 27 May 2009:
14th VIRTIS Meeting
Paris, France.
Talk: 'Thermal winds in Venus mesosphere derived from VIRTIS and VeRa/VEEx' by 'Piccialli, A., Titov, D., Migliorini, A., Tellmann, S., Grassi, D., Paetzold, M., Piccioni, G.'

5. 11 - 15 May 2009:
43rd ESLAB Symposium, International Conference on Comparative Planetology:
Venus - Earth - Mars
ESTEC, Noordwijk (NL).
Poster: Thermal wind in the atmospheres of Venus and the other planets' by 'Piccialli, A.; Titov, D. V.; Migliorini, A., Tellmann, S.; Grassi, D.; Piccioni, G.; Pätzold, M.'

6. 5 May 2009:
Oberseminar
Institut for Geophysics and Extraterrestrial Physics (IGEP), TU Braunschweig, Germany.
Talk: 'Cyclostrophic wind in Venus mesosphere ' by 'Piccialli, A., Titov, D. V., Hoerd, A.'

7. 17 April 2009:
VeRa SWTM
Köln, Germany.
Talk: 'Thermal winds in Venus mesosphere from VIRTIS and VeRa/VEEx temperature sounding' by 'Piccialli, A., Titov, D., Tellmann, S., Migliorini, A.'

8. 25 March 2009:
Venus dynamics workshop
Atmospheric, Oceanic and Planetary Physics, University of Oxford, Oxford, U.K.
Talk: 'Cyclostrophic winds in Venus mesosphere from VIRTIS and VeRa/VEEx temperature retrievals' by 'Piccialli, A., Titov, D. V., Migliorini, A., Tellmann, S.'

9. 28 January 2009:
S3 Student Seminar
Max Planck Institute for Solar System Research (MPS), Katlenburg - Lindau, Germany.
Talk: 'Thermal zonal wind in Venus mesosphere' by 'Piccialli, A., Titov, D. V., Hoerd, A.'

10. 4 - 5 December 2008:
3rd VMC SWT

Katlenburg - Lindau, Germany.

Talk: 'Thermal winds vs measurements: a check of cyclostrophic approximation' by 'Piccialli, A., Titov, D., VeRa and VMC team'.

11. 12 - 13 November 2008:

13th VIRTIS Meeting

Rome, Italy.

Talk: 'Cyclostrophic winds from VIRTIS and VeRa' by 'Piccialli, A., Titov, D., Migliorini, A. Grassi, D., Tellmann, S., Khatuntsev, I., Drossart, P., Piccioni, G., Paetzold, M., Haeusler, B.'.

12. 21 - 26 September 2008:

European Planetary Science Congress (EPSC)

Münster, Germany.

Talk: 'Cyclostrophic winds in Venus Mesosphere from VIRTIS and VeRa/VEEx temperature retrievals' by 'Piccialli, A., Titov, D. V., Migliorini, A., Grassi, D., Tellmann, S., Khatuntsev, I., Drossart, P., Piccioni, G., Paetzold, M.'.

13. 13 - 20 July 2008:

37th COSPAR Scientific Assembly

Montreal, Canada.

Poster: 'Retrieval of the cyclostrophic wind in the Venus mesosphere from the VIRTIS/Venus Express temperature sounding' by 'Piccialli, A.; Titov, D. V.; Grassi, D.; Khatuntsev, I.; Drossart, P.; Piccioni, G.; Migliorini, A.'.

14. 29 April 2008:

Oberseminar

Institut for Geophysics and Extraterrestrial Physics (IGEP), TU Braunschweig, Germany.

Talk: 'Cyclostrophic wind in Venus Mesosphere' by 'Piccialli, A., Titov, D. V., Hoerd, A.'.

15. 13 - 18 April 2008:

European Geosciences Union, General Assembly 2008

Vienna, Austria.

Poster: 'Thermal wind in the Venus mesosphere from the VIRTIS/Venus Express temperature sounding' by 'Piccialli, A.; Titov, D.V.; Grassi, D.; Khatuntsev, I.; Moissl, R.; Piccioni, G.; Markiewicz, W.J.; Drossart, P.'.

16. 2 - 8 March 2008:

Venus Express Scientific Workshop

La Thuile, Italy.

Talk: 'Cyclostrophic wind in VIRTIS mesosphere from VIRTIS temperature sounding' by '**Piccialli, A.**, Titov, D. V., Grassi, D., Khatuntsev, I., Drossart, P., Piccioni, G., Migliorini, A.'

17. 20 February 2008:

S3 Student Seminar

Max Planck Institute for Solar System Research (MPS), Katlenburg - Lindau, Germany.

Talk: 'Cyclostrophic wind in Venus mesosphere' by '**Piccialli, A.**, Titov, D. V., Hoerd, A.'

18. 10 September 2007:

Workshop on the Venus Atmospheric Dynamics

Max Planck Institute for Solar System Research (MPS), Katlenburg - Lindau, Germany.

Talk: 'Cyclostrophic wind in the Venus mesosphere from the VIRTIS temperature sounding' by '**Piccialli, A.**, Titov, D. V., Grassi, D., Piccioni, G., Moissl, R., Markiewicz, W.J., Khatuntsev, I.'

19. 20 - 24 August 2007:

European Planetary Science Congress (EPSC)

Potsdam, Germany.

Talk: 'Cyclostrophic wind in the Venus mesosphere from the VIRTIS temperature sounding' by '**Piccialli, A.**, Titov, D. V., Grassi, D., Piccioni, G., Moissl, R., Markiewicz, W.J., Khatuntsev, I.'

20. 26 - 27 June 2007:

10th VIRTIS Meeting

Rome, Italy.

Talk: 'First retrievals of the zonal wind' by '**Piccialli, A.**, Titov, D., Grassi, D.'

21. 6 - 7 March 2007:

9th VIRTIS Meeting

Berlin, Germany.

Talk: 'Dynamics of the Venus mesosphere: plans for the study based on the VIRTIS, VMC, and VeRa observations' by '**Piccialli, A.**, Titov, D.'

22. 18 - 22 September 2006:

European Planetary Science Congress (EPSC)

Berlin, Germany.

Talk: 'PFS-MEX nadir observations at 4.3 μm in the Mars atmosphere with account for non-LTE emissions' by '**Piccialli, A.**, Palomba, E.; Lopez Valverde, M.'

A.; Gilli, G.; Grassi, D.; D'Amore, M.; Formisano, V.'.

23. 5 - 9 September 2006:

VII Convegno Nazionale di Scienze Planetarie

S. Felice al Circeo (Lt), Italy.

Talk: 'Analisi della struttura non-LTE del CO₂ a 4.3 μm nell'atmosfera marziana attraverso le osservazioni Nadir del PFS-MEX' by '**Piccialli, A.**; Palomba, E.; Lopez Valverde, M. A.; Gilli, G.; Grassi, D.; D'Amore, M.; Formisano, V.'.

Acknowledgements

I would like to start my acknowledgements by thanking my supervisor Dr. Dmitry Titov. Thank you Dima for all your help, advice, for being always present and kind also in your busiest moments. Really, I believe I could not have had a better supervisor.

I am grateful to the Max Planck Institute for Solar System Research (MPS) and to the International Max Planck Research School (IMPRS) for providing me the opportunity and the financial support to carry out the research presented in this thesis. I must thank the coordinator of IMPRS, Dr. Dieter Schmitt, for all his efforts and enthusiasm in organising the school. Further, I would like to thank my university supervisor, Prof. Dr. Andreas Hördt for showing always interest in my work and for his useful comments.

This work would not have been possible without the efforts of all the people of the VIRTIS and VeRa teams. I wish to thank the P.I.s of the experiments: Pierre Drossart, Giuseppe Piccioni, Bernd Häusler and Martin Pätzold for having devised and maintaining such beautiful instruments. My gratitude goes to Davide Grassi, Alessandra Migliorini and Silvia Tellmann for the successful collaboration and for providing me the temperature profiles necessary to carry out this work. In addition, many thanks go also to Igor Khatuntsev and Nikolai Ignatiev for their helpful advice.

A special thanks go to Prof. Peter Read for his helpful and useful advice and for many valuable discussions. Thank you also for giving me the possibility to visit Oxford. The time I spent there was really fruitful and gave me the opportunity to learn a lot. I have to thank also all the people at the Atmospheric, Oceanic and Planetary Physics sub-department (AOPP), in Oxford, not only for the very interesting discussions (during the coffee break), but especially for their kind hospitality and for showing me around the beautiful city of Oxford: in particular, thanks to Colin, Con, Jo and Joao.

Further I would like to acknowledge constructive discussions with Alexander Medvedev and Miriam Rengel: thank you for your suggestions and support.

Finally, I wish to thank all the friends who have accompanied me in the last three years. A big thank-you goes to my apartment mate Manu for not killing me in the last months, but especially for all the fun and good laugh we had in the last three years. I would like to thank the "desperate housewives" group (Ela, Sofie, Sanja, Miriam) for the enjoyable time spent together. My sprachpartner Anna for not let me forget my italian. The whole "stammtisch" group (Chris, Alessandro, Gianmario, Alexandra, Marius, Anna, and all the others), who helped me in the last months not to think all the time at my thesis. And then to my distant friends: Sebastiano, Antonio, Francesca, Marina, Laura; thank you for being always present even if far away. And finally I want to thank my mother for her support, patience and for always encouraging me.

Curriculum Vitae

Name: Arianna Piccialli

Geburtsdatum: 23 October 1979

Geburtsort: Neapel, Italien

Staatsangehörigkeit: italienisch

Schulische Ausbildung

1985 – 1990: Scuola Elementare Statale "D. Morelli", Neapel, Italien

1990 – 1993: Scuola Media Statale "G. Lettieri", Neapel, Italien

1993 – 1998: Liceo Scientifico Statale "L. B. Alberti", Neapel, Italien

Studium

1998 – 2006: Master degree in physics, University of Neapel "Federico II"

2002 – 2003: Austauschstudium im Rahmen des ERASMUS Programms
Universidad de la Laguna, Kanarische Inseln, Spanien